UNIVERSIDAD NACIONAL AUTÓNOMA DE MÉXICO

FACULTAD DE INGENIERÍA

Analysis of the anisotropic plastic deformation during an indentation test using a polycrystalline plasticity finite element code

TESIS

Que para obtener el título de
Ingeniera Mecánica

P R E S E N T A

Hadassa Amelia Juárez Hernández

DIRECTOR DE TESIS

Dr. Rafael Schouwenaars

Ciudad Universitaria, Cd. Mx., 2018

Agradecimientos

VNIVERSIDAD NACIONAL
AVTONOMA DE
MEXICO
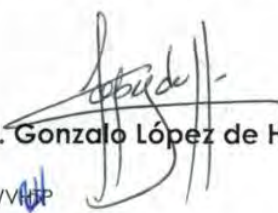
Srita. Hadassa Amelia Juárez Hernandez
P R E S E N T E

Por este conducto le informo que el Consejo Técnico de esta Facultad, en su sesión ordinaria celebrada el 5 de octubre del presente, conoció y analizó la solicitud por usted presentada relativo a escribir su tesis en un idioma diferente al español, en su caso en el idioma inglés.

En este sentido, en virtud de que no existe ninguna restricción en la Legislación Universitaria y de acuerdo con la interpretación del abogado general con número de oficio AGEN/DGEL/183/11 CIJ/24/11 el pleno del Consejo Técnico aprobó dicha solicitud.

Sin más por el momento, le envío un cordial saludo.

Atentamente
"Por mi raza hablará el espíritu"
Ciudad Universitaria Cd. Mx., a 6 de octubre de 2017
El Secretario del Consejo Técnico

Ing. Gonzalo López de Haro

GLH/VHP

Resumen

La gran mayoría de los procesos de manufactura de metales involucran deformación plástica, la cual ocasiona cambios en su microestructura. Una de las consecuencias de estos cambios es la aparición de anisotropía mecánica. El término anisotropía hace referencia a que la magnitud de las propiedades mecánicas del material varía según la dirección de estudio. En metales, esta anisotropía observada suele deberse al desarrollo de orientaciones preferenciales de los cristales del material durante los procesos de conformado (textura).

La anisotropía generada puede causar problemas en procesos posteriores o, por el contrario, se puede utilizar para obtener geometrías complejas. Sin embargo, para contrarrestar o aprovechar esta anisotropía, es necesario conocer cómo afecta al comportamiento plástico del material. Una de las formas de estudiar esto es mediante el uso de ensayos mecánicos. Para esta tesis, se utilizó el ensayo de indentación instrumentada (EII) para analizar la deformación plástica anisotrópica en 5 láminas de aluminio con distintas texturas. El EII es de especial interés en la industria y en la investigación ya que permite caracterizar materiales de una manera rápida y no destructiva. Adicionalmente, este ensayo permite relacionar propiedades mecánicas entre ellas, ofreciendo así la posibilidad de obtener un amplio panorama del material.

Para el análisis de la deformación plástica durante el ensayo de indentación, se utilizó un código de plasticidad policristalina (HMS) desarrollado por KU Leuven, Bélgica, el cual hace uso de una teoría multiescala de plasticidad. Este tipo de teorías involucran relacionar el comportamiento microscópico del material (deformación de los granos), con el comportamiento macroscópico del material (deformación de la lámina). Los resultados predichos por HMS fueron comparados con los experimentales y se analizaron las posibles fuentes de diferencia entre ellos. Se encontró que éstas se debían en parte a las limitaciones del modelo de elemento finito empleado, y en una mayor parte, a la simplificación de endurecimiento isotrópico homogéneo que supone la teoría de la plasticidad clásica

Contenido

Introduction

Aluminium is the most widely used non-ferrous metal in the world [1]. It is a material used in the industry and everyday life due to characteristics such as [2]:

a) good corrosion and oxidation resistance
b) low density
c) medium strength that can be increased by heat treatment
d) easy to recycle

Aluminium alloys are divided into two major categories: cast alloys and wrought alloys. In both cases, they are further classified according to their main alloying element using a numeral system established by The Aluminum Association [3, 4].

Cast aluminium alloys

1xx.0: 99.00% purity alloys

2xx.0: Al-Cu alloys

3xx.0: Al-Si-Cu-Mg or Al-Si-Mg alloys

4xx.0: Al-Si alloys

5xx.0: Al-Mg alloys

6xx.0: Unused

7xx.0: Al-Zn alloys

8xx.0: Al-Sn

9xx.0: Other

Wrought aluminium alloys

1xxx: Pure aluminium
- Strain hardenable
- Uses: transmission lines, food packaging

2xxx: Al-Cu alloys
- Heat treatable
- Uses: aeronautical industry,

3xxx: Al-Mn alloys
- Strain hardenable
- Uses: beverage cans, cooking utensils, heat exchangers

4xxx: Al-Si alloys
- Some can be heat treated
- Uses: welding wire

5xxx: Al-Mg alloys
- Strain hardenable
- Uses: boat and ship hulls, architectural

6xxx: Al-Mg-Si alloys
- Heat treatable
- Uses: structural and architectural, some vehicles frames

7xxx: Al-Zn alloys
- Heat treatable
- Uses: aircrafts, watches

8xxx: Al-Other elements
- Varies according to the alloy

For wrought alloys, the alloy classifying number may be accompanied by a letter and another number indicating the temper. Temper indicates that the aluminium alloy has been thermally treated to change its original properties, thereby providing great versatility in applications. The basic tempers are [2, 5]:

F: As fabricated
No special control of the processes during manufacturing.

O: Annealed
It produces the lowest strength and highest ductility.

H: Strain hardened (Table I.1)
Also called work hardening, strain hardening is a strengthening mechanism that is produced during plastic, or permanent, deformation. For this category, the first digit states whether a subsequent heat treatment was applied, while the second one indicates residual hardening.

W: Solution heat treated
Its aim is to strengthen the alloy through the introduction of solutes in the material structure (solvent). The difference in size between these solutes and solvent will greatly influence the achieved strength. This treatment is rarely used alone due to its instability.

T: Solution heat treated and aged (Table I.1)
In addition to being solid solution treated, the alloy is aged. This heat treatment, also called precipitation hardening, is based on the effect of temperature on solubility. It is carried out in three stages [1]:
   a) *Solution treatment:* Alloying elements are brought in solid solution at high temperatures to form a supersaturated solid solution (SSS).
   b) *Quenching:* The supersaturated solid solution is suddenly cooled down and is preserved as a metastable state by preventing diffusion of the solute.
   c) *Ageing:* Particles are precipitated from the solid solution into the material structure and serve to strengthen the alloy.

Table I.1 Strain hardened code (H), and solution heat treatment and ageing code (T) [2, 5]

T: Solution heat treated and aged	H: Strain hardened
T1—Cooled from an elevated-temperature shaping operation + natural aged T2—Cooled from an elevated-temperature shaping operation + cold worked + natural aged T3—Solution treated + cold worked + natural aged T4—Solution treated + natural aged T5—Cooled from an elevated-temperature shaping operation + artificial aged T6—Solution treated + artificial aged T7—Solution treated + overaged T8—Solution treated + cold worked + artificial aged T9—Solution treated + artificial aged + cold worked T10—Cooled from an elevated-temperature shaping operation + cold worked + artificial aged	**First digit** 1—Cold worked only 2—Cold worked and partially annealed 3—Cold worked and stabilized **Second digit** 2—1/4 hard 4—1/2 hard 6—3/4 hard 8—Hard 9—Extra hard

Due to the multiple uses and versatility of wrought aluminium alloys, over 63,403 tons were produced in 2017 [6]. They can be fabricated directly from the ore (primary aluminium) or from scraps (secondary aluminium). In the former case, it is necessary to produce aluminium oxide first from the ores found in mines, such as bauxite, to obtain aluminium from it. The most common chemical method to obtain aluminium oxide, or alumina, is called the Bayer process. The general process is as follows [1, 3, 4]:
   a) *Milling:* The bauxite is washed, crushed, and mixed with lime.
   b) *Digestion:* The product is heated in a pressure vessel with sodium hydroxide to form a sodium aluminate solution from the minerals in the bauxite.
   c) *Filtering:* Bauxite residues and other impurities are separated from the sodium aluminate solution.
   d) *Precipitation:* The sodium aluminate solution is cooled down and aluminium hydroxide seeds are added to promote the precipitation of solid aluminium hydroxide crystals.

e) ***Classification:*** Crystals formed in the previous stage are classified by size. Fine crystals are separated and used as seeders. Coarse crystals proceed to the calcination step.

f) ***Calcination:*** Rotary kilns at over 1000°C are used to produce alumina in this final step.

Aluminium is extracted from the alumina using the Hall-Héroult process [1]. During this process the alumina is electrolytically reduced in electrolytic cells using cryolite as an electrolyte.

Once aluminium is obtained, it proceeds to ingot casting, where, after being completely solidified, it will continue to the rolling stage. At this stage, the slab is plastically deformed by a series of rolls to diminish its height. According to the process temperature (Ec. I.1), two types of rolling can be distinguished: hot rolling ($T_H > 0.75$) and cold rolling ($T_H < 0.3$).

Eq. I.1

$$T_H = \frac{T}{T_M}$$

Where:
  T: current material temperature
  T_M: melting point

Both types of rolling produce changes in the material structure that cause the mechanical properties to be directionally dependent. This is called anisotropy and is important for two main reasons. First, this anisotropy may be harnessed to achieve complicated geometries without sacrificing weight or mechanical properties. Second, it may cause problems in further stages of manufacturing, which translate in loss of dimensional control and material waste.

One of the mechanical properties showing anisotropy is hardness. Hardness, in its most general definition, is a property associated to the resistance of the material to plastic deformation, specifically by means of indentation [7, 8, 9]. This property is of particular interest, both in industry and scientific research, because it allows for a quick and non-destructive characterisation of the material. Using a specific type of hardness test, called instrumented hardness test, it is also possible to obtain relations between different mechanical properties.

The purpose of this thesis is to observe the influence of the present anisotropy in the hardness of 5 aluminium alloy sheets. For this end, a software (HMS) developed by KU Leuven, in Belgium, will be used. This thesis belongs to a series of ongoing international works to use HMS as a tool to study anisotropic plastic behaviour in real life scenarios [10, 11, 12].

Objectives

1. To carry out instrumented Vickers microindentation test in 5 aluminium sheets (AA6016 (1mm thickness), AA6016 (2mm thickness), AA5005, AA1100, AA3103) and perform a statistical analysis of the results.
2. To simulate this test with isotropic FEM models.
3. To use the Hierarchical Multi Scale Software (HMS) to simulate the test under the assumptions of plastic anisotropy.
4. To compare the experimental data with results from the FEM models and to compare the FEM models between themselves.
5. To determine whether HMS can predict the anisotropy observed in the Vickers microindentation test.
6. To analyse the deviations of the FEM models from experimental data based on concepts of crystal and continuum plasticity, texture, and FEM.

Chapter 1. Theoretical framework

1.1 Continuum plasticity

Plasticity is the theory that studies the permanent deformation that bodies present under loads, and the associated stresses. This phenomenon is incremental in nature since the resulting plastic deformation is determined by the complete history of straining [13].

At macroscopic levels, the description of the permanent deformation of a body can be made with the continuum plasticity theory. This theory has the advantage that it implicitly considers mechanisms that occur during plastic deformation without considering their details.

1.1.1 Stress and strain

Although formal deductions of the tensorial quantities known as stress and strain exist, practical examples tend to be enough to give a concise explanation of these concepts. Among such practical examples is the tensile test. This test is a standardised procedure to determine a material response under a mechanical load [14].

For this test, a sample of known dimensions and geometry is placed between the clamps of a universal tensile stage. Then, a known displacement is applied to one of the clamps, while the other one remains static, and the force necessary to achieve the displacement is recorded. For an elastic plastic material, two types of material behaviour can be observed in this test, elastic (non-permanent, reversible), and plastic (permanent, irreversible).

The tensile test assures uniaxial tension in the zone of analysis during most of the test. The recorded load and displacement depend on the probe initial size and shape. To obtain the material response independent from the geometric characteristics of the sample, the engineering stress is defined (Eq. 1.1), where stress is simply defined as the material response to an external load.

Eq. 1.1

$$s = \frac{F}{A_0}$$

Where:

    F: force

    A_0: initial cross-sectional area

The engineering strain quantifies the specimen length change (Ec. 1.2)

Eq. 1.2

$$e = \frac{\Delta l}{l_0} = \frac{l - l_0}{l_0}$$

Where:

    l_0: initial length

    l: final length

The s vs e graph (Fig. 1.1) allows to obtain, directly or indirectly, information regarding yield stress, hardening behaviour, etc.

The decrease in stress observed is due to a plastic instability, known as "neck formation", which signals the end of the homogenous deformation in the form of a localised reduction of cross sectional area. One can determine the stress at which this takes place using the Considère criterion.
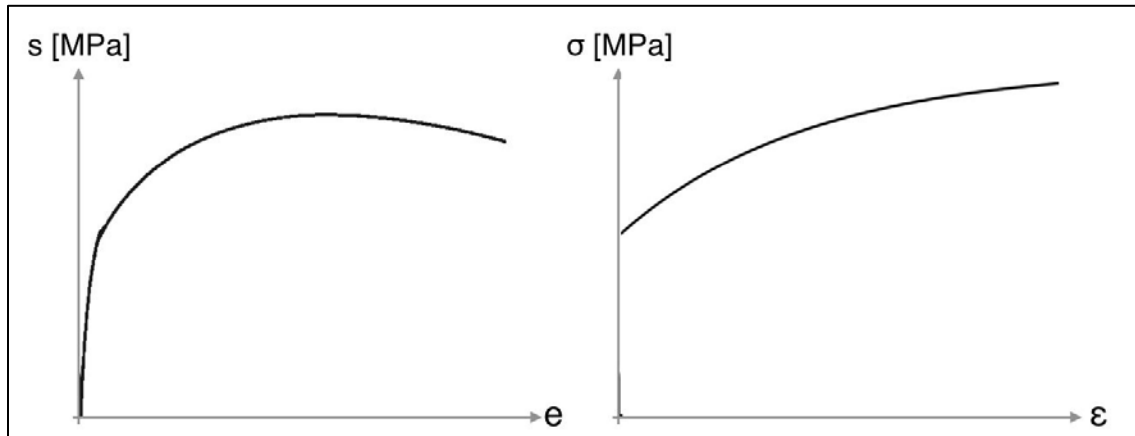
Figure 1.1 Left: *s* vs *e*. Right: σ vs ε

As seen from Eq. 1.1 and Eq. 1.2, the engineering quantities are simplifications since they only consider the initial and final state of the specimen and not its condition throughout the test. Instead true engineering stress (Eq. 1.3) and strain (Eq. 1.5) may be defined using the sample's current dimensions.

True stress (σ) is defined as:

$$\sigma = \frac{F}{A} = (1 + e)s$$

Where:

      σ: true stress
      A: current cross-sectional area

True strain (ε) is defined in incremental form:

$$d\varepsilon = \frac{dl}{l}$$

Upon integration one finds Ec. 1.5:

$$\varepsilon = \int_{l_0}^{l} \frac{dl}{l}$$

$$\varepsilon = \ln\left(\frac{l}{l_0}\right)$$

Both quantities, true strain and true stress, consider that the volume remains the same throughout the deformation process. Hence, they are only valid in the plastic range, since elastic deformation implies volume change. The resulting true stress vs true strain graph is presented in Fig. 1.1.

At small deformations, the engineering and true quantities give similar results. Therefore, for mechanical and structural design, the first ones are commonly used since they introduce an insignificant deviation in the calculations and allow for the solution of linear equations. For applications that require larger deformations, such as manufacturing processes, the second ones are employed.

1.1.2 Hardening laws

During cold working, it can be seen from Fig. 1.1 that an increase in load is required to increase the material plastic deformation. This phenomenon is called strain hardening; the microscopic mechanisms behind it are explained in [15]. However, for the macroscopic formulation, empirical "laws" can be used to describe this behaviour during a tensile test. It must be mentioned that these are in fact simple fitting approaches of measured curves, so the use of the term "hardening law" is strongly misleading and scientifically incorrect. Several of these laws exist, each one describing with different degrees of accuracy the phenomena experienced by the material. Inadequate fitting of experimental data to one of these laws may result in an erroneous description of the material behaviour.

Two of these laws, concerning only plastic behaviour, are Hollomon and Voce [13, 15]:
a) _Hollomon:_ A commonly used hardening law (Eq. 1.6), where k_h and n_h are material constants that describe the hardening behaviour.

Eq. 1.6

$$\sigma_h = k_h \varepsilon^{n_h}$$

b) _Voce:_ This hardening law (Eq. 1.7) considers strain hardening saturation, where k_V and n_V are material constants related to the hardening behaviour.

Eq. 1.7

$$\sigma_V = \sigma_0 + k_V(1 - e^{-n_V \varepsilon})$$

Strain hardening saturation is a phenomenon in which at higher strains, the strain hardening effect decreases significantly. This is a consequence of the different strain hardening stages, which have been described in early literature on the topic [16]. As seen from Fig. 1.2, this effect is reached at very high strains (99.99% Al).
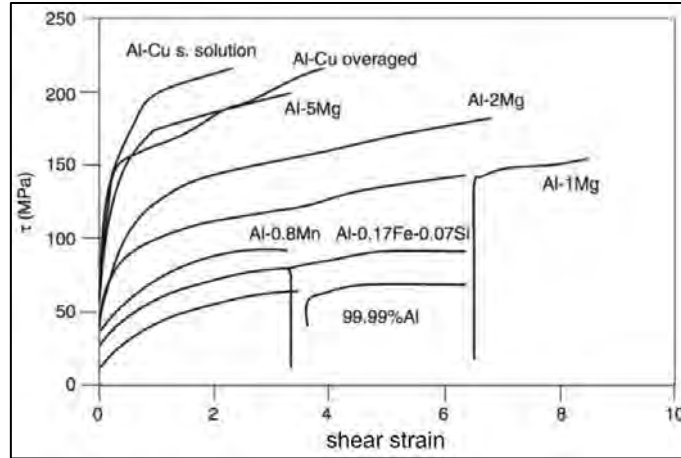
Figure 1.2 Large strain shear stress-strain curves of several Al alloys measured in room temperature torsion tests [15]

1.1.3 Yield criteria

Constitutive equations used for elasto-plastic materials usually require to be decomposed into elastic and plastic behaviour. Elastic behaviour is described by Hooke's Law (Eq. 1.8).

<div align="right">Eq. 1.8</div>

$$\boldsymbol{\varepsilon} = \mathbf{S}\,\boldsymbol{\sigma}$$

Where:
- $\mathbf{S}$: compliance tensor
- $\boldsymbol{\sigma}$: Cauchy stress tensor
- $\boldsymbol{\varepsilon}$: infinitesimal strain tensor

For a linear isotropic material, Eq. 1.8 is simplified as Eq. 1.9:

<div align="right">Eq. 1.9</div>

$$\boldsymbol{\varepsilon} = \frac{1+v}{E}\boldsymbol{\sigma} - \frac{v}{E}\boldsymbol{\delta}\,\boldsymbol{\sigma}$$

Where:
- v: **Poisson's** ratio
- E: **Young's** modulus

In a tensile test, the yield stress defines the limit of elastic behaviour. However, for a material that is undergoing any possible combination of applied loads, a yield criterion is used to define the when plastic behaviour starts. Such a criterion can be formulated in the form of a scalar function of the stress tensor components (Eq. 1.10).

<div align="right">Eq. 1.10</div>

$$f(\boldsymbol{\sigma}) \leq k^2$$

Where:
- $f(\boldsymbol{\sigma}) < k^2$: elastic behaviour
- $f(\boldsymbol{\sigma}) = k^2$: plastic behaviour

Valid yield criteria must fulfil the following conditions:
a) ***Hydrostatic pressure independence:*** For metals, yielding is unaffected by hydrostatic pressure [13]. There is no change in volume associated with plastic deformation, nor can this deformation be due to a hydrostatic pressure. Therefore, the stress tensor may be decomposed as in Eq. 1.11, where the trace of $\boldsymbol{\sigma}$ is associated with a hydrostatic pressure:

Eq. 1.11

$$\boldsymbol{\sigma} = \boldsymbol{\sigma}^H + \boldsymbol{\sigma}^D$$

$$\boldsymbol{\sigma}^H = \frac{1}{3}\boldsymbol{\delta}\,\boldsymbol{\sigma}$$

$$\boldsymbol{\sigma}^D = \mathbf{s} = \boldsymbol{\sigma} - \frac{1}{3}\boldsymbol{\delta}\,\boldsymbol{\sigma}$$

Where:

$\boldsymbol{\sigma}^H$: Hydrostatic pressure
$\boldsymbol{\sigma}^D = \mathbf{s}$: deviatoric stress

b) **_Isotropic material:_** Isotropy, contrary to anisotropy, means that material properties are directionally independent. Rather than a requirement, this is a simplification. Consequently, the yield criterion must be expressed in terms of invariants of tensors. From the definitions of these invariants and Eq. 1.11.

Eq. 1.12

$$J_1, J_2, J_3: invariants\ of\ the\ deviatoric\ stress\ tensor$$

$$J_1 = Tr(\mathbf{s}) = 0$$

$$J_2 = -\frac{1}{2}\mathbf{s}\colon\mathbf{s}$$

$$J_3 = Det[\mathbf{s}]$$

The yield criterion may then be expressed as Eq. 1.13

Eq. 1.13

$$f(J_2, J_3) \le k^2$$

c) **_No Bauschinger effect:_** Yield strength is equal if the sign of the stress tensor is inversed, e.g. for uniaxial tension and compression.

d) **_Concavity_:** A thermodynamic requirement, which is imposed by the first law of thermodynamics.

Two of the most popular criteria that meet these requirements are Tresca (the reader is referred to [13]), and von Mises (Eq. 1.14). The latter, also known as the criterion of maximum distortion energy, can be written as Eq. 1.15 using the definition of J_2 (Ec. 1.12).

Eq. 1.14

$$J_2 \le k^2$$

Eq. 1.15

$$\frac{1}{6}\left((\sigma_{11} - \sigma_{22})^2 + (\sigma_{22} - \sigma_{33})^2 + (\sigma_{33} - \sigma_{11})^2 + 6(\sigma_{12}{}^2 + \sigma_{23}{}^2 + \sigma_{31}{}^2)\right) \le k^2$$

The general yield criterion given in Eq. 1.10 describes a geometrical locus in a 6D stress space. Yield criteria may be geometrically represented in the principal stress space (Fig. 1.3a), where only three dimensions are needed.
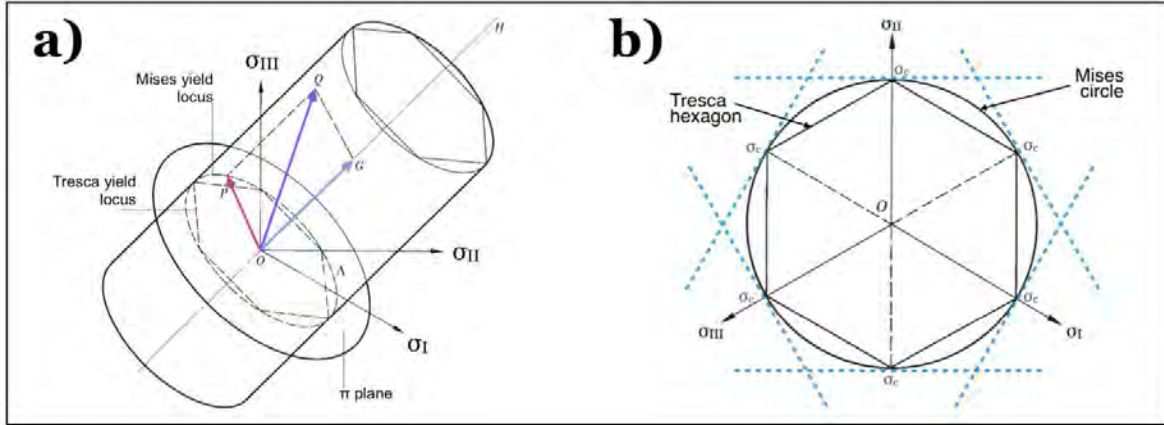
Figure 1.3 a) Geometrical representation of yield criteria in the principal stress space. Adapted from [13]. b) Deviatoric yield loci. Tresca (minimum), von Mises, and maximum possible (blue). Adapted from [13]

In this representation, **OH** is defined as a line whose direction cosines are (1/√3, 1√3, 1√3). The state of stress at any point can be represented using a vector parting from the origin. The decomposition of stress presented in Condition 1 is represented in (Fig. 1.3a), in which a stress vector **OQ** (purple) is decomposed into **OG** (blue), the hydrostatic stress, and **OP** (red), the deviatoric stress. For any state of stress, the deviatoric stress vector is confined to a plane that is perpendicular to **OH** and passes through the origin. This plane is called the π, or deviatoric, plane (Eq. 1.16)

$$s_{11} + s_{22} + s_{33} = 0$$

The latter equation follows automatically from the fact that the trace of a deviatoric tensor is **0**. If the yield stress is known, and according to Conditions 2, 6 points in the stress space are known, and the maximum and minimum valid yield criteria, as well as von Mises, can be defined using Condition 4 (Fig. 1.3b).

Parallel planes to π may be defined if the hydrostatic pressure is not zero. Since yield criteria are independent from hydrostatic pressure, they must be the same in all these planes. Therefore, the yield surface is a cylinder with its axis perpendicular to the π plane (Fig. 1.3a). This surface designates the stress state at the onset of plastic flow.

Stress states inside the yield surface correspond to an elastic behaviour. When the stress state reaches the yield surface, plastic deformation occurs with an incremental amount dε^P. The intersection between the yield surface and the π plane is called yield locus (Λ), which is identical every π/6 due to the requirement of isotropy and sign independence of the stress tensor.

The yield locus does not necessarily remain static throughout the deformation process. Strain hardening produces a change of shape and size of the yield locus throughout the deformation process. For homogeneous isotropic hardening, the yield locus only changes in size.

1.1.4 Plastic flow rules

Plastic flow rules determine the relationship between the plastic strain increment, d$\boldsymbol{\varepsilon}$[p], and stress increment, d$\boldsymbol{\sigma}$. Stress increment influences the magnitude of the strain increment [13], while current stress components influence the ratios of the components of d$\boldsymbol{\varepsilon}$[p]. This can be visualised using a strain hardenable material, in which after it has yielded, it is necessary to increase the applied load if one wants to keep deforming the material. A formal approach is necessary to determine an analytical expression of the flow rule [13, 17].

For this method some considerations need to be taken:
   a) Plastic deformation is not associated with a change in volume, therefore:
$$d\varepsilon_{11}{}^{P} + d\varepsilon_{22}{}^{P} + d\varepsilon_{33}{}^{P} = 0$$
   b) The change in the size of the yield locus is considered by a single parameter $\boldsymbol{c}$, which considers the strain history.
   c) The material is strain rate independent.

It is easily proven that the principal axes of stress coincide with those of the plastic strain increment. In consequence, it is possible to represent d$\boldsymbol{\varepsilon}$[p] as vector, multiplied by a proportionality constant, in the stress space previously established. A uniform cylinder, perpendicular to the $\boldsymbol{\pi}$ plane, may be defined using ($\boldsymbol{q}$(s_{11}, s_{22}, s_{33})=$\boldsymbol{constant}$), where $\boldsymbol{q}$ is an nth-degree homogenous function of the deviatoric stress components. The intersection between this cylinder and the $\boldsymbol{\pi}$ plane is the $\boldsymbol{\Gamma}$ curve. This curve is identical every $\pi/6$ due to reasons similar to those of Λ.

The function $\boldsymbol{q}$, and the relationships mentioned at the beginning of this section, may then be used to write the expression for the flow rule (Eq. 1.17)

Eq. 1.17

$$d\boldsymbol{\varepsilon}^{P} = \frac{\partial q}{\partial \boldsymbol{\sigma}} d\lambda$$

For this equation:
   $\boldsymbol{q}$: also referred as the plastic potential, defines the ratios of the components of the plastic strain increment. The cylinder generated when ($\boldsymbol{q}$(J_2, J_3)=constant) is called the plastic potential surface.
   d$\boldsymbol{\lambda}$: positive scalar that depends on the stress increment

For an equipotential surface, the increment in plastic work ($\boldsymbol{dw^{P}}$) is zero (Eq. 1.18).

Eq. 1.18

$$dw^{P} = \boldsymbol{\sigma} \, d\boldsymbol{\varepsilon}$$

From this equation it is deduced that $\boldsymbol{\sigma}$ and d$\boldsymbol{\varepsilon}$[p] are perpendicular to each other. This is known as the normality rule and is independent from the shape of the yield locus.

There are many similarities between Λ and Γ. Therefore, f and q can be considered identical. This type of flow rule is called the associated flow rule. As an example, a flow rule under this consideration, called Levi-Mises, is presented (Eq. 1.19). This equation establishes that plastic strain increment has the same direction that the stress that caused it.

Eq. 1.19

$$d\boldsymbol{\varepsilon}^{P} = \mathbf{s} \, d\lambda$$

11

1.1.5 Anisotropic yield criteria

Despite the popularity of isotropic yield criteria, anisotropic yield criteria have been developed to increase the accuracy when modelling real-world materials. One of the options for obtaining them is the phenomenological approach, in which the coefficients of polynomials of different degrees are calibrated by multiple tests. However, this has the disadvantage that mechanical tests cannot probe the entire stress space, and an interpolation function must be used, which may induce errors of different magnitude [18]. The reader is referred to [19] for a review of these type of criteria.

An alternative approach is to obtain the data for the fitting function through theoretical models for polycrystal plasticity. This has the advantage that many more points in the stress or strain rate space can be probed by computer simulation, which is generally much cheaper than mechanical tests. Also, one can follow the evolution of the material properties during deformation, whereas mechanical tests only determine the initial state.

The Facet method [18] uses a fitting function for the yield locus which is the nth root of a homogeneous n^{th}-degree polynomial (just like Von Mises uses the square root of a second degree polynomial). The homogeneity of the polynomial guarantees that the yield locus is always convex, even in presence of small numerical errors during the calculation. By taking the value of n equal to 6 or 8, the number of parameters used to describe the polynomial becomes very high, hence allowing for a detailed description of complex yield surfaces at a reasonable computational cost. The details behind this approach will be elaborated into some more detail in the remainder of this introduction (Sections 1.3 and 1.4)

1.2 Anisotropy

1.2.1 Texture

Plastic anisotropy has its origins in the preferred orientation of the grains composing the material microstructure, called texture (Fig. 1.4). The concept of crystallographic texture should not be confused with other uses of this word, e.g. morphological texture as used in mineralogy or surface texture as used in tribology. In an isotropic material, the grains are randomly oriented, and in consequence, there is no preferred orientation. The corresponding texture is called the random texture.
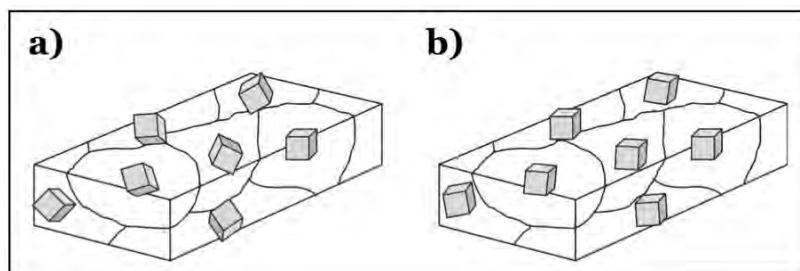

Figure 1.4 a) Material with random texture. b) Material with preferred orientation. Both from [15]

Knowledge of the orientation of a material grains is necessary to give a description of its texture. This orientation is given relative to the macroscopic sample, therefore, two reference systems are needed, one for the whole specimen, and one for the crystal [15]. The choice of axes of these reference systems is usually based on convenience.

For the sample, the symmetry originated by the different manufacturing processes is used to define natural (or principal) axes, and for the crystal, a set of crystallographic directions that are already orthogonal between themselves is commonly used [20]. For a material that comes from a rolling process, the directions chosen are ND (normal direction), RD (rolling direction), and TD (transversal direction), which are mutually orthogonal (Fig. 1.5a).
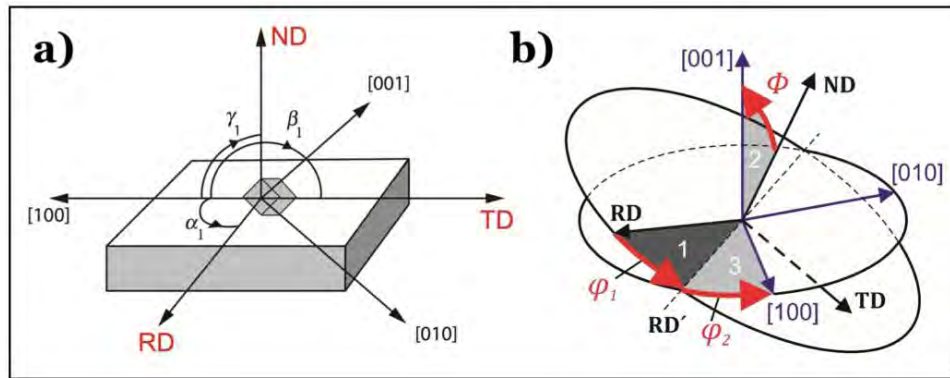
Figure 1.5 a) Crystal and sample reference systems [20]. b) Euler angles, according to the Bunge convention [20]

For a cubic crystal, the [100], [010], and [001] crystallographic directions are employed (Fig.5a). Choice of reference systems for other geometry and types of crystalline structure can be consulted in [20]

After both reference systems have been established, the crystal orientation can be defined by the orientation of the crystal coordinate system with respect to the specimen coordinate system. This can be written as Eq. 1.20:

Eq. 1.20

$$\mathbf{C_C} = \mathbf{g} \cdot \mathbf{C_S}$$

Where:

$\mathbf{C_C}$: crystal coordinate system
$\mathbf{C_S}$: specimen coordinate system
$\mathbf{g}$: orientation

The orientation can be expressed using the tensor of directional cosines (Eq. 1.21), which consists of the cosines of the angles between the crystal reference system and the sample reference system.

Eq. 1.21

$$\mathbf{g} : \begin{pmatrix} g_{11} & g_{12} & g_{13} \\ g_{21} & g_{22} & g_{23} \\ g_{31} & g_{32} & g_{33} \end{pmatrix}$$

13

By using three rotations defined by the Euler angles (φ_1, Φ, φ_2), it is possible to transform the specimen coordinate system unto the crystal coordinate system. Eq. 1.22 presents these rotations using the Bunge convention (Fig. 1.5b).

$$\mathbf{g} : \begin{pmatrix} g_{11} & g_{12} & g_{13} \\ g_{21} & g_{22} & g_{23} \\ g_{31} & g_{32} & g_{33} \end{pmatrix}$$

$$\mathbf{g}_{\varphi_1} : \begin{pmatrix} Cos[\varphi_1] & Sin[\varphi_1] & 0 \\ -Sin[\varphi_1] & Cos[\varphi_1] & 0 \\ 0 & 0 & 1 \end{pmatrix}$$

$$\mathbf{g}_{\phi} : \begin{pmatrix} 1 & 0 & 0 \\ 0 & Cos[\phi] & Sin[\phi] \\ 0 & -Sin[\phi] & Cos[\phi] \end{pmatrix}$$

$$\mathbf{g}_{\varphi_2} : \begin{pmatrix} Cos[\varphi_2] & Sin[\varphi_2] & 0 \\ -Sin[\varphi_2] & Cos[\varphi_2] & 0 \\ 0 & 0 & 1 \end{pmatrix}$$

The rotation matrix can then be linked to the Euler angles, as expressed in Eq. 1.23

$$\mathbf{g} = \mathbf{g}_{\varphi_1} \cdot \mathbf{g}_{\phi} \cdot \mathbf{g}_{\varphi_2}$$

Once defined the orientation of the individual single crystals, it is of interest to know which fraction of the total specimen volume has a given orientation. This can be achieved by defining the Orientation Distribution Function (ODF), which describes the distribution, in terms of volume fraction, of the orientations present in the sample (Eq. 1.24)

$$f(g) = \frac{\mathrm{d}V/V}{\mathrm{d}g} \quad ; \quad g(\varphi_1, \phi, \varphi_2)$$

Where:

$f(g)$: ODF

$\mathrm{d}g = Sin[\phi]\mathrm{d}\varphi_1\mathrm{d}\phi\mathrm{d}\varphi_2$

1.2.2 Texture measurement

Several techniques exist to experimentally determine a material texture. One technique is X-Ray diffraction, where an X-Ray beam incides onto a crystalline material and is scattered by planes of atoms (Fig. 1.6).
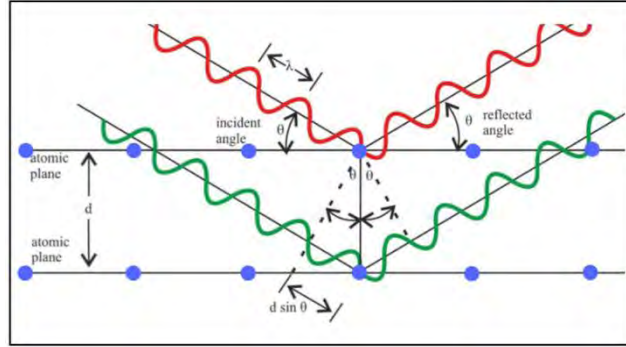
Figure 1.6 Schematisation of Bragg's law [21]

These atoms produce a regular array of waves that may or may not be cancelled out (destructive interference). The directions in which these waves add up (constructive interference), can be determined using Bragg's Law (Eq. 1.25).

$$2d\,Sin[\theta] = n\,\lambda$$

Where:

d: spacing between diffracting planes
θ: incident angle
n: any integer
λ: beam wavelength (0.01nm – 10nm for X-Ray beams)

The principle of X-Ray diffraction is incorporated in a texture goniometer. In this equipment, the sample is rotated in an Euler cradle so that the crystalline planes that satisfy the reflection condition are measured. The level of intensity obtained indicates the amount of grains that fulfil this condition, and in consequence, of the volume fraction of grains that have a given orientation. Stereographic projections of the obtained pole figures can be obtained as follows [22].

a) A unit cell of a grain with a given orientation is collocated inside the unit sphere (Fig. 1.7a).

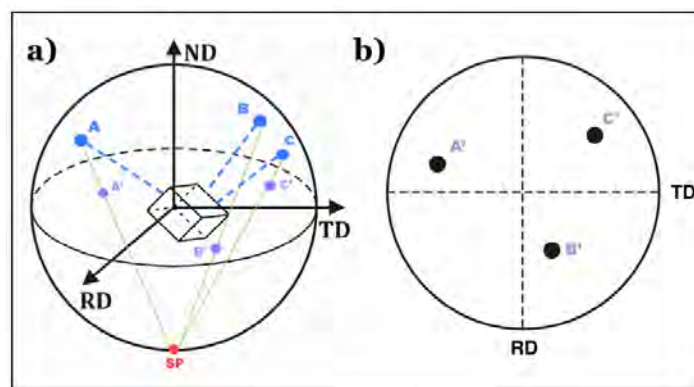
Figure 1.7 a) Unit sphere. Adapted from [15]. b) Stereographic projection of pole figure. Adapted from [15]

b) For the (100) pole figure, lines coincident with the normal vectors of each face of the unit cube are drawn. These lines are made to intersect the unit sphere (only the lines located in the northern hemisphere are used), obtaining points A, B, and C.

15

c) The points obtained in the previous step are connected to the sphere's south pole (SP). In their path they intersect the equatorial plane, resulting in points A', B', and C'. This second set of points serves to represent a 3D orientation in a 2D plane (Fig. 1.7b).

For an isotropic polycrystal, the second set of points is scattered all over the equatorial plane (Fig. 1.8a). In contrast, for a textured polycrystal, they are grouped (Fig. 1.8b and Fig. 1.8c).
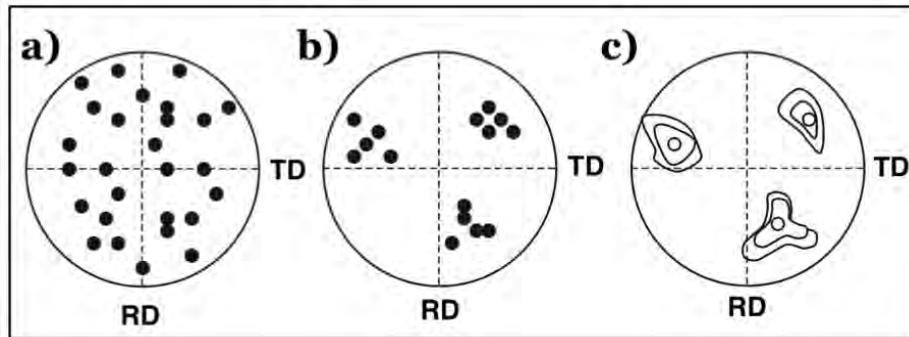
Figure 1.8 Stereographic projections a) Isotropic polycrystal. b) Textured polycrystal. c) Contour map [15]

From multiple pole figures, it is possible to reconstruct the ODF, for more information the reader is referred to [23]. The ODF is usually represented using a contour map of density distribution, in sections of the Euler space, where one of the Euler angles is maintained constant, and the other two vary inside a given range (Fig. 1.9)
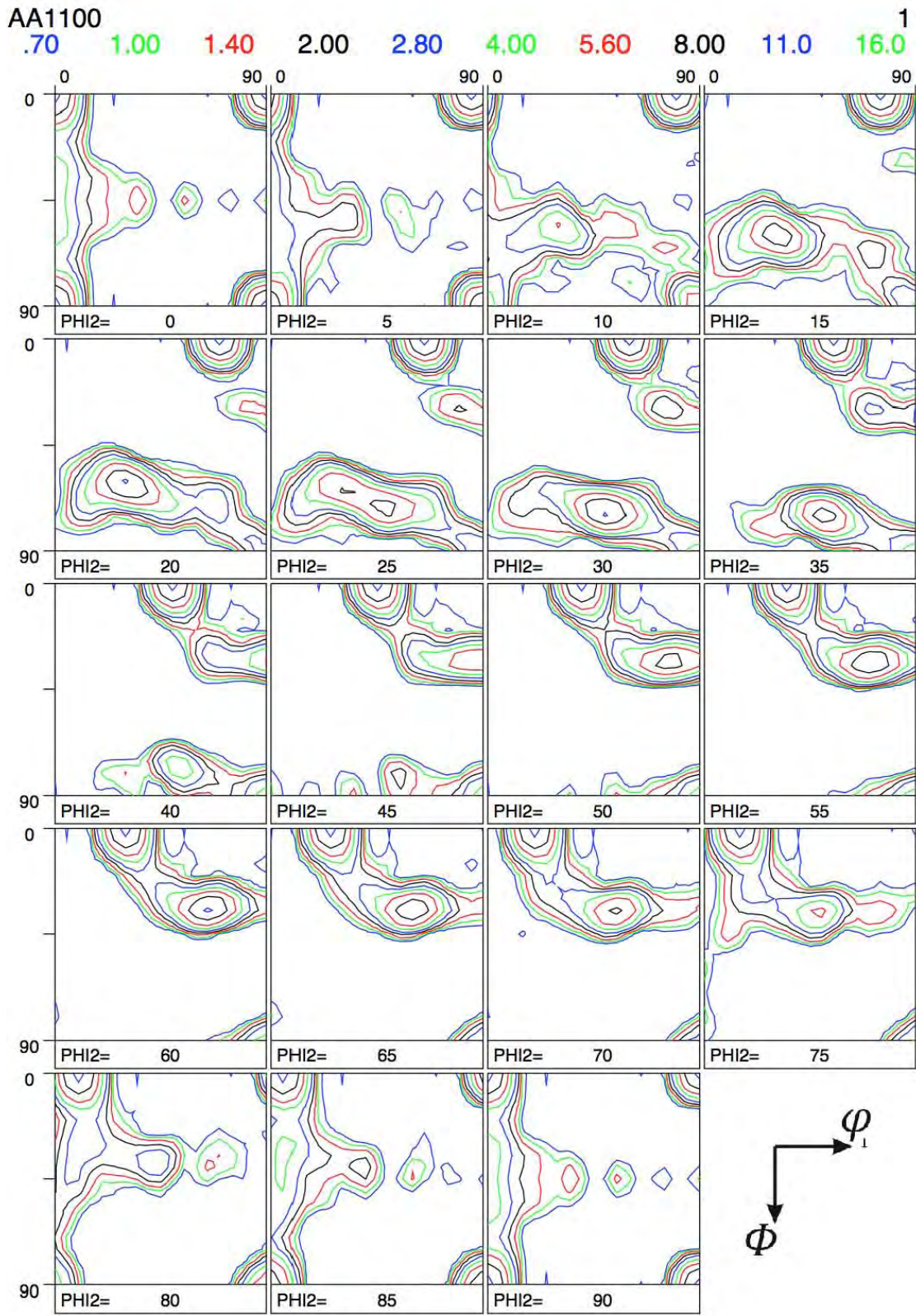
Figure 1.9 ODF for AA1100 (cold rolled)

So far, it has only been stated which crystal orientations, and in what amount, are present in the material, but not where they are located. Although this last information may appear redundant, is not. Grains with a given orientation may be distributed in different manners throughout the material (Fig. 1.10). As seen, cases a, b, and, c, do not necessarily produce the same mechanical response.

Fig. 1.10 Different positions for grains with a given orientation (blue). a) Contiguous in the microstructure. b) Located singly in the microstructure. c) In a different size class to the rest of the grains. d) Located in a special way with respect to the specimen, for example, near the surface. [20]
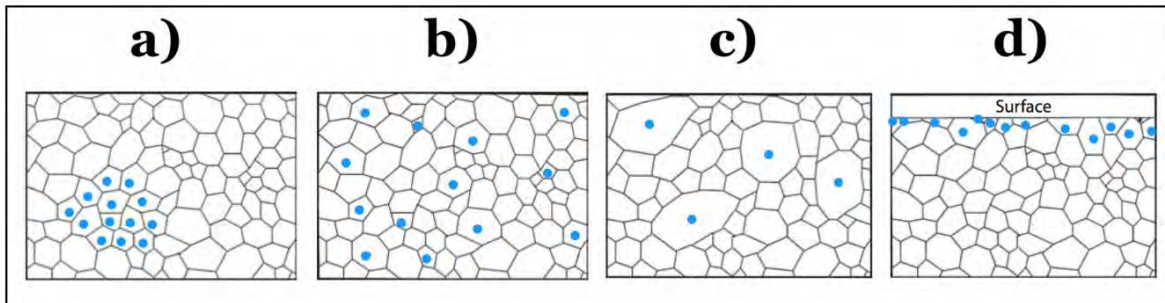
This concept, meaning including spatial location in a description of grain orientation, is known as micro texture [20]. Although it is usually reserved for finer and more complicated analysis, it may give an answer as to why analysis with a normal ODF (Eq. 1.24) may not yield accurate results, particularly for analyses that take place in relatively small areas.

1.3 Crystal plasticity

A polycrystal material response to an applied load depends on multiple factors that are related to the material microstructure. Therefore, to describe a complex material behaviour, such as plastic anisotropy, microstructural effects need to be considered and a continuum approach is no longer sufficient. A hierarchical multiscale theory proposes to employ theories at different scales, hence the multiscale name, to provide a more complete description of the phenomena studied. In one of the most common multiscale plasticity theories, only two scales are studied:

a) _**macro-scale**_: employs a continuum plasticity theory (Section 1.1)
b) _**meso-scale**_: employs a crystal plasticity theory

Crystal plasticity is a theory that seeks to explain the behaviour of single or multiple crystals under applied loads or imposed strains. In this section, a brief review of the most important concepts in this theory will be given, starting with a single grain response, and proceeding to more complex models that consider multiple grains. This theory allows for the formulation of a local constitutive law, which establishes relationships between local stress, strain, and rigid body rotation inside the representative volume element (RVE) [24, 29]. For the sake of simplicity, all the models discussed in this section will neglect elastic strain. The theories mentioned here contemplate a homogenous, single phase material; factors such as grain size or the presence of heterogeneities are not considered.

1.3.1 Schmid's law

The plastic deformation of a single crystal is caused by the sliding of parts of the crystal along certain crystallographic planes and directions. Generally, slip occurs more easily in the plane of greatest atomic density (slip plane) and in the closest packed direction within the slip plane. For a grain with an FCC crystalline structure, there are 4 compact planes ({111} planes), each one with 3 compact directions (<110> directions) as seen in Fig. 1.11. In consequence, there are 12 slip systems ({111}<110>=4x3=12) for this type of crystalline structure.
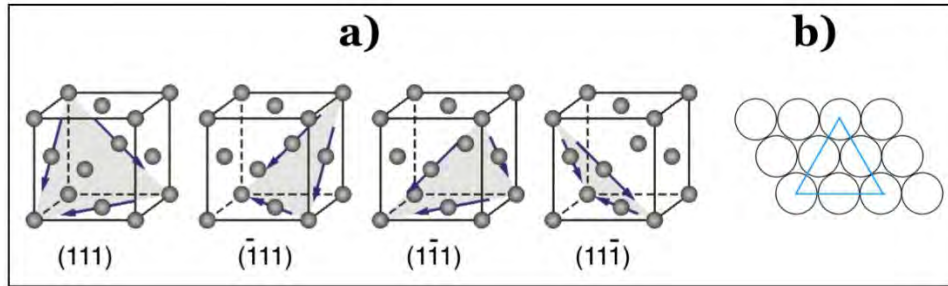
Fig. 1.11 FCC slip planes and directions [26]

Schmid's law indicates that slipping occurs when the shear stress applied reaches a critical resolved value ($\tau = \tau_{crss}$). For uniaxial loading, this law is expressed as Eq. 1.26, where its parameters can be identified in Fig. 1.12
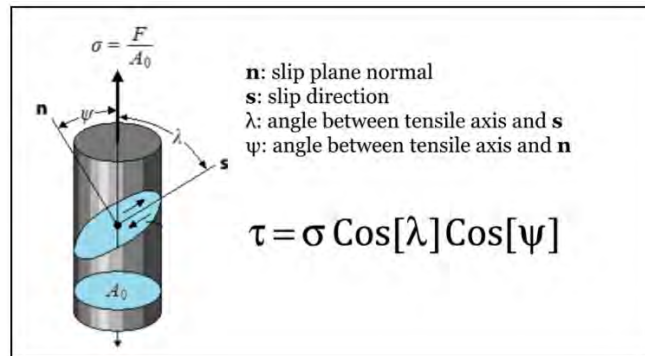
Fig. 1.12 Schmid's Law. Adapted from [27]

Despite the useful information provided, uniaxial loading is seldom found. Therefore, Schmid's law may be written in its tensorial form (Eq. 1.27). For this equation, $\hat{\mathbf{i}}_1$, $\hat{\mathbf{i}}_2$, and $\hat{\mathbf{i}}_3$ are unit vectors along the [100], [010], [001] crystallographic axes, respectively.

Eq. 1.27

$$\tau_{ns} = l_{ni} l_{sj} \sigma_{ij}$$

Where:

$$l_{ni} = \mathbf{n} \cdot \hat{\mathbf{i}}_i$$
$$l_{sj} = \mathbf{s} \cdot \hat{\mathbf{i}}_j$$

Schmid's law in tensorial form may be also expressed using an orientation matrix $\mathbf{M}^{(s)}$ associated with the $\mathbf{s}$ slip system (Eq. 1.28).

$$\tau^{(s)} = \mathbf{M}^{(s)} : \mathbf{s}$$

$$\mathbf{M}^{(s)} = \frac{1}{2}[\mathbf{b}^{(s)}\mathbf{n}^{(s)} + \mathbf{n}^{(s)}\mathbf{b}^{(s)}]$$

$$\mathbf{M}^{(s)} = \begin{pmatrix} M^{(s)}{}_{11} & M^{(s)}{}_{12} & M^{(s)}{}_{13} \\ M^{(s)}{}_{21} & M^{(s)}{}_{22} & M^{(s)}{}_{23} \\ M^{(s)}{}_{31} & M^{(s)}{}_{32} & M^{(s)}{}_{33} \end{pmatrix}$$

Where:

$\mathbf{b}^{(s)}$: unit vector in the direction of the Burgers vector

As seen, the attained shear stress depends on the orientation of the single crystal to the applied load. Consequently, a single crystal is anisotropic by nature.

1.3.2 Single crystal rotation

The rotation of grains in a polycrystalline material is responsible for the texture generation in deformation processes, such as rolling. In consequence, this rotation is the cause of the observed anisotropy. For simplicity, only the mechanism of a single grain rotation, using a tensile test, is explained [15].

a) During the test, the specimen cannot experience uniform glide on every slip system because it is constrained at its ends (Fig. 1.13).
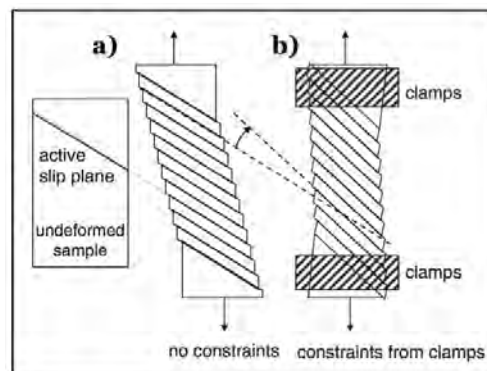
Figure 1.13 a) Tensile test of an unconstrained single crystal. b) Tensile test of a constrained single crystal [15]

b) Due to the imposed deformation, the crystal starts deforming on one slip system.
c) To accommodate the difference between this shear deformation and the imposed elongation, the crystal lattice rotates, and the strain is accommodated in another slip system. This rotation depends on the activated slip systems and the imposed deformation.

For a polycrystal, the description is somewhat more difficult, since the grain rotation is constrained by other grains that are moving as well. The rotation of the crystals remains active throughout the plastic deformation process, and the texture changes continuously, in what is called texture evolution. The resulting preferred crystal orientation depends on the initial texture, the plastic flow path, and the crystal structure.

1.3.3 Polycrystal models

Iso stress model

The iso stress model, first proposed by Sachs [72], starts from the assumption that all the crystals in the material experience the same stress. Therefore, if these grains are oriented in different ways, and according to Eq. 1.28, each one experiences different amounts of plastic deformation. All grains are in mechanical equilibrium but there is no strain compatibility. This model has been found to provide poor texture predictions for moderate to large strains and is no longer used [24].

Iso strain model and other variants

The iso strain model has evolved over the decades into different variants. The original iso strain model, Full Constrains Taylor (FC Taylor), is based on two hypotheses. The first one is that the imposed macroscopic plastic deformation ($\boldsymbol{\varepsilon}_R$) is the same as the plastic deformation experienced by the grains ($\boldsymbol{\varepsilon}_r$), which may be written as Eq. 1.29a, or Eq. 1.29b

Eq. 1.29a

$$d\boldsymbol{\varepsilon}_R = d\boldsymbol{\varepsilon}_r$$

Eq. 1.29b

$$\mathbf{D} = \mathbf{d}$$

This equation may be further developed using the definition of the velocity gradient tensor of the crystal ($\mathbf{l}$) (Eq. 1.30).

Eq. 1.30

$$\mathbf{l} = \sum_{s=1}^{N} \mathbf{b}^{(s)}\mathbf{n}^{(s)} \, d\gamma$$

Where:

N: available slip systems

$d\gamma$: slip rates

This tensor may be decomposed into its symmetric ($d\boldsymbol{\varepsilon}_r$) and skew-symmetric part ($\mathbf{w}$):

Eq. 1.31

$$\mathbf{l} = Sym[\mathbf{l}] + Skew[\mathbf{l}]$$

Eq. 1.32

$$Sym[\mathbf{l}] = \mathbf{d} = d\boldsymbol{\varepsilon}_r = \sum_{s=1}^{N} \frac{1}{2}[\mathbf{b}^{(s)}\mathbf{n}^{(s)} + \mathbf{n}^{(s)}\mathbf{b}^{(s)}]d\gamma^{(s)}$$

Eq. 1.33

$$Skew[\mathbf{l}] = \mathbf{w} = \sum_{s=1}^{N} \frac{1}{2}[\mathbf{b}^{(s)}\mathbf{n}^{(s)} - \mathbf{n}^{(s)}\mathbf{b}^{(s)}]d\gamma^{(s)}$$

Using Eq. 1.28 and Eq. 1.32, Eq. 1.29a may be rewritten as Eq. 1.34:

$$d\varepsilon_R = \sum_{s=1}^{N} \mathbf{M}^{(s)} d\gamma^{(s)}$$

The imposed macroscopic plastic deformation is not associated with the change of volume, therefore Tr(dε_R) = 0, which leaves only 5 independent components. Thus, only 5 of the 12 possible slip systems are used (Eq. 1.35)

$$d\varepsilon_R = \sum_{s=1}^{5} \mathbf{M}^{(s)} d\gamma^{(s)}$$

Eq. 1.35 shows that by using the Taylor factor (M) (Ec. 1.28), the macroscopic plastic strain increment can be expressed in terms of the slip rate. Hence it is a factor that relates microscopic and macroscopic flow properties [15]. However, a large combination of the possible slip systems that can be used in Eq. 1.35 exist. Due to this, Taylor proposed a second hypothesis, which states that the five glide systems chosen should be the ones that minimise plastic work (Eq. 1.36)

$$Min[dW^P] = Min\left[\sum_{s=1}^{5} \tau_{CRSS}^{(s)} d\gamma^{(s)}\right]$$

As seen from Eq. 1.28, Taylor factor varies as a function of orientation, which is shown in Fig. 1.14.
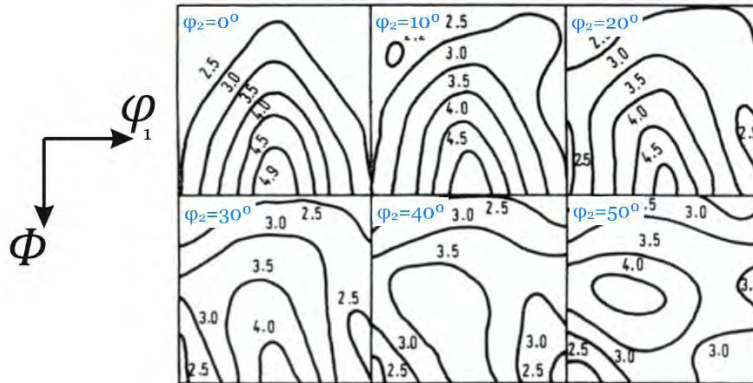
Fig. 1.14 Single crystal Taylor factor as a function of crystal orientation expressed by Euler angles (plane strain deformation). FCC metal [24]. The value of the Taylor factor will vary as the orientation of the crystal varies as well. For example, the value of M when the grain has an approx. (45°, 5°, 0°) orientation is 2.5.

An average Taylor factor, also called polycrystal Taylor factor, can be calculated using Eq. 1.37

$$\bar{M} = \int M(g) f(g) dg$$

FC Taylor proposes a local constitutive law given in terms of a kinematical equation and an energetic assumption or restriction. As such, it is an upper-bound approximation and overestimates the amount of work required to impose the plastic deformation. This will happen as well for other models derived from this crystalline approximation (Taylor-type models).

One of such derived models is called Relaxed Constrains Taylor (RC Taylor). The main difference between FC and RC Taylor, is that the latter does not forcibly impose the restriction that all the components of the polycrystal and local strain rate tensors are the same, leaving one or more components free (Eq. 1.38). This is called a relaxation.

<div align="right">Eq. 1.38</div>

$$\mathbf{d} = \mathbf{D} - \sum_{r=1}^{R} \widetilde{\mathbf{T}}_r \, \dot{\gamma}_r^{RLX}$$

Where:

$\widetilde{\mathbf{T}}_r$: symmetric tensor associated with the type of relaxation

$\dot{\gamma}_r^{RLX}$: relaxation shear rates

In this model, two types of relaxation are possible, R=1 (where $\widetilde{\mathbf{T}}$ is defined as Eq. 1.39a), and R=2 (where $\widetilde{\mathbf{T}}$ is defined as Eq. 1.39b).

<div align="right">Eq. 1.39a</div>

$$\widetilde{\mathbf{T}}_1 = \begin{bmatrix} 0 & 0 & 1/2 \\ 0 & 0 & 0 \\ 1/2 & 0 & 0 \end{bmatrix}$$

<div align="right">Eq. 1.39b</div>

$$\widetilde{\mathbf{T}}_1 = \begin{bmatrix} 0 & 0 & 1/2 \\ 0 & 0 & 0 \\ 1/2 & 0 & 0 \end{bmatrix} \text{ and } \widetilde{\mathbf{T}}_2 = \begin{bmatrix} 0 & 0 & 0 \\ 0 & 0 & 1/2 \\ 0 & 1/2 & 0 \end{bmatrix}$$

For this model, it is assumed that the crystals possess an elongated shape, and therefore, the types of relaxation mentioned before do not cause incompatibilities. Additionally, the relaxations are defined in such a manner that they do not contribute energy to the system.

Cluster models

Although RC Taylor is not applicable to all grain geometries, its proposed concept of relaxation is used in other successful models, like the Advanced LAMEL. This model belongs to a type of crystalline approximations called cluster models, which consider two or more crystals and their interaction, instead of the FC/RC Taylor single grain. Additionally, this model is not restricted by grain geometry as its predecessor.

The Advanced LAMEL crystalline approximation, or ALAMEL, considers a cluster consisting of two grains (grain 1 and grain 2, or x=1, 2) and a boundary between them [25, 28, 29]. A coordinate system is defined using this boundary, where the y_3 axis is commonly defined as normal to the grain boundary surface. ALAMEL stems from the consideration that, although compatibility between grains is necessary, there may be a strain gradient inside a grain. With these considerations, the velocity gradient of each of the crystals may be written as Eq. 1.40.

Eq. 1.40

$$\mathbf{l}_1 = \mathbf{L} + \sum_{r=1}^{R} \widetilde{\mathbf{A}}_r \, \dot{\gamma}_r^{RLX}$$

$$\mathbf{l}_2 = \mathbf{L} - \sum_{r=1}^{R} \widetilde{\mathbf{A}}_r \, \dot{\gamma}_r^{RLX}$$

Where:

$\mathbf{L}$: macroscopic velocity gradient tensor

$\dot{\gamma}_r^{RLX}$: relaxation shear rates

$\widetilde{\mathbf{A}}_r$: tensor associated with the type of relaxation

r: relaxation mode

In a similar fashion to Eq. 1.31 and Eq. 1.38, the local strain increment for each grain, Sym[$\mathbf{l}_1$] and Sym[$\mathbf{l}_2$], is defined as Eq. 1.41:

Eq. 1.41

$$Sym[\mathbf{l}_1] = \mathbf{d}_1 = d\boldsymbol{\varepsilon}_{r1} = \sum_{s=1}^{N} \mathbf{M}^{(s)}\dot{\gamma}^{(s)}{}_1 + \sum_{r=1}^{2} \tilde{\mathbf{E}}_r \, \dot{\gamma}_r^{RLX}$$

$$Sym[\mathbf{l}_2] = \mathbf{d}_2 = d\boldsymbol{\varepsilon}_{r2} = \sum_{s=1}^{N} \mathbf{M}^{(s)}\dot{\gamma}^{(s)}{}_2 - \sum_{r=1}^{2} \tilde{\mathbf{E}}_r \, \dot{\gamma}_r^{RLX}$$

Where:

$\tilde{\mathbf{E}}_r$: is the symmetric part of $\widetilde{\mathbf{A}}$

As has been stated, the local constitutive law is also given in terms of an energetic assumption. For this case, the minimum plastic work condition (Eq. 1.36) must be fulfilled for the energy sum in both grains.

1.4 The hierarchical multiscale software (HMS)

The Hierarchical Multiscale Software (HMS), is a polycrystalline plasticity finite element code developed at KU Leuven with the main objective of providing a computationally feasible solution to predict anisotropic plastic behaviour. For this purpose, it employs a statistically representative sample of texture and multiscale modelling [10].

One of the main characteristics of HMS is the implementation of the Facet method to obtain an analytical expression of the yield locus. The procedure is as follows:

a) *Calculation of points of the discrete yield locus:* By using micro mechanical models, either ALAMEL or FC Taylor, the corresponding yield stresses to a given set of strain rate modes are obtained. Texture is accounted for in the form of a discrete ODF. The use of these virtual experiments allows to obtain points the entire stress or strain rate space, without the use of interpolation functions.

b) *Analytical expression of the continuous yield locus:* The unknown coefficients of the Facet function (Section 1.1.5) are fitted to the data points calculated in the previous step. This provides a continuous description of the yield locus in 5 dimensions.

c) HMS receives hardening laws as input to include material hardening in its predictions, by multiplying the locus calculated in the former step by the magnitude of the yield stress obtained from a uniaxial tensile test.

The procedure described before gives HMS an advantage over two of the main approaches used to determine anisotropic plastic behaviour. On one hand, the limitations of the phenomenological approach are overcome using virtual experiments. On the other hand, it is computationally much more efficient than full field approaches, where every grain is modelled at every integration point of the finite element model [24, 30]. Additionally, HMS can predict texture evolution and use this information to update the corresponding yield function at every 5% or 10% accumulated plastic strain [31]. A summary of HMS workflow is given in Fig. 1.15.
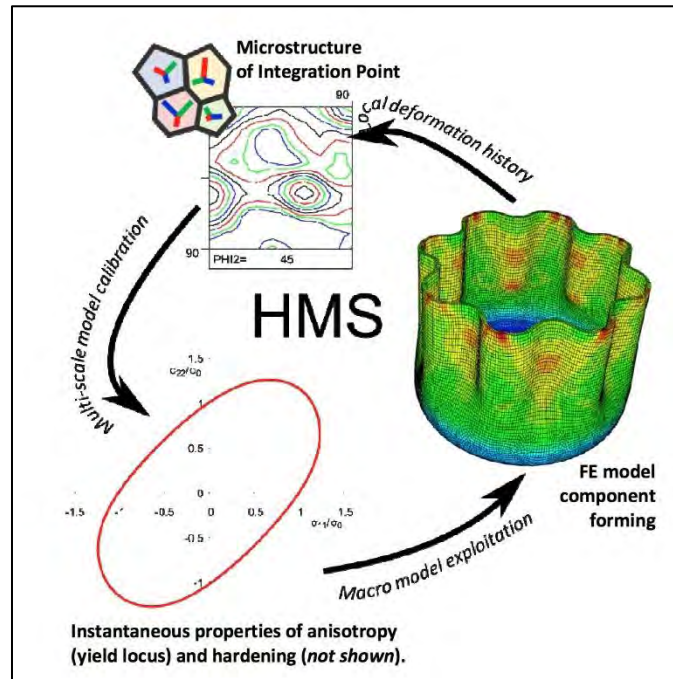

Fig. 1.15 HMS workflow [11]

1.5 Vickers hardness test

During the Vickers hardness test, a sample is indented with a pyramidal shaped diamond indenter (Fig. 1.16a) and the resulting indentation diagonals are measured (Fig. 1.16b).
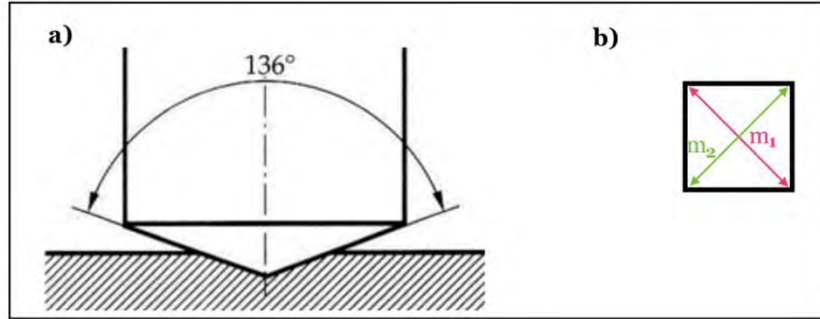
Figure 1.16 a) Vickers indenter and idealised indentation shape [32]. b) Indentation diagonals

The obtained hardness is quantified by a Vickers hardness number, or HV (Eq. 1.42)

$$HV = 1854.4 \frac{P}{m^2}$$

Where:

P: load [g_f]
m: mean indentation diagonal [µm]

As long as the indentation shape follows the geometry presented in Fig. 1.16 closely, and there is no elastic recovery, the expression for the indentation depth can be calculated as Eq. 1.43.

$$d_i = \frac{m}{2\sqrt{2}Tan\left[\frac{\theta}{2}\right]}$$

Where:

d_i: inferred indentation depth
θ: 136°

In reality, there is a certain degree of elastic recovery and the material piles up or sinks in around the indentation, resulting in shapes like the ones presented in Fig. 1.18. Consequently, Eq. 1.43 needs to be corrected to account for these phenomena [33]
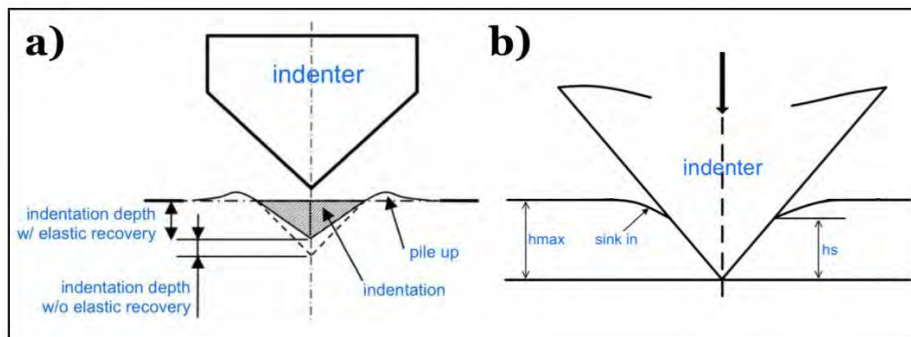

Figure 1.17 Indentation shapes a) Pile up, adapted from [34]. b) Sink in, adapted from [35]

1.5.1 Instrumented Vickers hardness test

Instrumented indentation (IIT), stems from the same principle as the one described previously, except for the fact that depth and load are recorded as the indentation is made. The resulting curve is similar to the one shown in Fig. 1.18.
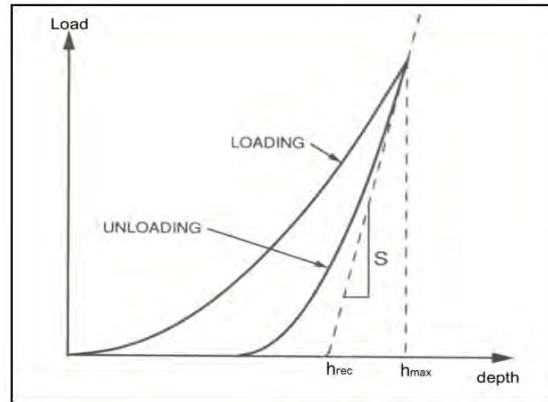

Figure 1.18 Depth vs load curve [36], also called the P-h curve.

Two main stages are present in the indentation curve; loading and unloading. The former one contains information about elastic and plastic behaviour, while the latter contains, ideally, only information about elastic recovery. In reality, the latter part includes the indenter behaviour as well. Nonetheless, the final depth can be obtained by separating these two effects by using linear fitting and extrapolation.

Extensive work has been done to correlate results obtained by means of IIT with material properties or behaviour [37, 38, 39]. This is of special importance for materials or coatings which cannot be tested by traditional means. It is useful as well to characterise material surface properties after a surface treatment.

To analyse and interpret a P-h curve is not a trivial task. Beyond difficulties inherent to the method [40], other modelling problems remain. At the present moment, a complete analytical description of the P-h curve for elasto-plastic materials has not yet been obtained. For this kind of materials, and a self-similar indenter, the loading part of the indentation curve can be approximated as Eq. 1.44:

Eq. 1.44

$$P = Ch^2$$

Where:
C: function of material properties and indenter geometry
h: depth

Dimensional analysis can be used to determine which material properties and indenter characteristics affect C, as well as the reason behind a square exponent for h [43]. FEM has been used to obtain the influence that E (Young's Modulus), Y (Yield strength), and n (work hardening exponent for Hollomon law) have in the indentation curve (Fig. 1.19).
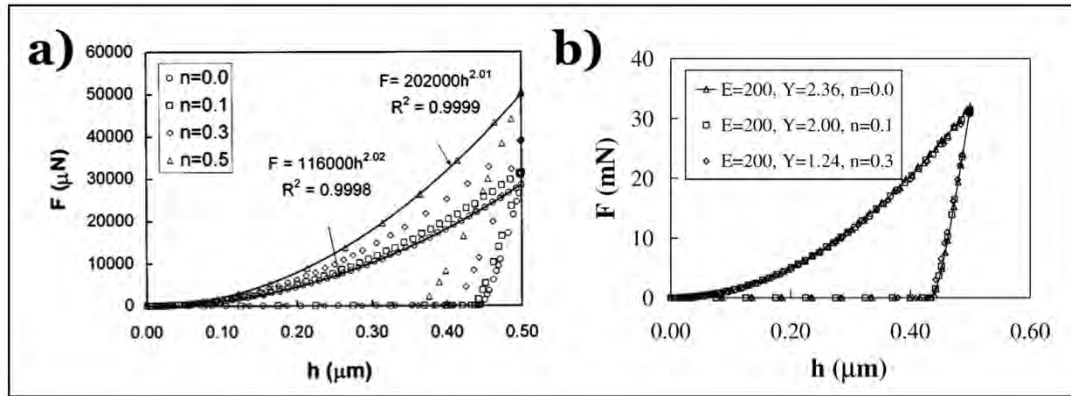
Figure 1.19 a) P-h curves with varying n (E=200GPa. Y=2[GPa], v=0.33) [41]. b) P-h curves with varying E, Y, and n [42]

Regarding work hardening behaviour, it was known that the amount of its effect on the indentation curve is inversely proportional to the Y/E ratio [43]. For pile up and sink in, their relation to material behaviour is not yet fully understood, however, it is considered too a function of Y/E and hardening behaviour [43].

1.5.2 FEM modelling of the instrumented Vickers hardness test

FEM replication of IIT is mainly used to quantify the influence of certain parameters on the experimentally obtained results. This allows to finetune analytical or empirical models that describe the material properties that intervene during IIT. It serves for the reverse modelling and visualisation of stress and strain fields as well.

This section provides an overview of the main difficulties in reproducing an IIT by FEM, which coincidently are the most common sources of deviation between experimental and FEM results. The list presented here is based on the work by Marteau et al (2015):

a) *FEM model dimensionality:* Refers as whether the FEM model is constructed in 2D or 3D. Depending on the type of information one is trying to extract, it may be advisable or not. For materials with complex structures, where indentation shape and stress/strain distributions may be of interest, this simplification induces significant errors. For indenters which are not axisymmetric, like Vickers, this simplification is not possible.

b) *Boundary conditions:* It was found that completely restricting the movement of boundary nodes, as opposed as partially restraining them, led to increases in the overall model stiffness. This effect may disappear if the model is large enough compared with the indentation. This is in fact a general problem in finite element modelling.

c) *Mesh characteristics:* The mesh should be fine enough to guarantee an appropriate contact without compromising computing resources. The size of the simulated pile up and sink depends on the type of mesh employed. It should be assured that the obtained results are independent from the mesh employed.

d) *Material behaviour laws:* Inappropriate choice of the behaviour law results in a deviation of practically all the observed output parameters.

e) *Friction coefficient:* Although the choice of friction coefficient has apparently no effect on the P-h curves, it may influence pile-up and sink-in effects. This effect is mainly noticeable at µ>=0.4, and for materials that harden significantly during indentation.

f) _Indenter type:_ Tip roundness results in a decrease of indentation depth due to a flat spot formation. This defect only affects the loading part of the P-h curve and is more visible at low indentation loads. It affects the determination of contact area as well. A flat-nosed tip may also cause deviations in the indentation curve; for large tip radii, the indentation depth for a given load is smaller than its counterpart with a sharp tip.

Other sources of deviation are due to factors which are beyond the FEM model. They include defects originating from the sample preparation, determination of the contact zone, and the indentation size effect (ISE). This last concept refers, in simple words, to the observed increase of hardness for small indentation depths.

1.6 Materials characterisation

Material characterisation techniques aim to provide information concerning different aspects of a sample, including chemical composition, microstructure, crystallographic orientation, micro texture and mechanical/chemical/physical properties. For this section, only some of the techniques used to obtain morphological information of an indented sample are discussed.

1.6.1 Optical profilometry

Optical profilometry is a widely used technique to characterise the sample surface. It can be carried out using either interferometry methods or the chromatic confocal principle. The latter principle is explained as follows [44, 45]:

a) White light is decomposed into different wavelengths using an optical pen, which is an array of lenses with different refractive index and high degree of chromatic aberration.
b) The variation in the lenses refractive index causes a variation of the focal distance for each wavelength, which focus at different distance from the final lens.
c) When scanning a sample, the distance of the sample to the final lens varies, since it is not perfectly smooth. Consequently, the wavelength that is in focus varies (Fig. 1.20).
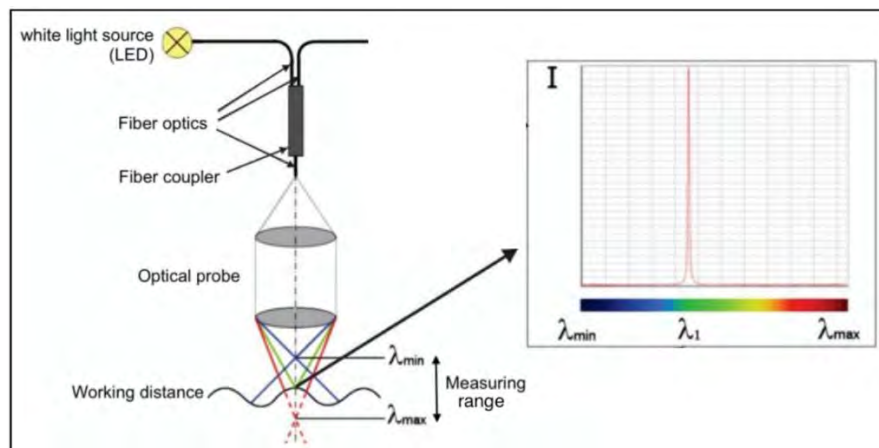

Figure 1.20 Optical profilometry by chromatic confocal principle. Adapted from [45]

d) The light is reflected from the sample to the optical pen, and using a pin hole filter, only the focused wavelength makes it to a CCD spectrometer.

e) This spectrometer indicates which wavelength is focused, which allows to determine the distance of the measured point to the final lens. Knowing the optical characteristics of the system, the surface topography can be reconstructed.

1.6.2 Atomic force microscopy

Atomic Force Microscopy, or AFM, is an imaging technique that employs a probe, consisting of a sharp tip mounted on a flexible cantilever to obtain the specimen surface topography. As the sample is scanned, it induces the deflection of the cantilever. This deflection is correlated with changes in the Z position of the tip, and if these are recorded, a 3D profile of the surface can be obtained.

A feedback loop is used to control the forces between sample and probe. The deflection of the cantilever is measured by bouncing a laser off the back of the cantilever onto a position sensitive photodiode detector (Fig. 1.21a) [49]. Different AFM imaging modes exist depending on the separation between sample and probe (Fig. 1.21b). They are presented in Table 1.1.
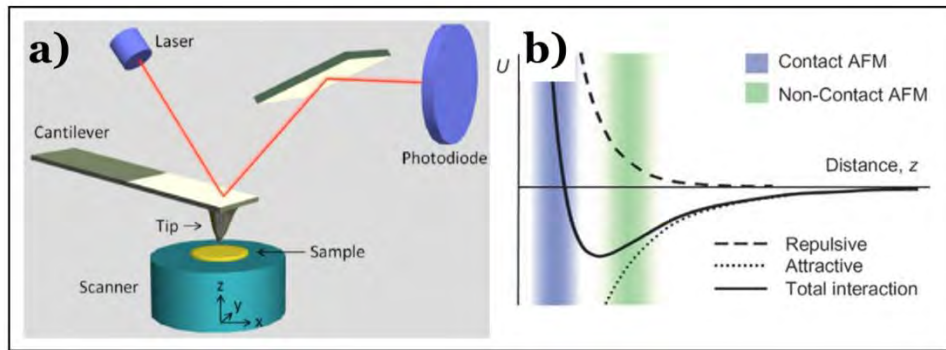

Figure 1.21.3 a) AFM schematic [50]. b) AFM imaging modes according to sample-probe separation [51]

Table 1.1 AFM imaging modes. Images from [51]

AFM imaging modes [40, 44]		
Contact (static)	**Tapping (dynamic)**	**Non contact (dynamic)**
• Tip touches the sample surface • Repulsive Van der Waals forces • Changes in deflection are measured • Surface or tip wear	• Cantilever is vibrated at its resonant frequency • Probe interaction with sample modifies the cantilever's oscillation • Changes needed to maintain frequency are measured	• Tip does not touch the sample surface • Attractive Van der Waals forces • Cantilever is vibrated at or above its resonant frequency • Separation changes necessary to maintain frequency are measured

Chapter 2. Methodology

The methodology was developed with the goal of distinguishing experimental factors and statistical errors from the effects induced by inaccuracies in the finite element model. This chapter explains the experimental procedure, while in Ch. 3 the FEM model development, validation, and HMS implementation is described.

Four alloys (AA6016T4, AA5005, AA3103, AA1100) were studied, using two different thicknesses for the first one. Throughout this work, these alloys will be referred with the following names (Table 2.1)

Table 2.1 Alloy names

Name	Alloy	
AA6016mm1	AAA6016T4	1.1mm thickness
AA6016mm2	AA6016T4	2.0mmm thickness
AA5005	AA5005	
AA1100	AA1100	
AA3103	AA3103	

The methodology here presented is divided in:
a) Material characterisation
b) Experimental procedure
c) Statistical analysis of experimental results
d) Comparison between experimental and FEM results

2.1 Materials characterisation

2.1.1 Physical and mechanical properties

The physical and mechanical properties of interest for all samples were **Young's** Modulus (E=70GPa), **Poisson's** ratio (v=0.33), and density (ρ=**2700** kg/m³) [55]. The values for mechanical properties such as yield stress, and parameters related to the hardening behaviour were considered in the hardening laws for each material. For this work, Voce hardening laws were employed (Fig. 2.1).
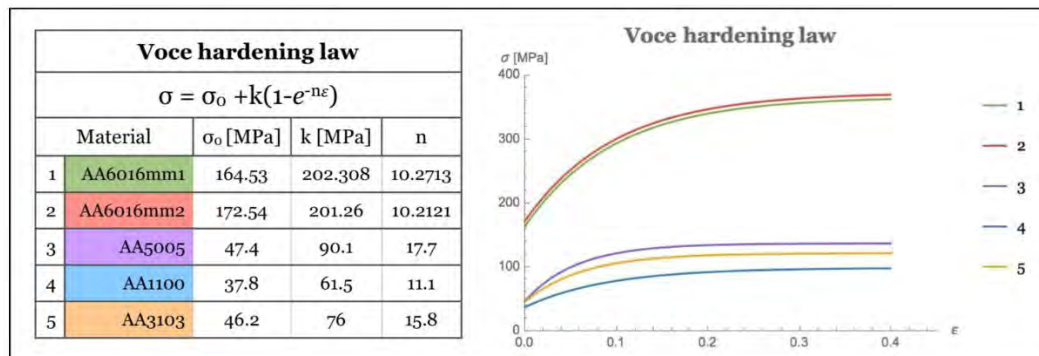

Voce hardening law			
$\sigma = \sigma_0 + k(1-e^{-n\varepsilon})$			
Material	σ_0 [MPa]	k [MPa]	n
1 AA6016mm1	164.53	202.308	10.2713
2 AA6016mm2	172.54	201.26	10.2121
3 AA5005	47.4	90.1	17.7
4 AA1100	37.8	61.5	11.1
5 AA3103	46.2	76	15.8

Figure 2.1 Voce hardening laws

2.1.2 Crystalline texture

Pole figures for all samples were acquired at KU Leuven using a Siemens 500 X-Ray diffractometer. Posteriorly, ODFs were reconstructed using the MTM-FHM software [56]. The corresponding orientation distribution functions are presented in Fig 2.2 through Fig. 2.6. Due to space constrains, only the most representative sections of each ODF are shown. The contour levels for all alloys are the same, to ease qualitative comparison between textures.
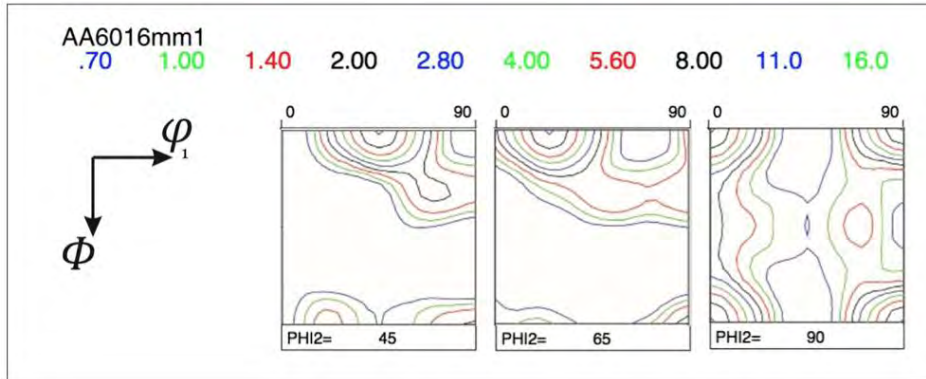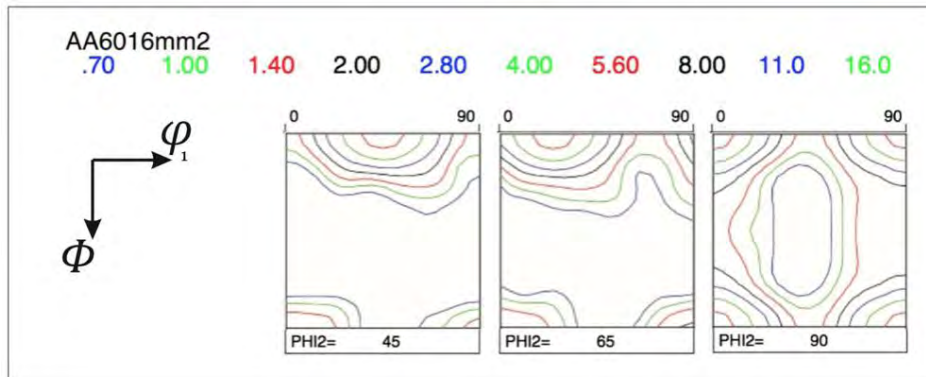

Figure 2.2 ODF for AA6016mm1
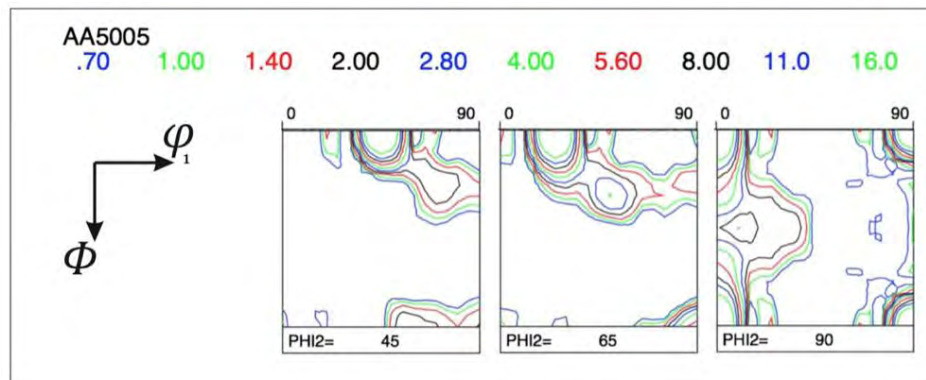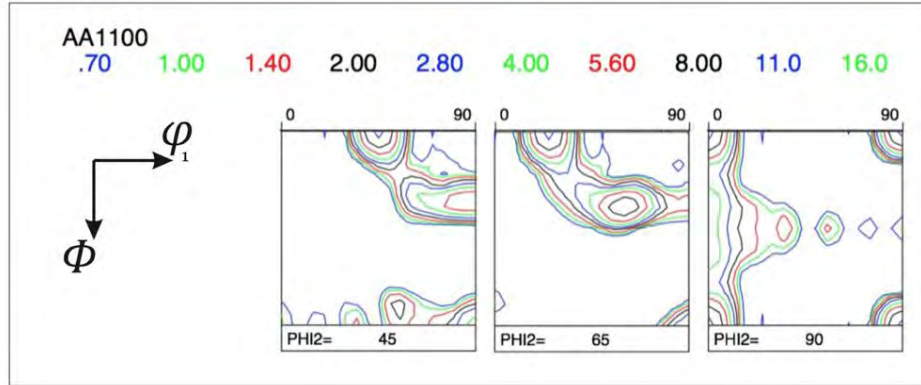

Figure 2.3 ODF for AA6016mm2

Figure 2.4 ODF for AA5005
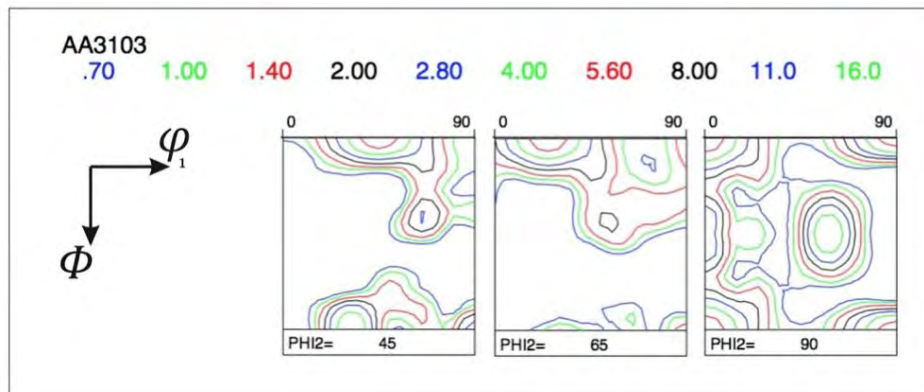
Figure 2.5 ODF for AA1100

Figure 2.6 ODF for AA3103

2.1.3 Yield loci sections

For all materials, initial yield locus section (σ_{11}-σ_{22}) was calculated using the ALAMEL micro mechanical model and the Facet function (Fig. 2.7). Isotropic homogenous hardening was assumed. The initial estimated yield stress in the RD direction (σ_{RD}) and yield stress in the TD direction (σ_{TD}) is given as well.

Yield stress [MPa]	
σ_{RD}	σ_{TD}
AA6016mm1	
164.530	162.173
AA6016mm2	
172.540	169.825
AA5005	
47.400	48.513
AA1100	
37.800	37.899
AA3103	
46.200	45.579
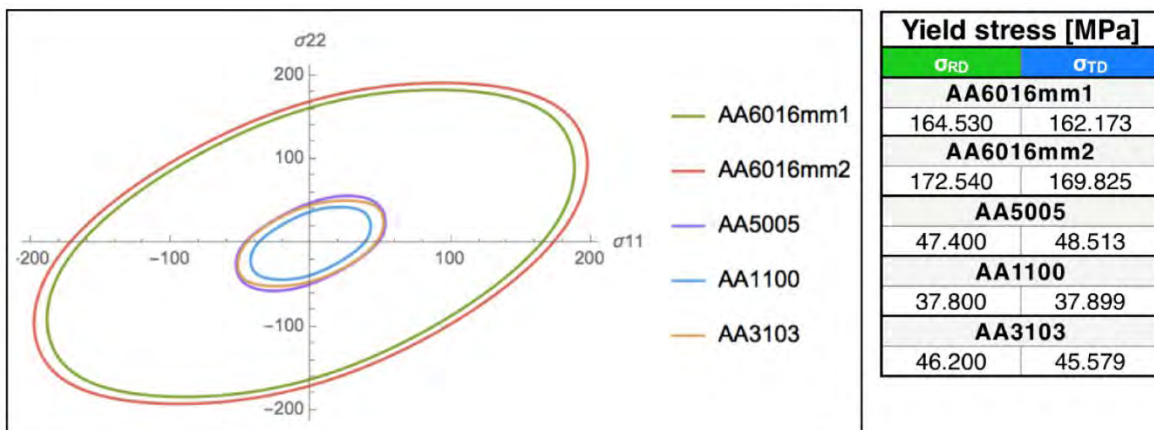
Figure 2.7 Initial yield loci sections and estimated σ_{RD} and σ_{TD} [MPa]

2.2. Experimental procedure

2.2.1 Instrumented indentation
Samples in each material direction (ND, RD, TD) were cut from larger sheets for all studied materials. They were resin mounted, ground, and polished according to ASTM E3 [57]. A Nanovea® micro indenter was used with the following parameters:
Load: 0.25N
Indentation speed: 0.25N/min
Unloading rate: 1N/min
Contact Load: 0.03N
Time at peak load: 10s (for stabilisation purposes)

Indentation depths (d_{Exp}) were obtained with an optical profilometer at the time of indentation (data acquisition frequency: 150Hz). Seven indentations were performed in each material direction for each material, obtaining seven raw indentation curves.

To quantify the amount of anisotropy, in terms of indentation depth, the coefficient of variation was employed (Eq. 2.1). This coefficient expresses the extent of relative variability in relation to the mean of the population, and is a measure of dispersion [58]

Eq. 2.1

$$CV = \frac{StandardDeviation[Mat]}{Mean[Mat]}$$

Where:
Mat: Set that contains indentation depths in all directions for a single alloy

2.2.2 Optical measurement of indentation diagonals
Since standard HV_{Exp} is defined by the direct measurement of the indentation diagonals (m_{Exp}) and not by other indirect approaches [59], optical measurement of these lengths was necessary. This was performed obtaining photographs of the indentations with an Axiocam ERc 5s camera and processing them using the Zen software, both by Zeiss®.

Additionally, an inferred indentation depth (d_{Expl}) was calculated from the indentation diagonals (Eq. 1.43) and compared to the indentation depth with elastic recovery (Section 2.3.3). The difference between them served to indicate whether the indentation shape followed the one indicated in Fig. 1.16 (ideal shape), or the one in Fig. 1.17 (non-ideal shape).

2.2.3 Indentation shape
To select the most appropriate indentation shape characterisation technique for this work, AFM and optical profilometry were compared. It was found that although measurements with the optical profilometer were faster, they presented a distortion at the corners of the indentation. Therefore, a Bruker Innova® AFM was used with the following parameters:
Mode: Contact
Tip: SNL-10
Resolution: 256x256
Scanning Frequency: 0.5Hz
Measurement area: 30µm^2

Only the most representative indentation for each direction in the AA6016 alloy was analysed. With the obtained results, Mathematica® was used to generate a mesh to compare with the one calculated by HMS. Using this mesh, two profiles were defined as the intersection of the indentation with two planes normal to each other (Fig. 2.8).
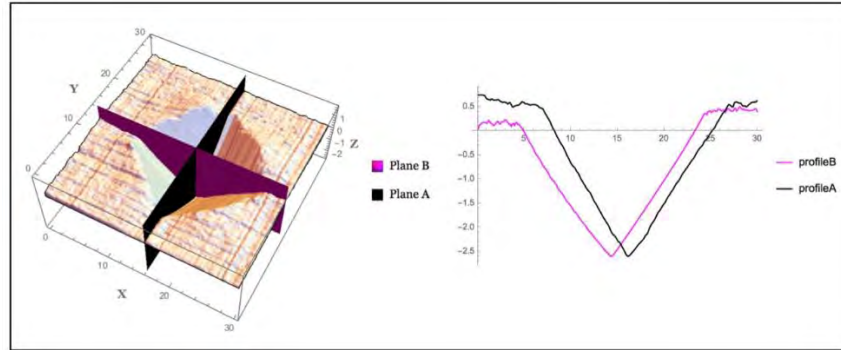

Figure 2.8 a) Planes A and B. b) Profiles on these planes

Plane A was defined as a plane which crosses the indentation at the point of minimum depth and had $\hat{\mathbf{i}}$ as its normal. Plane B was defined similarly, with $\hat{\mathbf{j}}$ as its normal. These profiles provided information concerning the symmetry and shape of the indentation.

2.3 Analysis of experimental results

2.3.1 Fitting and adjustment of experimental indentation curves

Adjustment and fitting of raw data was done before performing statistical analysis. The reason for the former was to determine the exact moment the indenter contacted the material. The latter was performed to fit the data with Eq. 1.44.

The procedure followed was based on the one described in [61], with the main difference being that it was carried out in the depth vs load curve instead of the load vs depth curve. One of the main characteristics of this method was that it tries to fit all experimental curves at the same time, i.e., a single fitting curve was constructed with the information from all experimental data.

Since the equipment started collecting data even before the indenter made contact with the base material, the contact load defined by the user was used to define the start of the filtered experimental curve. Next, the deviation from zero load was corrected with the contact load, and the experimental curve was smoothed. This smoothing left the curve with equidistant data points (load, depth), and limited the curve to the range from minimum maximum load common to all the curves. This was necessary because, although a 0.25N load was defined, the applied load usually varied within a small range (approx. +/- 0.05N).

Once this was done, a fitting function was defined (Eq. 2.2)

$$F_f = h_0 + \sqrt{\frac{P}{c_1}} + c_f P$$

Where:

h_0: initial indentation depth
P: load
c_1: hardness
c_f: frame stiffness

Its constants were determined using the data from all the smoothed experimental curves together. Thus, this fitted curve considered information from all the experimental curves. Then, the smoothed and reduced data were plotted against the fitting curve, and outliers were detected. The raw data corresponding to this outlier was eliminated and the whole process was run again. This was repeated twice, eliminating 2 outliers, and only five smoothed experimental data remained. These were referred to as reduced experimental indentation curves. Their fit was called fitting curve, and the corresponding depth obtained from this last curve was d_{ExpF}.

2.3.2 Statistical analysis

The statistical analysis here described had two main goals: to determine the indenter condition and to classify observed material behaviour.

Indenter condition

For the indenter condition it had to be determined whether it was acceptably pyramid shaped or not, since this could significantly affect the results. To rule out this, the following procedure was performed:

a) Measurement of indentation diagonals made with the indenter in its original position (Set 1).
b) Measurement of indentation diagonals made with the indenter at $\pi/2$ from its original position (Set 2).
c) The vertical diagonals from Set 1 were subtracted from the horizontal diagonals from Set 2. (Set 3). If the indenter was acceptably pyramid shaped, there should be no significant difference between the vertical diagonals from Set 1 and the horizontal diagonals from Set 2. Therefore, the mean of Set 3 **shouldn't** be significantly different from 0.

A T-Test was done for two alloys (AA5005 and AA6016mm1), with significance level at 0.05. The null hypothesis stated:
Ho: _There is no difference between the sample and a sample with a perfect indenter._

Table 2.2 Indenter condition

Statistical analysis		
Whether the indenter was perfectly pyramid shaped and its impact on the measurements		
Ho: _There is no significant difference between the sample and a sample with a perfect indenter._		
Material	Result	Consequence
AA6016mm1	Null hypothesis accepted	Pyramid shaped indenter
AA5005	Null hypothesis accepted	Pyramid shaped indenter

The results showed that the null hypothesis was accepted for both materials. Therefore, it was concluded that the indenter was acceptably pyramid shaped. Since according to Section 1.5.2, indenter sharpness affects results, it was verified using AFM (Fig. 2.9).
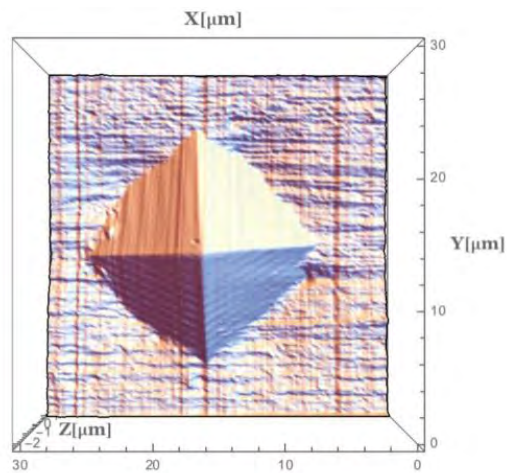

Fig. 2.9 Indenter sharpness

Material behaviour

Statistical analysis regarding material behaviour was done in terms of d_{Exp}. It was of interest to see whether the difference in terms of d_{Exp} between each direction (ND, RD, TD) was significant. The idea was to quantitatively determine whether the material could be considered anisotropic or not for indentation purposes. To observe if there was any significant difference between d_{Exp} in one direction and the others, an Analysis of Variance (ANOVA) was proposed. This method allows to observe if there is a significant variation in a set and associate this variation with a variable in the process or phenomena. In this case, ANOVA served to determine if the observed variation in d_{Exp} for each direction was due to the material direction or merely a coincidence.

For this test, the null hypothesis stated:

Ho: *There is no relationship between the variation in d_{Exp} for each direction and said direction. The variation is due to random effects.*

For the case at hand, the variance of a set only containing d_{Exp} in a certain material direction was compared to a set containing all d_{Exp}, regardless of direction. If the material was isotropic, there should be no significant difference between variance of one direction set and the variance of all directions. This meant, for practical purposes, it did not matter whether the measurements were taken in ND, RD or TD. Therefore, the acceptance of the null hypothesis also implied there was no significant difference for d_{Exp} between directions, and in consequence, the material was considered isotropic.

For the implementation with Mathematica®, the built-in ANOVA function was used. The input was an array containing pairs. The first member of the pair was the direction (ND:1, RD:2, TD:3), while the second one was the d_{Exp}. The significance level was set at 0.1

2.3.3 Elastic recovery

To obtain the change in indentation depth due to elastic recovery, the unloading section of the indentation curve was employed. This section was divided in two parts, easily identified by a slope change, with only the first part being of interest. Assuming a linear elastic behaviour, it was possible to use these data to estimate the depth corresponding to a full elastic recovery (load=0 N) using linear extrapolation (Fig. 2.10)
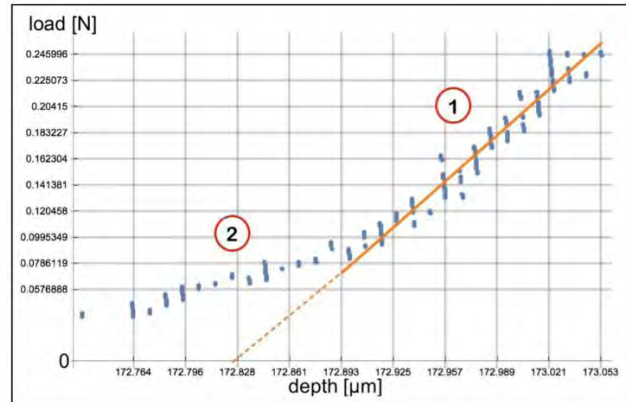

Figure 2.10 Change in indentation depth due to elastic recovery. The two different parts of the unloading section of the indentation curve can be identified. Raw data in blue. Linear fitting in solid orange. Inferred indentation depth in dashed orange.

Raw data of the corresponding reduced indentation curves was used for this approach and fitted to a linear function. Then, the corresponding indentation depth at zero load, i.e. indentation depth with recovery (d_{ExpR}), was obtained.

2.4 Comparison between experimental and HMS results

Comparison between experimental and HMS results was done in terms of depth, HV, and indentation shape.

2.4.1 Indentation depth

Reduced experimental indentation curves were qualitatively compared with the ones obtained with HMS. A quantitative analysis was performed as well to verify if the depth predicted by HMS (d_{HMS}) was comparable to the sets of experimental indentations performed on the material using the T-test with significance level established at 0.1. The null hypothesis for this test stated:

H0: *There is no significant difference between the HMS depth prediction and the experimental data.*

Additionally, CV_{HMS} for each alloy was calculated (Eq. 2.1) and qualitatively compared with CV_{Exp}. The aim was to verify whether HMS predicted the same amount of anisotropy.

2.4.2 HV

HV_{Exp} was compared to the one predicted by HMS (HV_{HMS}). The T-Test was used as well with the following null hypothesis:

H0: *There is no significant difference between the HMS HV prediction and the experimental data.*

2.4.3 Indentation shape

The shape predicted by HMS was qualitatively compared to the one reported by AFM using contour plots for the plan view. The aim of this was to visualise the material distribution by the indentation (pile ups or sink ins) and the squareness of both indentations profiles. This was only performed for the AA6016 alloy.

Chapter 3. FEM model

An isotropic FEM model was first developed for its posterior implementation with HMS. In this model, verification of the influence of some of the parameters mentioned in Section 1.5.2 was analysed. Next, HMS simulations were prepared and executed in a workstation.

3.1 FEM model

3.1.1 Description

The FEM model used for this work was a three-dimensional representation of 1/4 of a Vickers indenter and 1/4 of base material (Fig. 3.1), built in Abaqus CAE®.
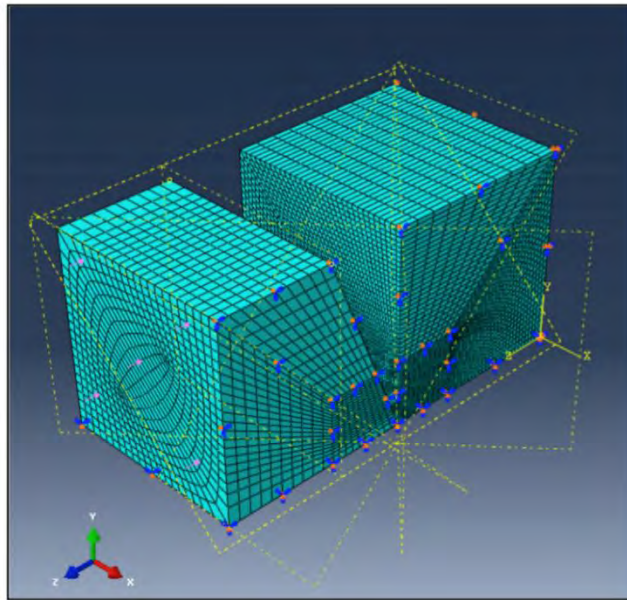

Figure 3.1 FEM model

This model was based on the one presented in [62]. Main features of the latter include:
a) ***Mesh composed by elements with 3:1 aspect ratio:*** to maintain an acceptable aspect ratio throughout the simulation and reduce hourglassing.
b) ***Asymmetric mesh:*** to avoid artefacts that appear due to an equal number of nodes in the indentation zone enter in contact with the indenter at the same time.
c) ***Smooth loading curve:*** to prevent sudden energy jumps in the elastic-plastic transition that appear when a linear load curve is employed.
d) ***Optimisation of mass scaling:*** to reduce computing times while preserving low kinetic energy without sacrificing a smooth indentation curve.

All these implementations led to an indentation curve that matches the expected shape of a theoretical indentation curve.

3.1.2 Verification

Preliminary simulations were performed to analyse the impact of certain factors in the model. This allowed to select the FEM model that most closely represents the phenomena without compromising computing times. These analyses were:

a) Indenter type
b) Friction coefficient (μ)
c) Mesh convergence
d) Round-off errors (double precision)

For simplicity, the preliminary analyses were carried out in an isotropic material. The simulation scheme for them is presented in Table 3.1

Table 3.1 Simulation scheme. FEM model verification

Material	Anisotropic indenter [1 1 1]		Anisotropic indenter [1 0 0]		Isotropic indenter		Mesh A	Mesh B	Mesh C	Isotropic double precision
	Simulation scheme									
AA6016mm1	μ=0	00Fr111	μ=0	00Fr100	μ=0	00Frlso	mA1	mB1	mC1	iP1
	μ=0.1	01Fr111	μ=0.1	01Fr100	μ=0.1	01Frlso				
	μ=0.2	02Fr111	μ=0.2	02Fr100	μ=0.2	02Frlso				
	μ=0.3	03Fr111	μ=0.3	03Fr100	μ=0.3	03Frlso				
AA5005	/		/		/		mA2	mB2	mC2	iP2

Indenter type

A revision of literature could not identify any works that consider the anisotropy of the indenter (diamond). As a matter of fact, a large part of the studies consulted neglected the elastic nature of the indenter and considered it a rigid component. As diamond is a strongly anisotropic cubic material, a preliminary study on the elastic behaviour of the indenter was carried out.

There was no information, either on the literature or by the provider of the indentation equipment, with respect to of the orientation of the crystal system of the diamond in the indenter with respect to the vertical axis. Therefore, the least and most rigid directions of this lattice were tested ([100] and [111]). Elastic constants for diamond were obtained from [63]. In addition, an isotropic elastic indenter was considered. These analyses were run for different friction coefficients (μ=0, 0.1, 0.2, 0.3). The selection of these friction coefficients had the purpose of analysing a wide range of μ, rather than using friction coefficients commonly found in this type of test. An example of the results is shown in Fig. 3.2.
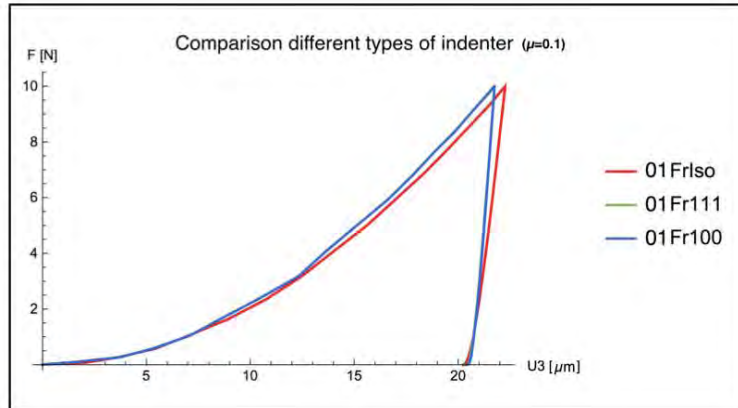
Figure 3.2 Comparison of indentation curves for different indenter types. AA6016mm1, μ=0.1

For all studied cases, computing time ranged from 5.1 hours (isotropic indenter) to 5.3 hours ([111]). It was observed that the details of the elastic behaviour of the indenter did not strongly influence the results. An isotropic elastic indenter was chosen due the following reasons:

a) Although an indenter with cubic symmetry would be a novelty in the field, there was no evidence as to the real indentation direction.
b) The model with an isotropic indenter had the shortest running time.

Friction coefficient

Four friction coefficients (μ=0, μ=0.1, μ=0.2, μ=0.3) were used to verify the degree of influence of this parameter in the results. As has been stated, the selection of these friction coefficients had the purpose of analysing a wide range of μ, rather than using friction coefficients commonly found in this type of test. Results for the isotropic indenter are presented in Fig. 3.3.
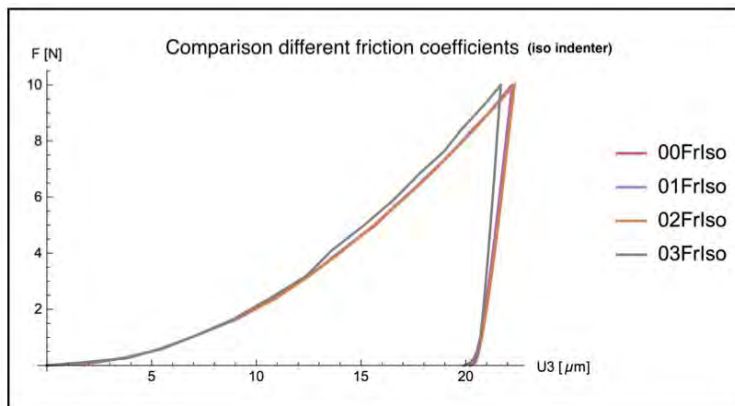

Figure 3.3 Comparison of indentation curves for different friction coefficients. AA6016mm1, iso indenter

As was observed from Figure 3.3, the variations due to changes in the friction coefficient were minimum, and similar behaviour was observed for all the indenters. A friction coefficient of μ=0.1 was used due to the fact of it being widely used in the literature [64, 65, 66], and the fact that friction is always present to some degree. The difference in computing times was negligible.

Mesh convergence

The purpose of this test was to evaluate the dependence of a result with the employed mesh. Three meshes that followed the conditions established in Section 3.1.1 were proposed for the base material:

a) Mesh A: 48x16x49 nodes
b) Mesh B: 42x14x41 nodes
c) Mesh C: 30x10x29 nodes

For this evaluation, not only the quality of the indentation curve was compared, but indentation depth as well (Fig. 3.4). According to the test, while mesh A and B provided the same results, mesh C did not. In addition, the obtained indentation curve with mesh C had a low quality (oscillations). Computing times were 7.2, 5.1, and 3.69 hours for the mesh A, B, and C respectively. Following this, it was reasonable to adopt mesh B.
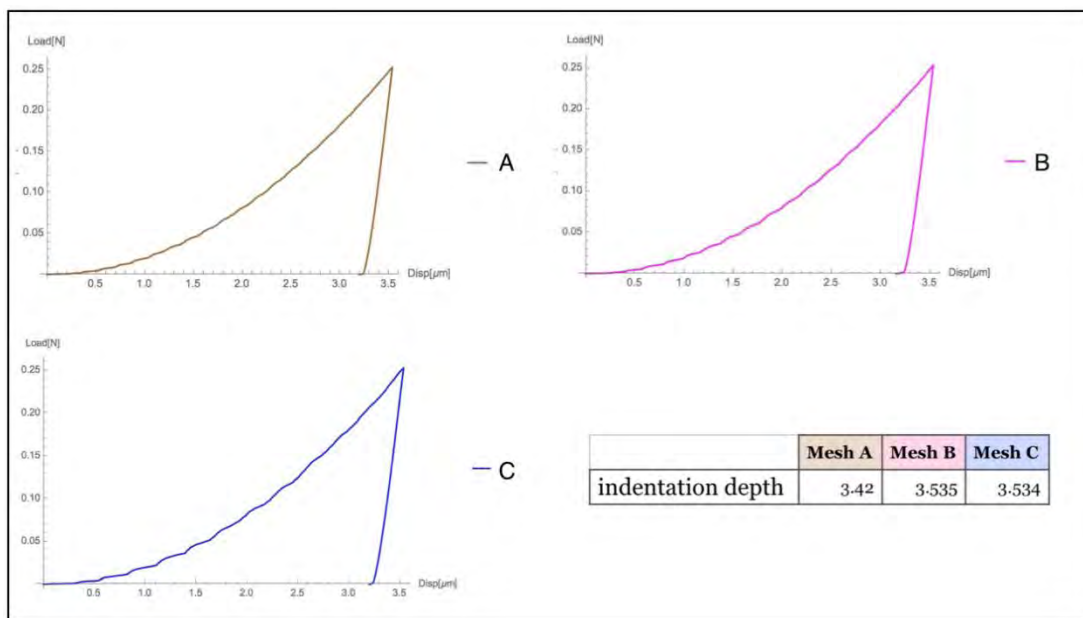

	Mesh A	Mesh B	Mesh C
indentation depth	3.42	3.535	3.534

Figure 3.4 Comparison of indentation curves and indentation depth for different meshes

Round-off errors

A double precision analysis was carried with the isotropic model to estimate the deviations from the experimental results due to round-off errors. This was done for both the AA6016mm1 and the AA5005 alloys (Fig. 3.5).
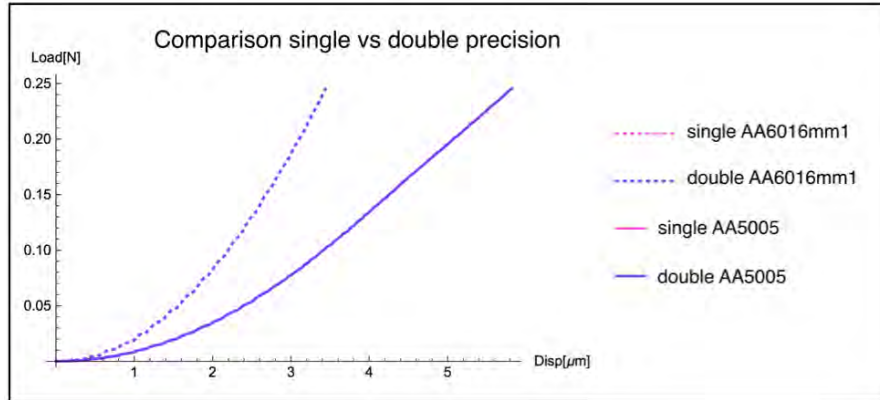
Figure 3.5 Comparison of indentation curves for single and double precision

Round-off errors represented a negligible percentage of deviation. Due to the significant increase in computing time and the small amount of improvement this method carries, single-precision was selected.

3.1.3 Final FEM model

Based on the original model, changes made to the model for this thesis included:

a) *Reduction in model size:* due to the changes in indentation size
b) *Changes in step duration:* to reflect the times presented by ASTM E384. Since no strain rate effects were included in the model, there were no effects in the results obtained. For this same reason, the creep step was eliminated.
c) Definition of sets to speed up data collection.

In consequence of the four preliminary analyses, and the conditions mentioned at the beginning of this chapter, the following model was adopted:

a) Indenter type: Isotropic
b) Interaction: μ=0.1 (between indenter and base material)
c) Load: 0.0625N applied as a pressure with smooth amplitude. Therefore, since the model geometry is a fourth of an indentation: 4*0.0625=0.25N (Fig. 3.1)
d) Boundary conditions: Symmetry on X and Y. **0** displacement at the base of the indented material
e) Base material mesh: 42x14x41 nodes
f) Element type: C3D8R
g) Steps: 2
    a. Load: 10s
    b. Unload: 10s
h) Precision: single

3.2 HMS simulations

3.2.1 Implementation

Distinctions between running an isotropic simulation in Abaqus® and an anisotropic one in HMS included performing the following extra steps (a full description of the procedure to prepare HMS simulations can be found in [31]):

a) Material orientations for the base material were defined in Abaqus® to exchange between ND, RD, and TD material directions.

b) User defined material containing both elastic and plastic parameters, as well as solution dependent variables.

c) A SMT file containing a discrete ODF was needed. This file was obtained using the information obtained from X-Ray diffraction.

d) Calculation of yield locus using an appropriate micro mechanical model and the Facet function. ALAMEL crystalline approximation was used, since it has been reported it yields better results than FC Taylor [67, 68]

As has been mentioned in Section 1.4, HMS has the capability to predict changes in texture due to plastic deformation, update it, and with the new texture recalculate the yield locus. This process was run for all materials only in the RD direction. The purpose was to see if there was a visible difference between running the simulations with constant texture (constant anisotropy) and texture evolution (evolving anisotropy). Some of the results obtained are presented in Fig. 3.6 and Fig. 3.7 (AA6016mm1RD, AA5005RD).
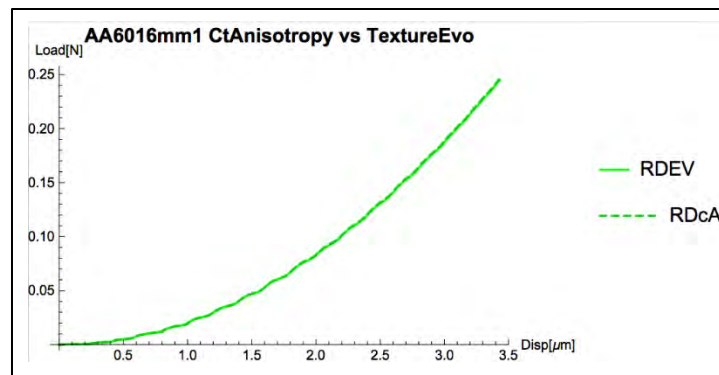

Figure 3.6 Comparison between constant anisotropy (RDcA) and texture evolution simulations for the AA6016mm1RD (RDEV)
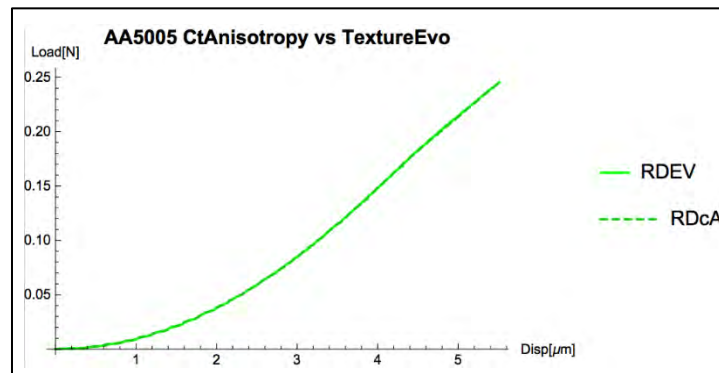

Figure 3.7 Comparison between constant anisotropy (RDcA) and texture evolution simulations for the AA5005RD (RDEV)

From Fig. 3.6 and Fig 3.7, as well as an inspection of the other materials results, it was seen that there is no visible difference between the constant anisotropy and texture evolution simulations. Since the latter takes over 3 times the time to run in comparison to the former, it was decided to perform all the analysis with the assumption of constant anisotropy. The followed simulation scheme is presented in Table 3.2. Isotropic simulations were executed in Abaqus® only.

Table 3.2 HMS and Abaqus® simulation scheme

Simulation scheme			
Material	isotropic	Material direction	constant anisotropy
6016mm1	iS1	ND	cA1
		RD	cA2
		TD	cA3
5005	iS2	ND	cA4
		RD	cA5
		TD	cA6
1100	iS3	ND	cA7
		RD	cA8
		TD	cA9
3103	iS4	ND	cA10
		RD	cA11
		TD	cA12
6016mm2	iS5	ND	cA13
		RD	cA14
		TD	cA15

3.2.2 Data extraction

For the simulations, displacements and coordinates at the nodes of the base material (contact surface) were obtained. These, in conjunction with the smooth loading function were used to construct the indentation curves and the morphology of the predicted indentation. Data extraction was performed using a python script to obtain RPT files of these values for further processing with Mathematica®.

A geometric parameter of interest for this model was m_x-m_y (Fig. 3.8), which is related to the deviation respect a perfectly squared indentation. When this parameter equals zero, the indentation is perfectly square.
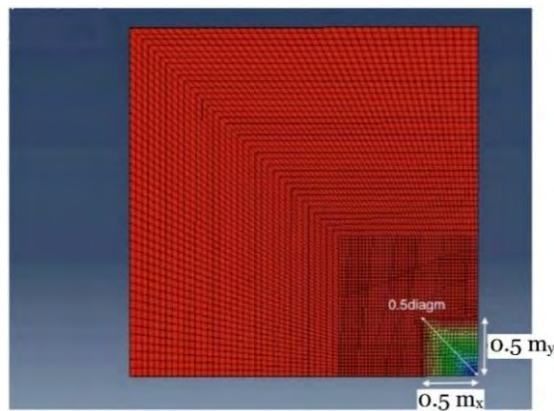

Figure 3.8 m_x and m_y of an indentation

46

Chapter 4. Results

Results obtained according to the procedures described in chapters 3 and 4 are presented in this chapter, grouped by type of result, rather than by material.

4.1 Indentation curves

4.1.1 Experimental indentation curves

Reduced experimental indentation curves and their corresponding fit (black) are presented in Fig. 4.1 through Fig. 4.5. These figures include indentation depth, with and without elastic recovery, and coefficient of variation.
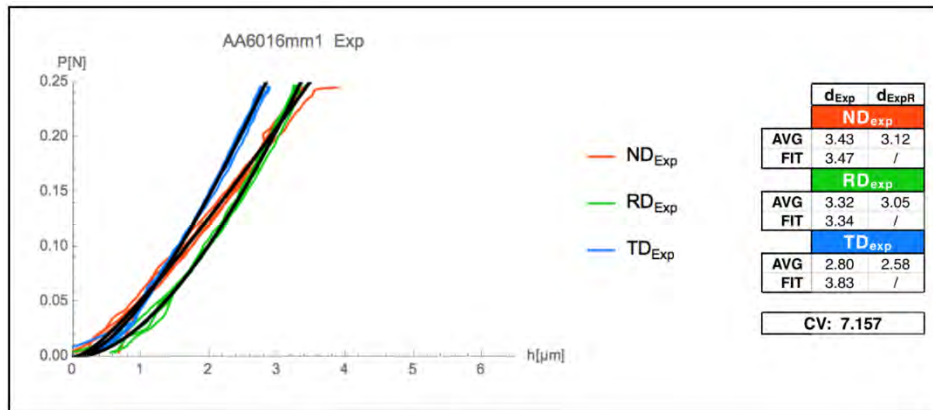

Figure 4.1 Experimental indentation curves and their fit (black). AA6016mm1
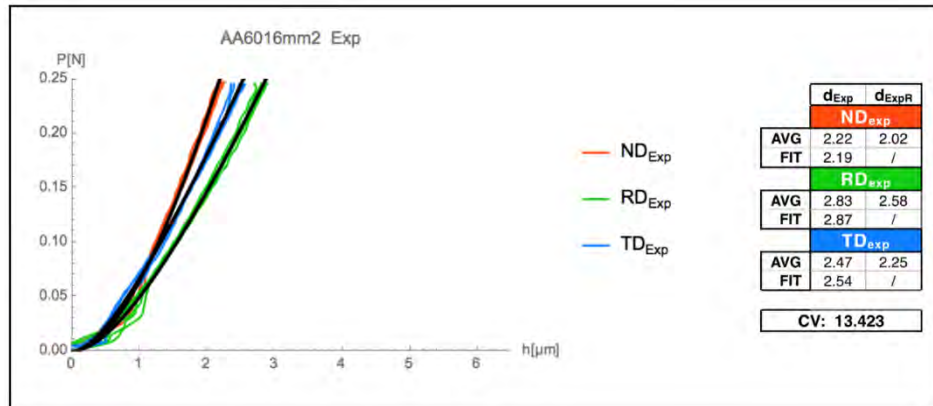
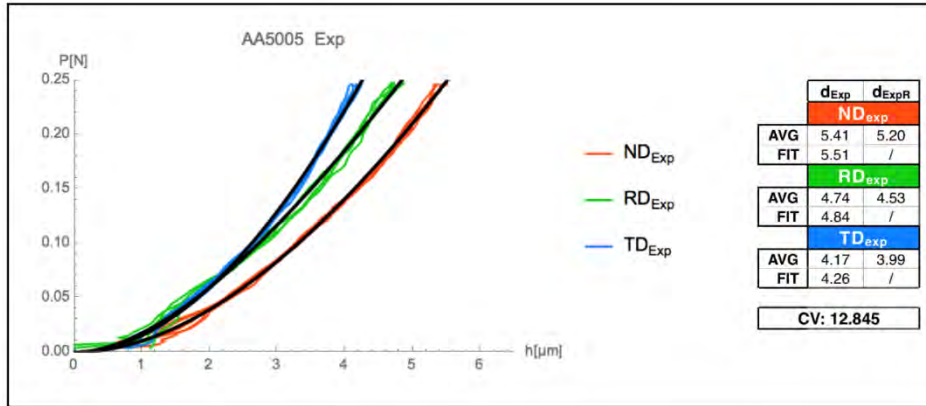Figure 4.2 Experimental indentation curves and their fit (black). AA6016mm2

Figure 4.3 Experimental indentation curves and their fit (black). AA5005
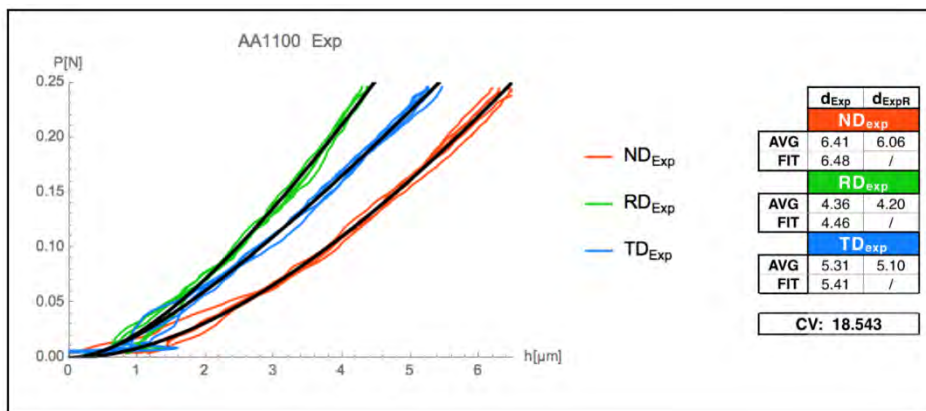

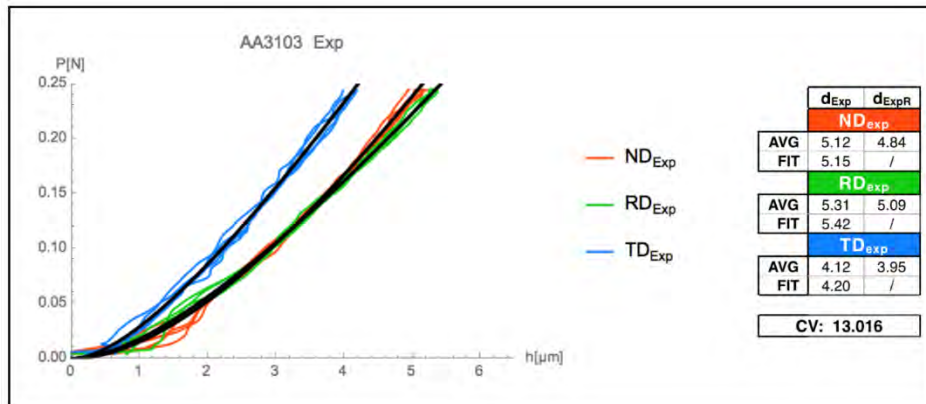Figure 4.4 Experimental indentation curves and their fit (black). AA1100

Figure 4.5 Experimental indentation curves and their fit (black). AA3103

For the AA6016mm1ND sample, problems arose at the time of measurement, since the sample was mounted differently from the others. This caused interference between the indenter and optical profilometer positions. The problem was only present in this sample. For further analysis the information from this direction was considered unreliable (results presented later in this section reinforce this conclusion), and as such, parameters obtained with this data were considered erroneous and not included in the analysis.

Two observations can be made from the previous figures. First, while the fitting curve provided an adequate approximation to the shape of the experimental curves, for some alloys, it deviated at the very end. In consequence, it overestimated the indentation depth. Second, there was a visible difference, in terms of indentation depth, between material directions for any given material. Whether this difference was statistically significant is presented in Table 4.1.

Table 4.1 Significant depth difference between directions for each material

Statistical analysis			
Significant difference between directions for each material (depth)			
Ho: *There is no relationship between the variation in depth for each direction and said direction. The variation is due to random effects*			
Material	Result	p-value	Consequence
AA6016mm1	Null hypothesis rejected	1.275E-16	Anisotropic material
AA6016mm2	Null hypothesis rejected	3.141E-15	Anisotropic material
AA5005	Null hypothesis rejected	5.144E-15	Anisotropic material
AA1100	Null hypothesis rejected	1.029E-12	Anisotropic material
AA3103	Null hypothesis rejected	6.114E-15	Anisotropic material

All tested materials had a significant difference in indentation depth between directions. Consequently, for indentation purposes, they were considered anisotropic.

4.1.2 HMS indentation curves

Indentation curves obtained with HMS are presented in Fig. 4.6 through Fig. 4.10. These figures include indentation depth and coefficient of variation.
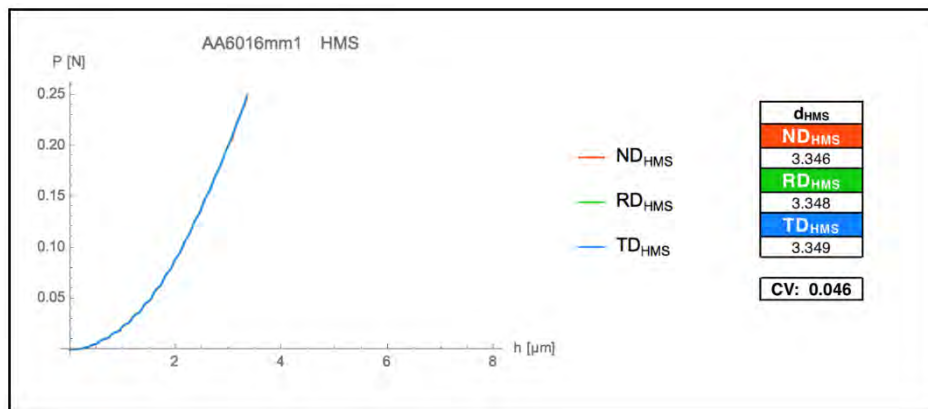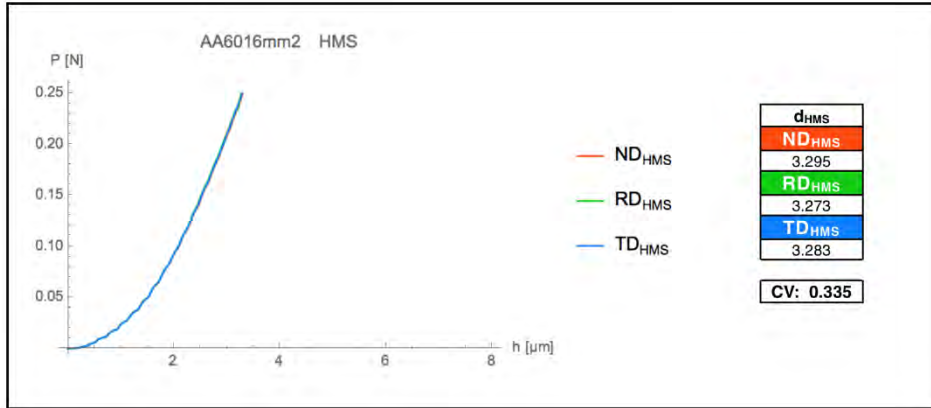

Figure 4.6 FEM results. AA6016mm1

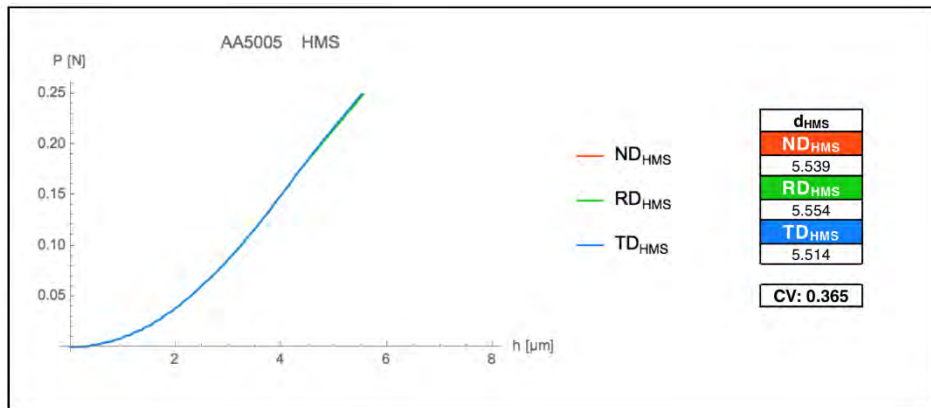Figure 4.7 FEM results. AA6016mm2
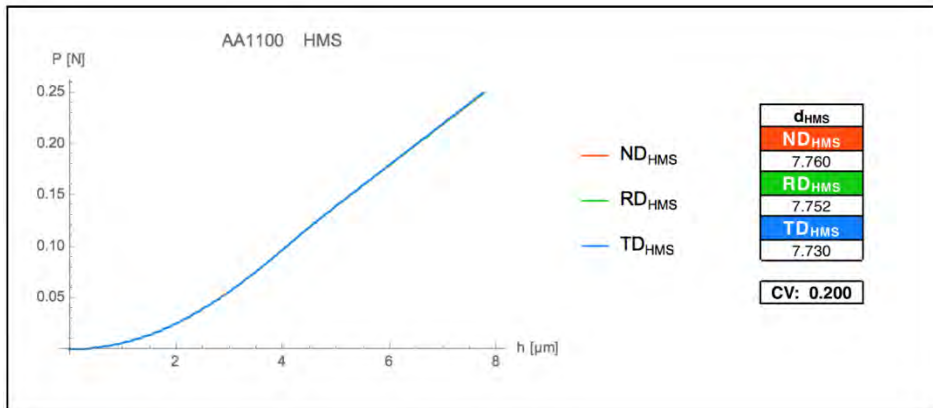

Figure 4.8 FEM results. AA5005
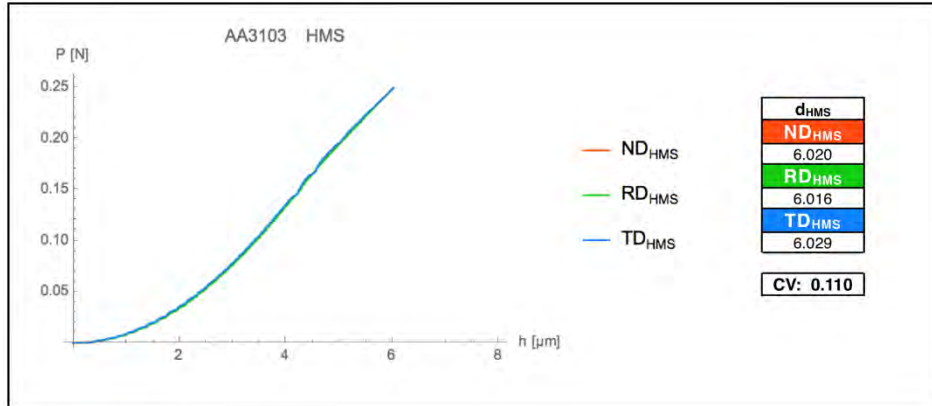

Figure 4.9 FEM results. AA1100

Figure 4.10 FEM results. AA3103

The indentation depth difference between directions for the same material was negligible. In consequence, the coefficient of variation of each material is far smaller than its experimental counterpart. Additionally, HMS consistently predicted larger indentation depths. It should be noted as well that the indentation curve for the last three materials (AA5005, AA1100, AA3103) deviates from the shape expected from Eq. 1.44.

4.1.3 Comparison between experimental and HMS results

Qualitative comparison between experimental and HMS predicted indentation curves is presented in Fig. 4.11 through Fig. 4.15. For the former, only the fitting curve is shown.
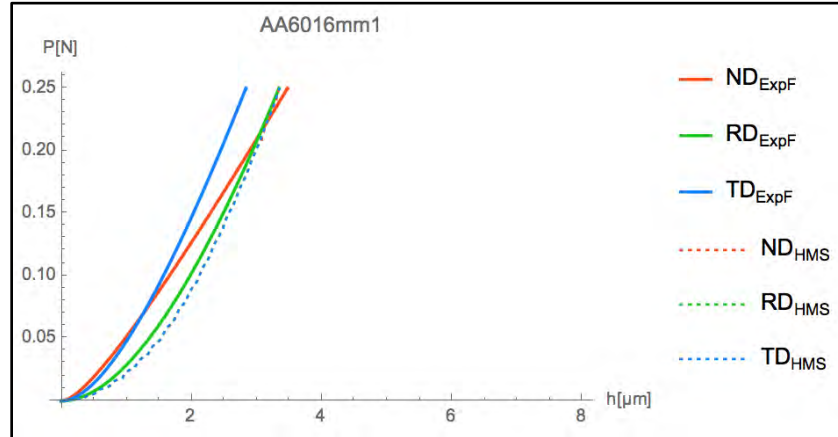

Figure 4.11 Comparison between HMS and experimental indentation curves. AA6016mm1
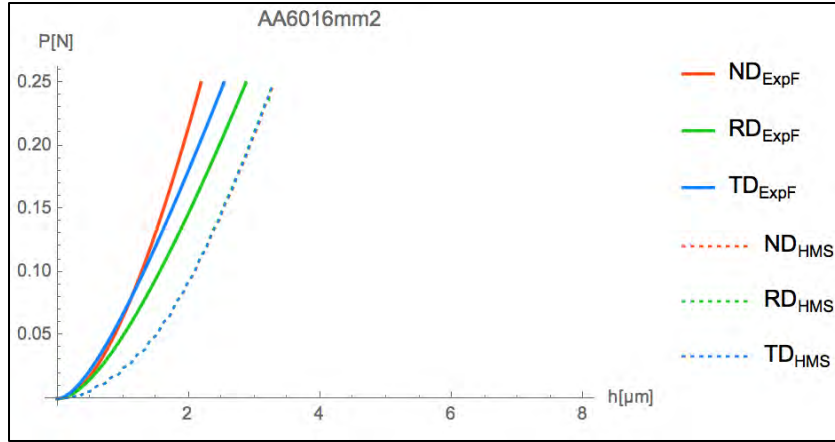
Figure 4.12 Comparison between HMS and experimental indentation curves. AA6016mm2
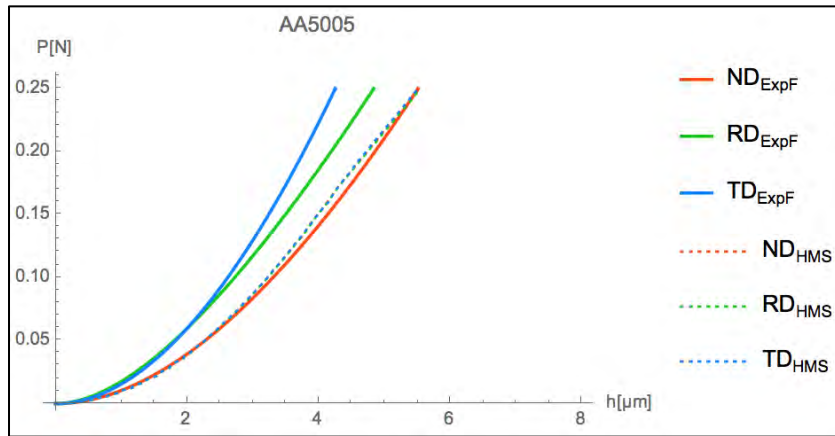

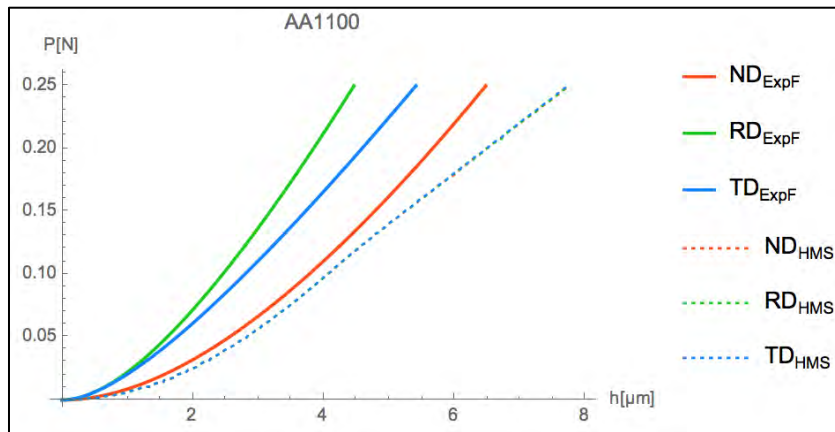Figure 4.13 Comparison between HMS and experimental indentation curves. AA5005

Figure 4.14 Comparison between HMS and experimental indentation curves. AA1100
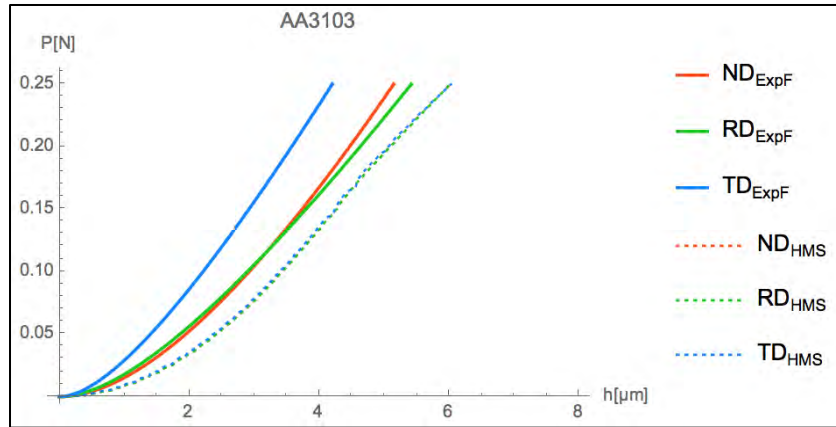
Figure 4.15 Comparison between HMS and experimental indentation curves. AA3103

The deviation of HMS predictions from experimental results was in terms of magnitude of anisotropy and indentation depth. For the first one, HMS underestimated the amount of anisotropy for all materials by an order of magnitude or more. Regarding indentation depth, HMS overestimated the indentation depth.

The magnitude of the deviation of HMS predictions from experimental results varied from alloy to alloy (Table 4.2). However, for almost all cases, since HMS predicted a softer, less anisotropic material, the difference is large. Whether this difference is statistically significant or not is summarised in Table 4.3.

Table 4.2 Deviation between experimental results and HMS predictions (depth)

% deviation of HMS predictions from experimental results			
ND	RD	TD	Mean
%dev	%dev	%dev	%dev
AA6016mm1			
3.65	0.17	18.18	7.33
AA6016mm2			
50.71	14.10	29.51	31.44
AA5005			
0.51	14.79	29.60	14.97
AA1100			
19.78	73.65	42.87	45.43
AA3103			
16.95	11.02	43.49	23.82

Table 4.3 Significant difference between HMS prediction and experimental data (depth).

Statistical analysis		
Significant difference between HMS prediction and experimental results (depth)		
Ho: *There is no significant difference between the HMS depth prediction and the experimental data.*		
Material	Result	p-value (ND, RD, TD)
AA6016mm1	ND: Ho accepted, RD: Ho rejected, TD: Ho accepted	0.36, 0.391, 0.462E-5
AA6016mm2	ND: Ho rejected, RD: Ho rejected, TD: Ho rejected	9.358E-8, 1.197E-4, 2.532E-5
AA5005	ND: Ho rejected, RD: Ho rejected, TD: Ho rejected	0.014, 1.725E-5, 1.170E-6
AA1100	ND: Ho rejected, RD: Ho rejected, TD: Ho rejected	5.953E-5, 3.951E-9, 5.389E-7
AA3103	ND: Ho rejected, RD: Ho rejected, TD: Ho rejected	1.218E-4, 1.924E-6, 7.633E-7

4.2 HV

4.2.1 Comparison between experimental and HMS results

Experimental and predicted HV are presented in Table 4.4 along their corresponding diagonals. HMS kept the trend of predicting softer materials and less anisotropy. The difference between HV_{Exp} and HV_{HMS} was significant, as shown in Table 4.5

Table 4.4 Experimental and predicted HV

	Indentation diagonals [μm] and HV			
	Exp		HMS	
	AVG m_{Exp}	AVG HV_{Exp}	m_{HMS}	HV_{HMS}
AA6016mm1				
ND	22.57	91	22.615	91
RD	23.77	82	22.572	91
TD	21.97	96	22.572	91
AA6016mm2				
ND	19.41	123	21.895	97
RD	21.42	101	21.938	96
TD	20.07	115	21.931	96
AA5005				
ND	37.48	33	37.060	34
RD	32.84	43	27.067	34
TD	26.22	68	37.053	34
AA1100				
ND	38.67	31	51.726	17
RD	32.09	45	51.775	17
TD	34.92	38	51.789	17
AA3103				
ND	31.74	46	41.409	27
RD	30.45	50	41.437	27
TD	29.03	55	41.515	27

Table 4.5 Significant difference between HMS prediction and experimental data (HV)

Statistical analysis		
Significant difference between HMS prediction and experimental results (HV)		
Ho: *There is no significant difference between the HMS HV prediction and the experimental data.*		
Material	Result	p-value (ND, RD, TD)
AA6016mm1	**ND**: Ho accepted, **RD**: Ho rejected, **TD**: Ho rejected	0.177, 3.927E-6, 4.734E-5
AA6016mm2	**ND**: Ho rejected, **RD**: Ho rejected, **TD**: Ho rejected	3.684E-7, 1.3E-5, 1.037E-6
AA5005	**ND**: Ho rejected, **RD**: Ho rejected, **TD**: Ho rejected	0.016, 1.262E-5, 1.69E-8
AA1100	**ND**: Ho rejected, **RD**: Ho rejected, **TD**: Ho rejected	6.300E-7, 3.318E-8, 3.080E-7
AA3103	**ND**: Ho rejected, **RD**: Ho rejected, **TD**: Ho rejected	4.595E-7, 3.659E-7, 1.517E-8

4.3 Indentation shape

4.3.1 Experimental indentation shape

As stated in Section 2.2.2, d_{Expl} was obtained from the optical measurement of the indentation diagonals. As seen from Table 4.6 and Figs. 4.1 - Fig. 4.5, d_{Expl} does not match d_{Exp}, which suggests a deviation of the current indentation shape to the ideal shape.

Table 4.6 Inferred indentation depth from diagonals

AVG d_{Expi} [μm]		
ND	RD	TD
AA6016mm1		
3.23	3.40	3.14
AA6016mm2		
2.78	3.31	2.87
AA5005		
5.38	4.64	3.74
AA1100		
5.49	4.60	4.98
AA3103		
4.58	4.37	4.37

AFM measurements were taken in all directions for the AA6016mm1 and AA6016mm2 (Fig. 4.16 and Fig. 4.17). They are presented along their profiles (Section 2.2.3).
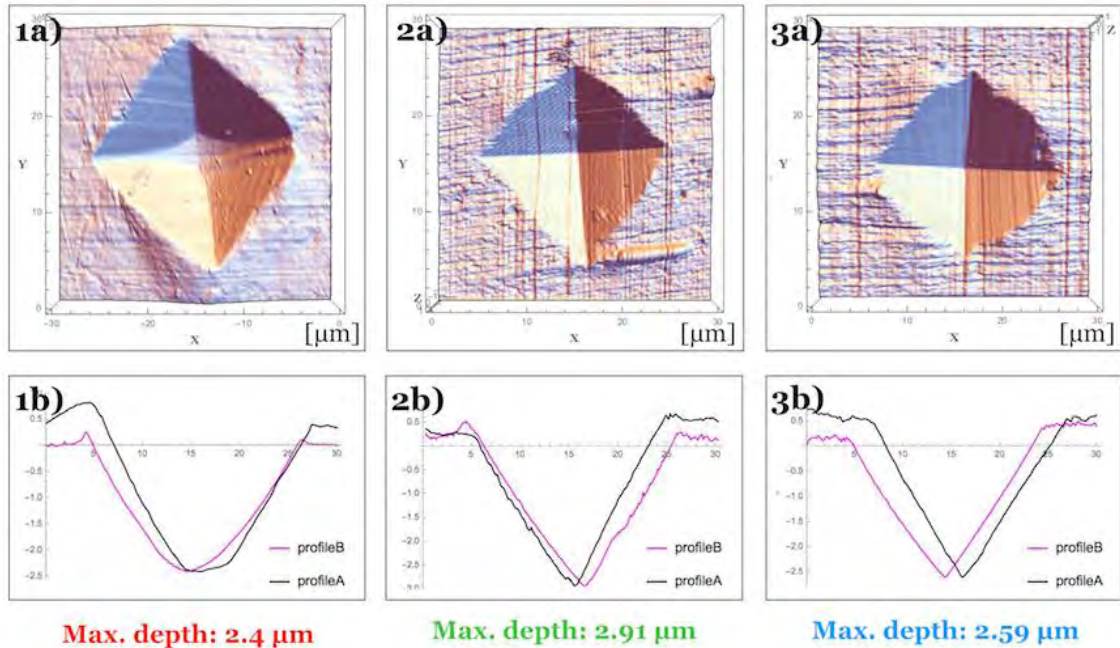
Max. depth: 2.4 μm   **Max. depth: 2.91 μm**   **Max. depth: 2.59 μm**

Figure 4.16 Indentation shape for AA6016mm1. Numbers 1, 2, 3, indicate ND, RD, TD respectively.
a) AFM. Plan view. b) Indentation profile.

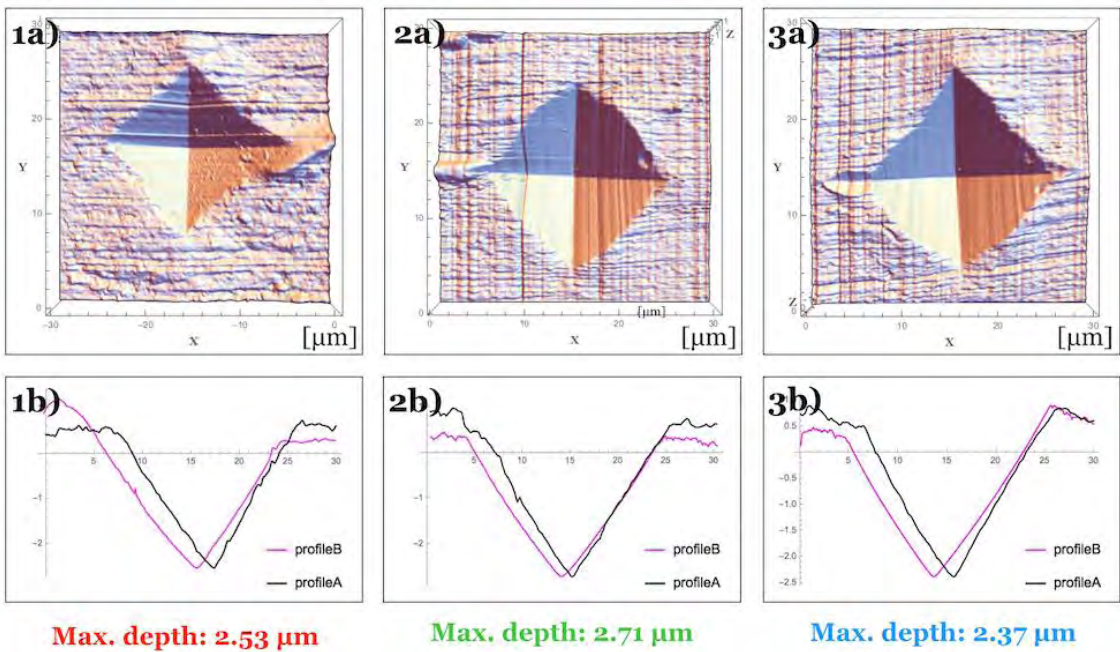**Max. depth: 2.53 μm**   **Max. depth: 2.71 μm**   **Max. depth: 2.37 μm**

Figure 4.17 Indentation shape for AA6016mm2. Numbers 1, 2, 3, indicate ND, RD, TD respectively.
a) AFM. Plan view. b) Indentation profile.

A distorted indentation shape was obtained for AA6016mm1ND, which was consistent with the measuring problems described before. Almost all directions presented a slightly asymmetric profile, and an even more asymmetric pile-up. The maximum depth obtained from these profiles was compared with d_{ExpR} (Fig. 4.1 - Fig. 4.5) and d_{ExpI} (Table 4.6).

It was found that the AFM reported depth matched closely with the first one, but not with the second one. This served as a validation of the methods of obtaining d_{Exp} and d_{ExpR}. Additionally, it enforced the idea that the indentations of all materials do not necessarily follow the ideal profile described in Fig. 1.16.

4.3.2 HMS indentation shape

The m_x-m_y parameter was employed as a measure of the amount of squareness of an HMS predicted indentation. From Table 4.7, not only the isotropic simulation was not perfectly square, sometimes it was even less square than its anisotropic counterparts.

Table 4.7 Indentation squareness of HMS predictions, when m_x-m_y =0, the indentation is perfectly square.

HMS m_x -m_y [μm]			
ND	RD	TD	iso
AA6016mm1			
-0.360	-0.360	-0.360	-0.360
AA6016mm2			
0.500	0.520	0.530	-0.760
AA5005			
0.330	0.240	0.340	0.250
AA1100			
0.430	0.240	0.360	0.230
AA3103			
0.360	0.240	0.430	0.170

Contour plots for the plan view of the indentations with elastic recovery were obtained from the simulations (Fig. 4.18 - Fig. 4.20). For a single alloy, contour levels are the same to ease comparison between material directions. AA6016mm1 and AA6016mm2 are presented in Section 4.3.3.
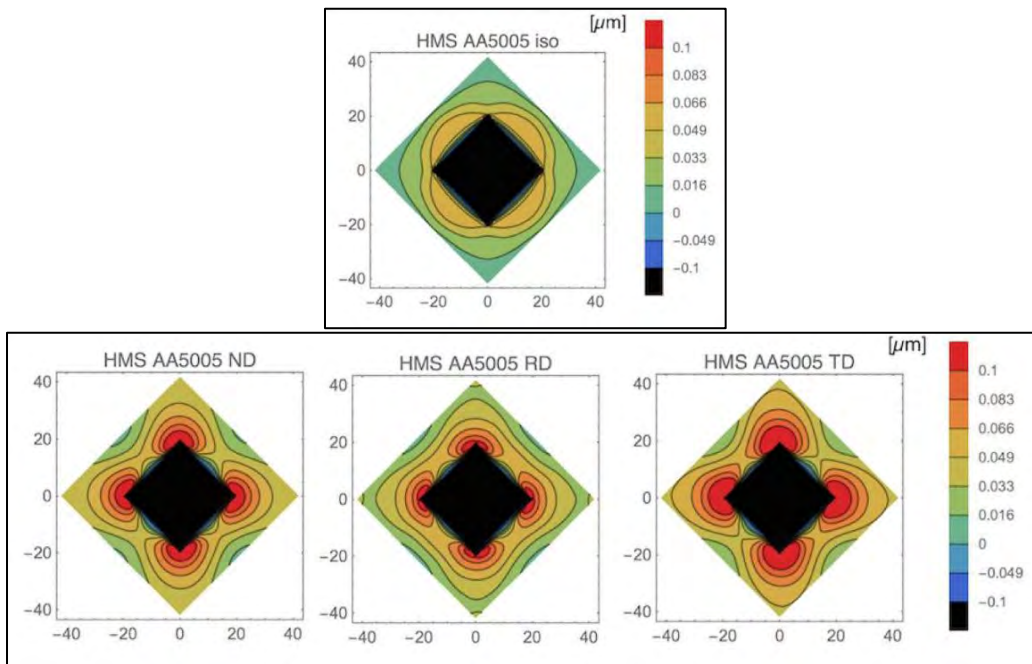

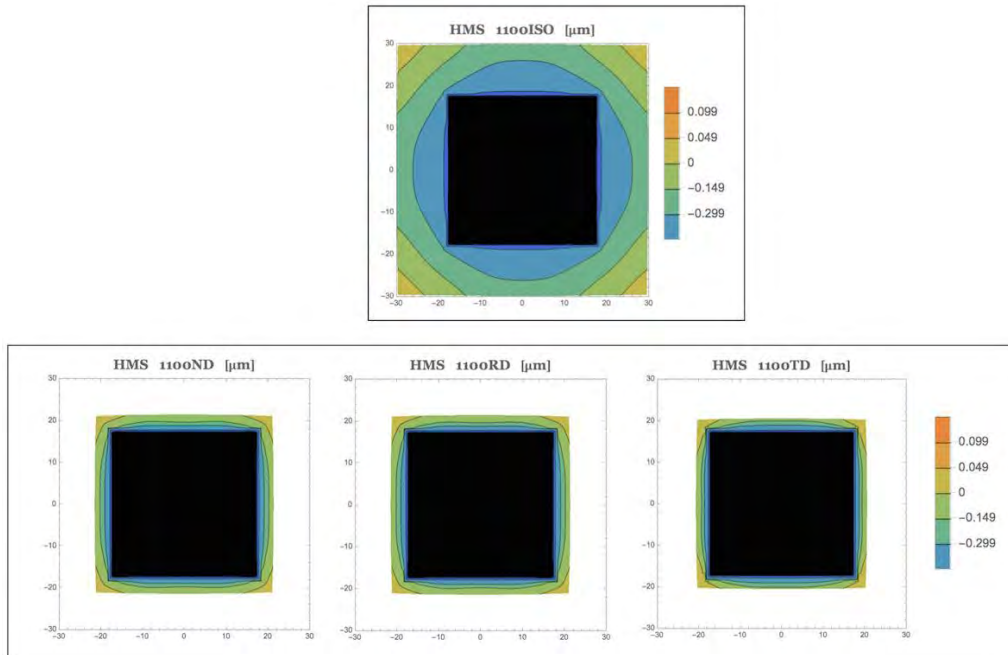Fig. 4.18 HMS contour plots. Plan view. AA5005

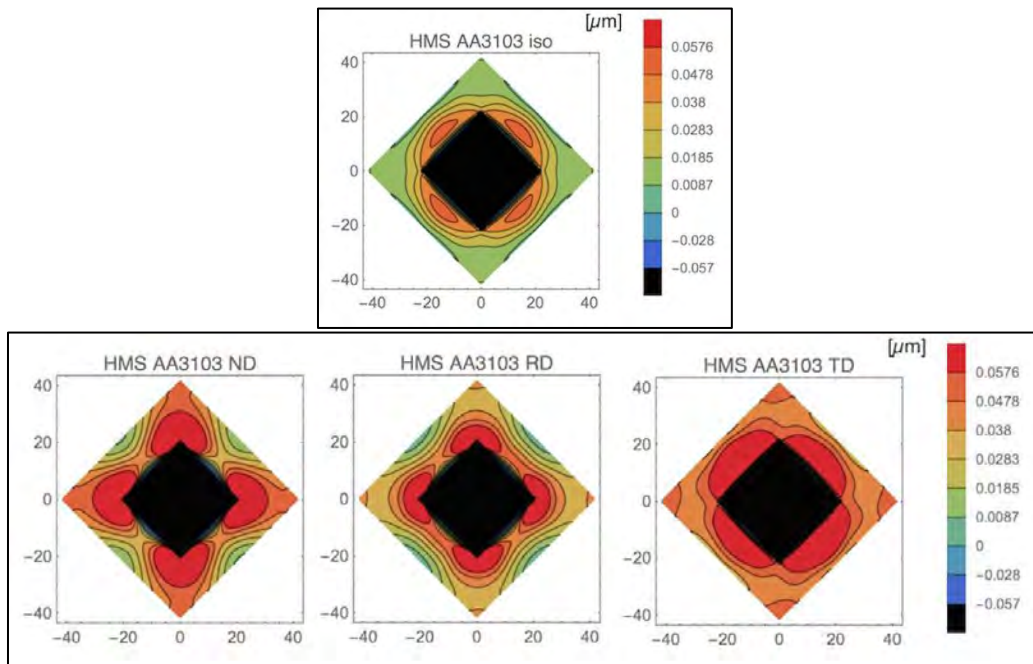Fig. 4.19 HMS contour plots. Plan view. AA1100

Fig. 4.20 HMS contour plots. Plan view. AA3103

Differences for position and magnitude of pile up between each material direction were predicted. These were compared to the isotropic case, where for all alloys, the magnitude of the pile up was smaller. In addition, for some alloys, pile up displaced from the sides to the corners, a position that is not commonly found.

4.3.3 Comparison between experimental and HMS results

Contour plots with AFM and HMS, were compared for the AA6016 alloy in Fig. 4.21 through Fig. 4.26
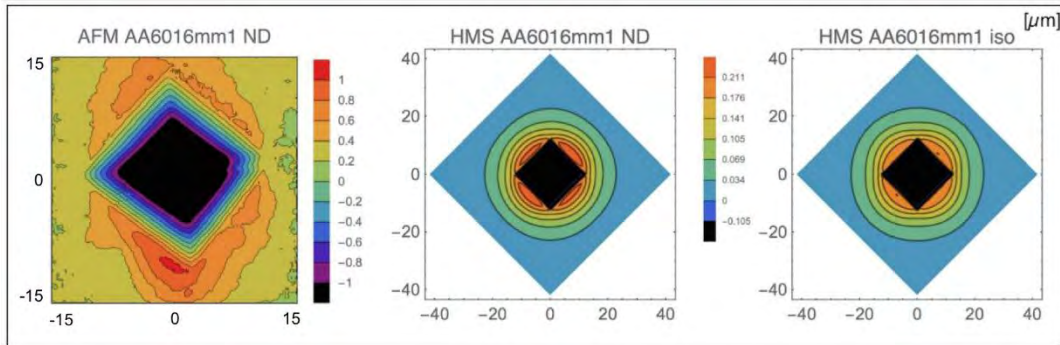

Figure 4.21 Contour plots for AFM and HMS indentations. Plan view. AA6016mm1ND
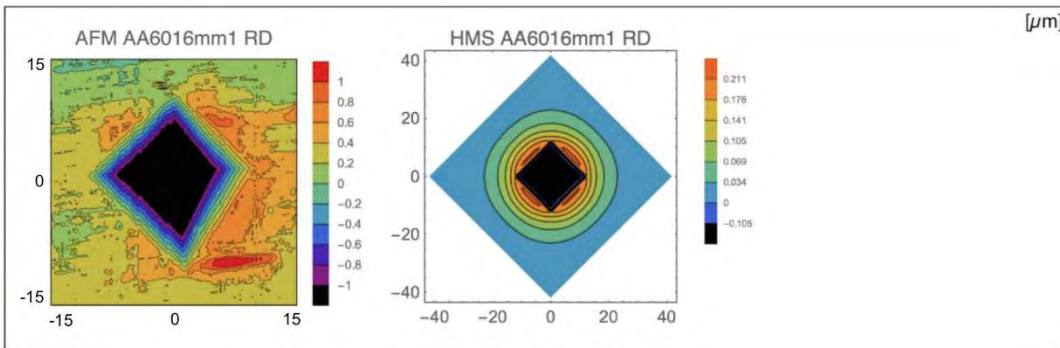

Figure 4.22 Contour plots for AFM and HMS indentations. Plan view. AA6016mm1RD

Figure 4.23 Contour plots for AFM and HMS indentations. Plan view. AA6016mm1TD

Figure 4.24 Contour plots for AFM and HMS indentations. Plan view. AA6016mm2ND

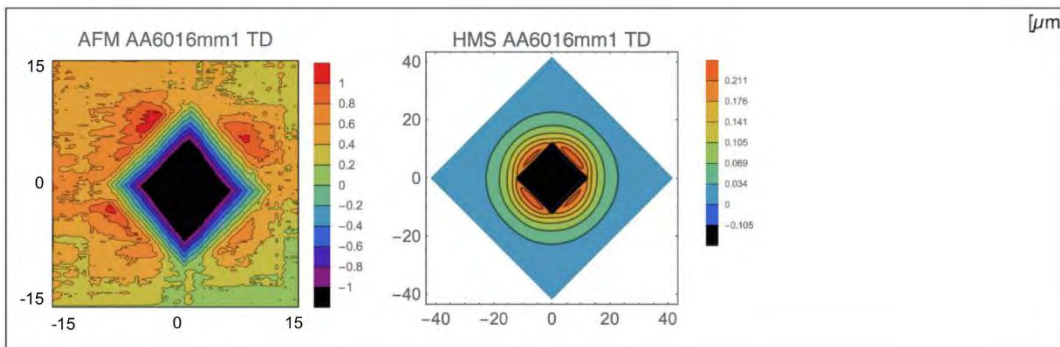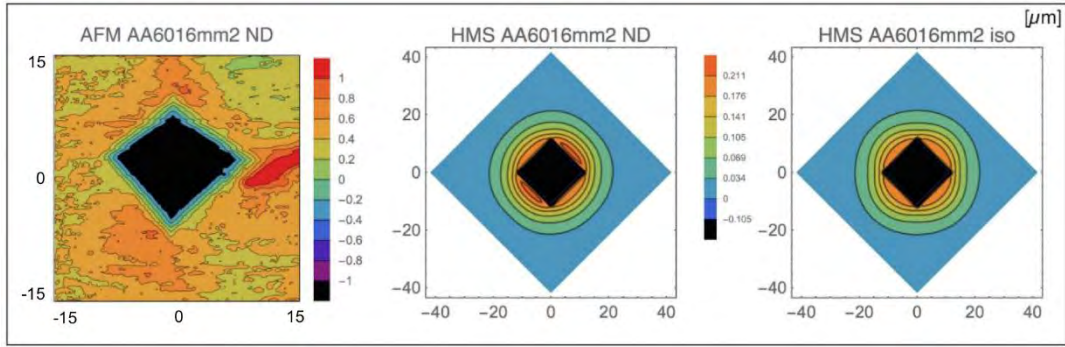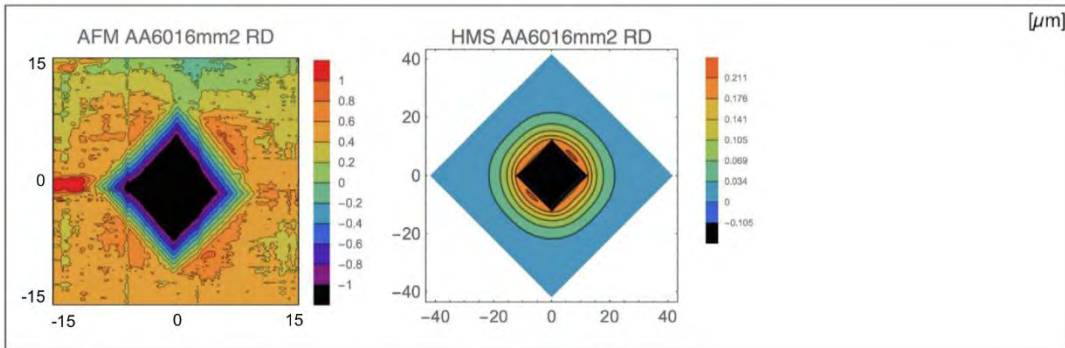Figure 4.25 Contour plots for AFM and HMS indentations. Plan view. AA6016mm2RD

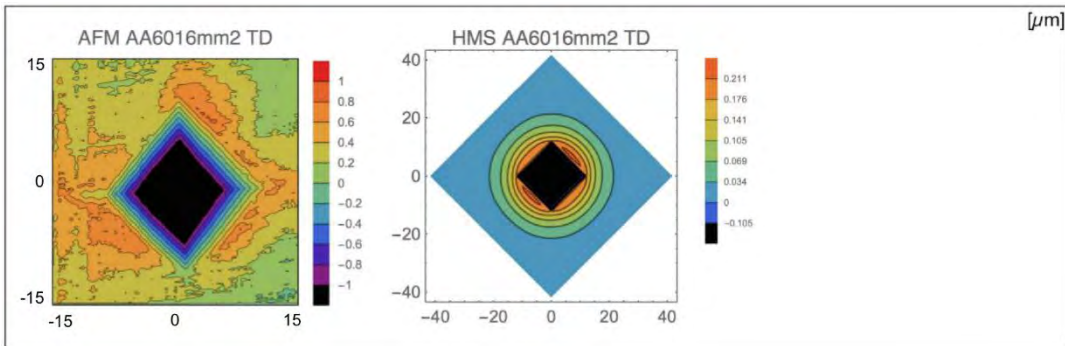

Figure 4.36 Contour plots for AFM and HMS indentations. Plan view. AA6016mm2TD

It was found that the pile up present in the experimental results was always larger than its predicted counterpart. Additionally, in most cases it did not possessed the symmetry found in the simulations. Despite these differences, for most directions, HMS provided an adequate approximation of the pile up position.

Chapter 5. Discussion

The discussion is divided into three sections:
  a) Experimental results
  b) HMS results
  c) Comparison between experimental and HMS results

Experimental results

The adjustment method proposed for the plastic part of the experimental curves yielded an excellent fit in terms of shape, and good in terms of indention depth, with differences between d_{ExpF} and mean of experimental data being less than 5%. It is seen in multiple cases that the fit overestimated indentation depth. Although this may be corrected by using a weighted least squares method for the fitting, it should be reminded that despite Eq. 1.44 being justified by a dimensional analysis, it is an empirical expression that is only valid for certain material behaviour. Therefore, the observed deviation may have its origins in a variation of the response of the material to the applied load. As for d_{ExpR}, the linear fitting and extrapolating method yielded approximate results, which are confirmed by the ones by AFM.

Once the effectiveness of the fitting method was verified, it was found that the indentation curves visibly varied between directions. The statistical analysis confirms that all the materials are anisotropic with respect to indentation measurements. In spite of this, it is of interest to discard other possible sources of deviation between directions to ensure that the observed anisotropy was not a consequence of experimental errors. The two possible sources of deviations considered are:
  a) **_Sample preparation:_** Since all directions for a single material were resin mounted and prepared at the same time, it is assumed that the amount of sample modification due to strain hardening (during grinding) would be the same for all directions. Hence, it is discarded as a source of the observed anisotropy.
  b) **_Problems with the fitting method:_** This implies that an artefact taking place during fitting, like incorrect indenter-material contact determination, is the responsible for the observed anisotropy. However, as has been mentioned, AFM measurements provided verification for these methods.

In terms of indentation shape, it was found that d_{ExpI} did not match d_{ExpR}, which leads to believe that the obtained indentation does not follow the ideal indentation profile. AFM measurements verified this as well, showing the presence of a pile up and slightly asymmetric indentations. As a consequence, it was decided to use indentation depth instead of HV for further analysis, to avoid additional errors due to the transformation from depth to hardness.

HMS results

Although the FEM model was optimised to reduce errors induced by meshing and time increments, some limitations were still found. It was observed that the imposed asymmetry on the mesh did have an impact on the results. It constantly predicted a non-square indentation for an isotropic material. Even more so, in some cases, the anisotropic material had a squarer indentation. This effect can hypothetically affect the simulated material anisotropy.

Another limitation found was in terms of the predicted indentation curves, since some of them presented an almost linear behaviour at the end, which is clearly a deviation from the expected shape. Several causes were investigated, and it was found that the model was too small, causing the plastic zone to reach the boundaries of the model (Fig. 5.1). Due to space constrains, only two materials are shown. However, AA6016mm2 had a behaviour like the one in Fig. 5.1a, while AA5005 and AA3103 had a similar behaviour to the one presented in Fig. 5.1b.
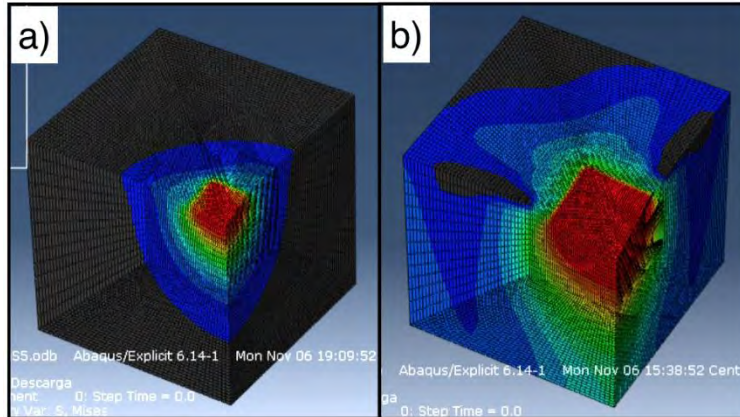

Figure 5.1 a) No plastic zone breakthrough effect. AA6016mm1 b) Plastic zone breakthrough AA1100.

Since the analysis uses homogeneous plastic theory (no dislocations, no grain boundaries), there is no need to repeat the simulations with a larger model, and the effect was corrected with the following method:

a) *Identification of the moment where the plastic zone breaks through to the boundaries:* This was done by linearizing the indentation curve ($\sqrt{P} = h$) (ND_U, RD_U, TD_U). For this new data, an interval, in which no plastic zone breakthrough had taken place, was defined. Afterwards, this interval was fitted to a straight line and extrapolated to P = 0.25N (ND_C, RD_C, TD_C) (Fig. 5.2), and compared with the original linearized data.
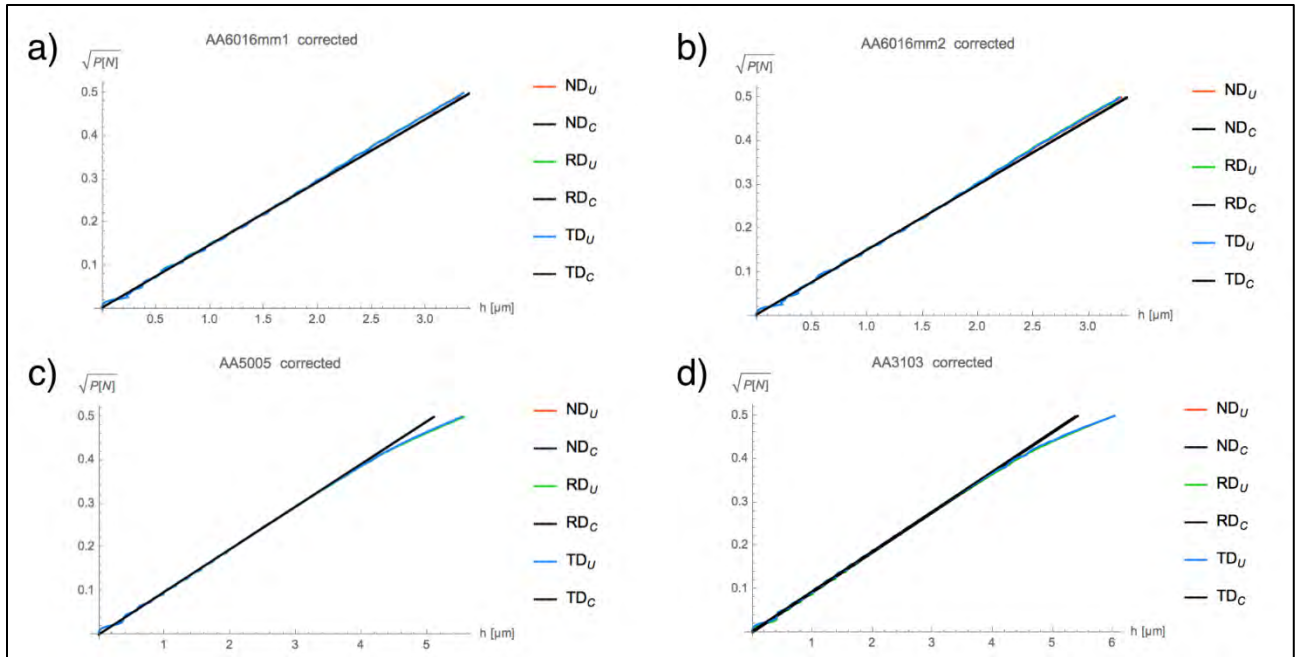
Figure 5.2 Start of the plastic zone breakthrough effect. a) AA6016mm1. b) AA6016mm2. c) AA5005. d) AA3103
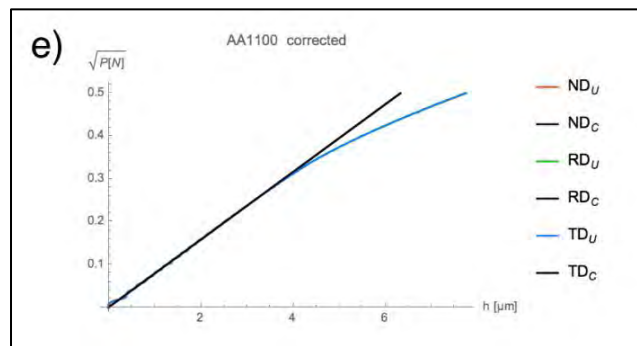
Figure 5.2 Start of the plastic zone breakthrough effect. e) AA1100

b) *Obtaining corrected indentation curves:* ND_c, RD_c, TD_c were converted into $P = h^2$, and corrected HMS indentation curves were obtained (Fig. 5.3 through Fig. 5.7). The difference is significant, with the largest deviation corresponding to the material with the overall largest indentation depths, since plastic zone breakthrough took place first.
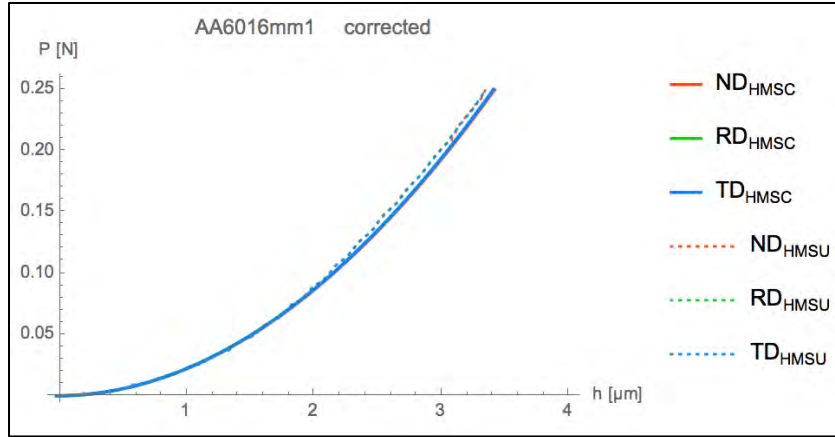
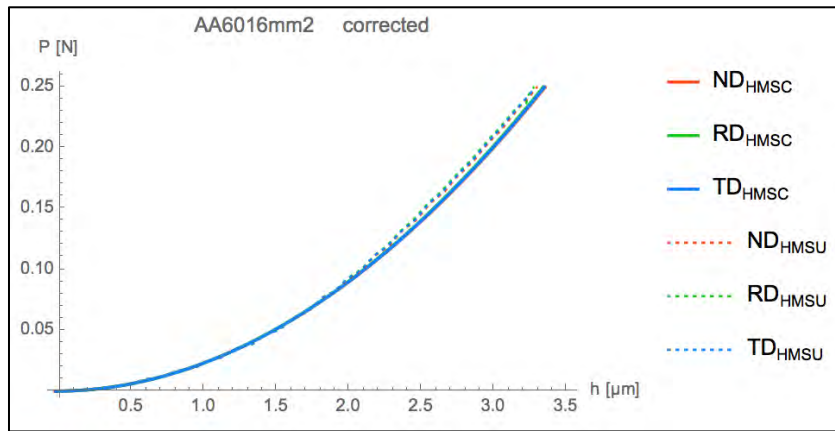Figure 5.3 Corrected HMS indentation curves. AA6016mm1. U: uncorrected. C: corrected

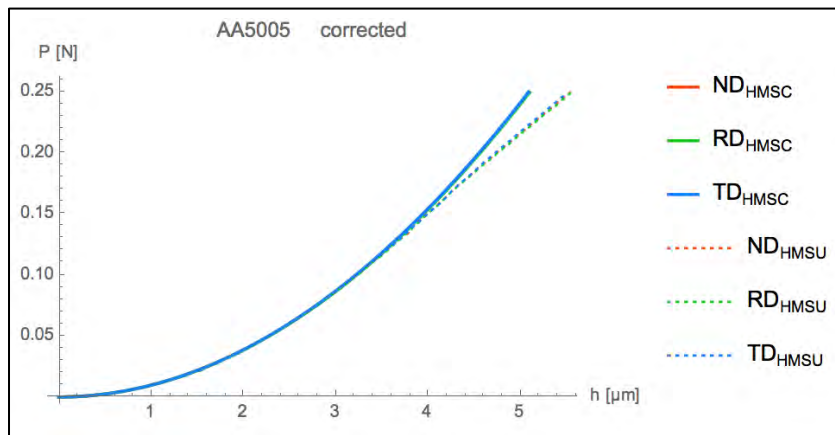Figure 5.4 Corrected HMS indentation curves. AA6016mm2. U: uncorrected. C: corrected

Figure 5.5 Corrected HMS indentation curves. AA5005. U: uncorrected. C: corrected
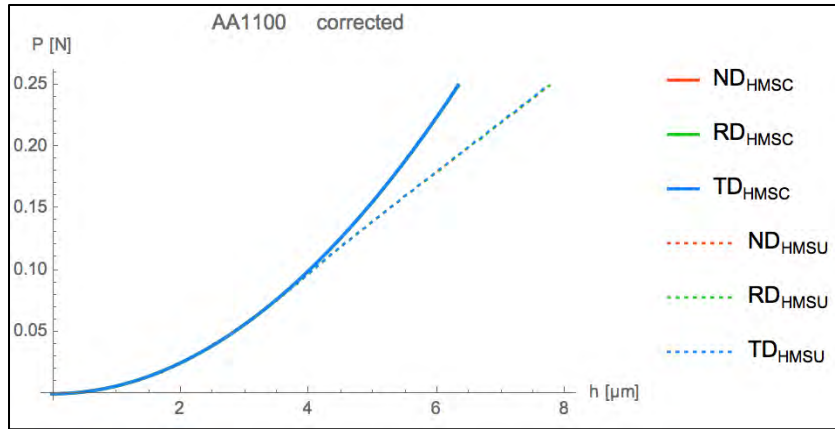
Figure 5.6 Corrected HMS indentation curves. AA1100. U: uncorrected. C: corrected
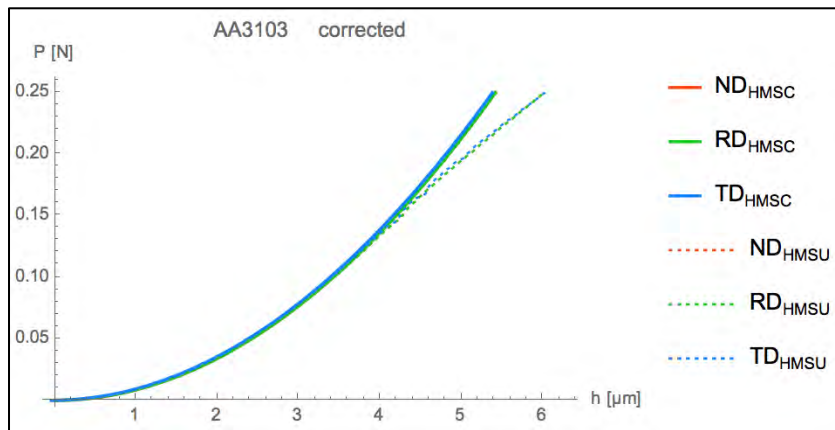
Figure 5.7 Corrected HMS indentation curves. AA3103. U: uncorrected. C: corrected

Comparison between experimental and HMS results

Comparison was made in terms of indentation shape, particularly pile up, indentation depth, and amount of anisotropy. For the first one it was found that HMS predicted a change in pile-up position for different directions. The simulations predict the experimental pile up position adequately, although HMS consistently simulated smaller pile ups.

With respect to indentation depth and amount of anisotropy, there was a large deviation between HMS and experiments. HMS always predicted softer materials and less anisotropy than its experimental counterpart. Regarding indentation depth, the plastic zone breakthrough correction mentioned before greatly decreased the amount of deviation, as seen in Fig 5.8 through Fig. 5.12, and Table 5.1.

Figure 5.8 Corrected and uncorrected HMS indentation curves vs experimental ones. AA6016mm1
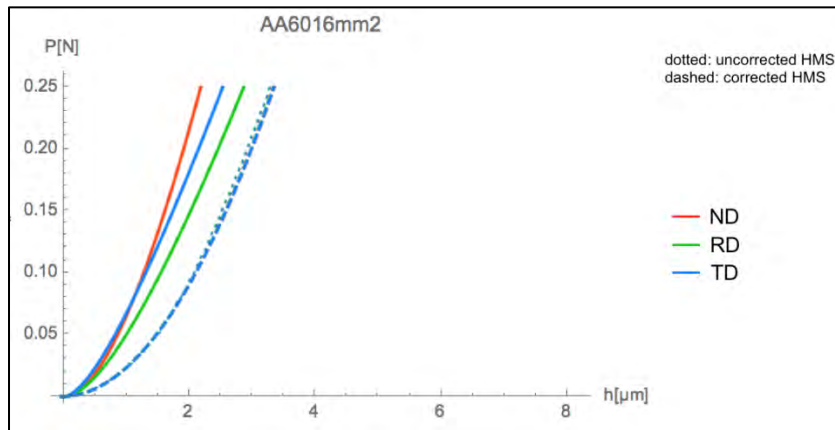
Figure 5.9 Corrected and uncorrected HMS indentation curves vs experimental ones. AA6016mm2
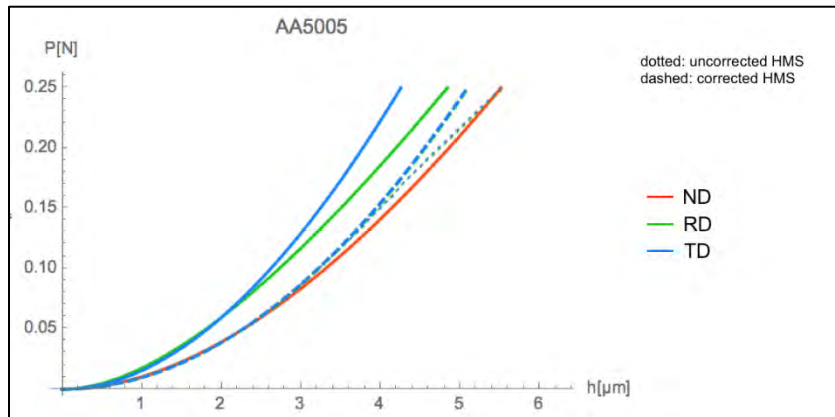
Figure 5.10 C Corrected and uncorrected HMS indentation curves vs experimental ones. AA5005
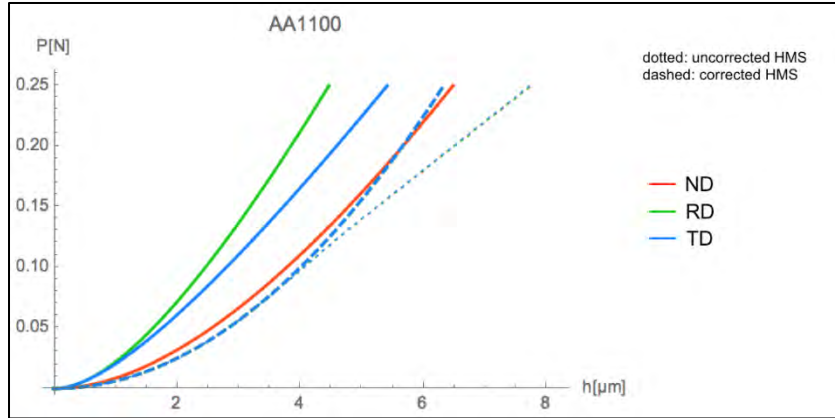
Figure 5.11 Corrected and uncorrected HMS indentation curves vs experimental ones. AA1100
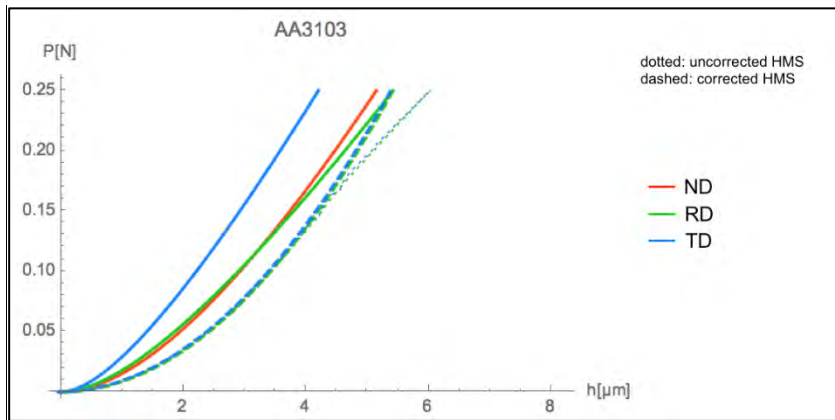
Figure 5.12 Corrected and uncorrected HMS indentation curves vs experimental ones. AA3103
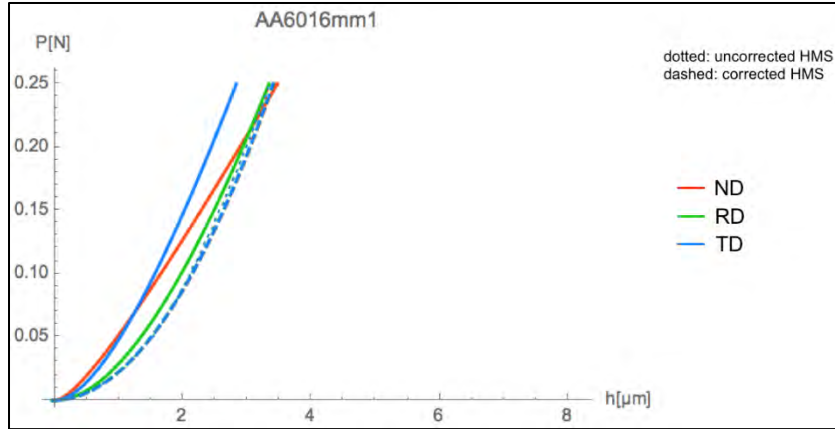
Table 5.1 Deviation between experimental results and corrected HMS predictions (depth)

	HMS indentation depth [μm]						
	Uncorrected				Corrected		
	d_{HMSU}	%dev	Mean %dev		d_{HMSC}	%dev	Mean %dev
AA6016mm1							
ND	3.346	3.7			3.416	1.6	
RD	3.348	0.2	7.3		3.407	1.9	7.9
TD	3.349	18.2			3.407	20.2	
AA6016mm2							
ND	3.295	50.7			3.352	53.3	
RD	3.273	14.1	31.4		3.338	16.4	33.9
TD	3.283	29.5			3.346	32.0	
AA5005							
ND	5.539	0.5			5.091	7.6	
RD	5.554	14.8	15.0		5.100	5.4	10.9
TD	5.514	29.6			5.087	19.6	
AA1100							
ND	7.760	19.8			6.329	2.3	
RD	7.752	73.7	45.4		6.331	41.8	20.3
TD	7.730	42.9			6.325	20.3	
AA3103							
ND	6.020	17.0			5.418	5.3	
RD	6.016	11.0	23.8		5.418	0.0	11.1
TD	6.029	43.5			5.381	28.1	

A fraction of the remaining deviation can be associated to the use of a Voce hardening law. This law is often used to permit saturation of the strain hardening at high strains. However, it was found in this work that such saturation occurs much earlier than expected if the law is fitted to tensile data for the different Al-alloys. As seen from Fig. 1.2 and Fig. 2.1, the employed Voce laws predict saturation much earlier than what is described in the literature. Future works need to include improved hardening laws, or even better, use the original tensile test data without fitting to an empirical expression.

The possibility of an indentation size effect, i.e. material tends to appear harder at small indentation depths, was also considered. A brief literature review demonstrated, however, that this effect is visible at far smaller indentation loads and depths than the case at hand (P=0.25N, Min. overall indentation depth: 2,220 nm) (Fig. 5.13) [69, 70, 71].
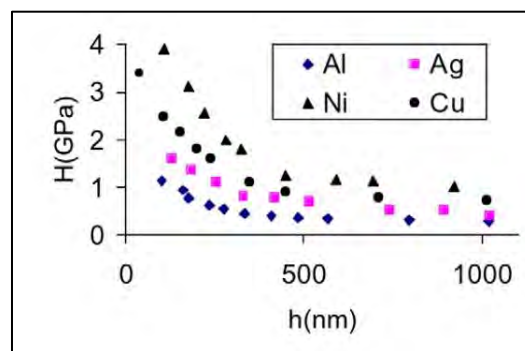

Figure 5.13 Size effect. Hardness vs indentation depth [71]

As for the difference in the amount of anisotropy, two main reasons are proposed. The first one is related to the asymmetric mesh. As was mentioned before, this mesh could compensate a certain part of the anisotropic effect. However, the amount of deviation of squareness is small in comparison to the amount of anisotropy experimentally found (Table 4.7). Therefore, it is considered that this asymmetric mesh causes at most a small fraction of the observed deviation. Nonetheless, it represents a point of improvement for future works.

This work proposes, however, that the main reason of deviation between amount of anisotropy predicted and experimentally found is related to the yield locus, as will be explained in the following paragraphs. For simplicity, only the (σ_{11}-σ_{22}) section of the yield locus was obtained, and consequently, only the behaviour for RD and TD will be analysed.

Recapitulating some characteristics of the employed yield loci in this work:
   a) Discrete yield loci were constructed by using a crystalline approximation (ALAMEL) and a set of defined strain rate modes.
   b) A continuous function was obtained from these points by the Facet method.
   c) Isotropic homogenous hardening was assumed, which means that during the plastic deformation process the yield locus is multiplied by a single number according to the hardening law employed. This is based on the assumption that during a tension test, the influence of hardening and anisotropy can be multiplicatively separated.

Therefore, throughout the process the yield locus only changes in size but not in shape (Fig 5.14) (it shall be reminded that texture evolution can cause a change in shape, but this effect was found to be insignificant in the present simulations) Consequently, under this assumption, the relationship between yield stress in the RD and TD directions (σ_{RD} and σ_{TD}) is maintained throughout the process.
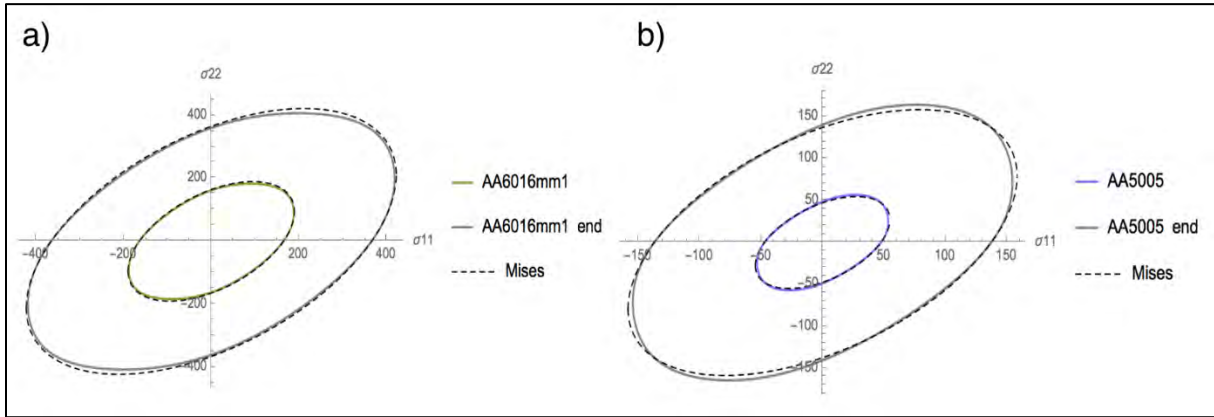
Fig. 5.14 Yield loci at the start and at the end of the deformation process (approx.) a) AA6016mm1. b) AA5005

The isotropic homogenous hardening assumption also implies that the relationship between indentation depth in the RD and TD (d_{RD}, d_{TD}) is maintained throughout the process. This is useful since, although σ_{RD} and σ_{TD} can be easily obtained from FEM, they are not accessible with the obtained experimental data. Since under this assumption d_{RD} and d_{TD} are proportional, by plotting d_{RD} and d_{TD} one should obtain a straight line (Fig. 5.15 through Fig. 5.19).
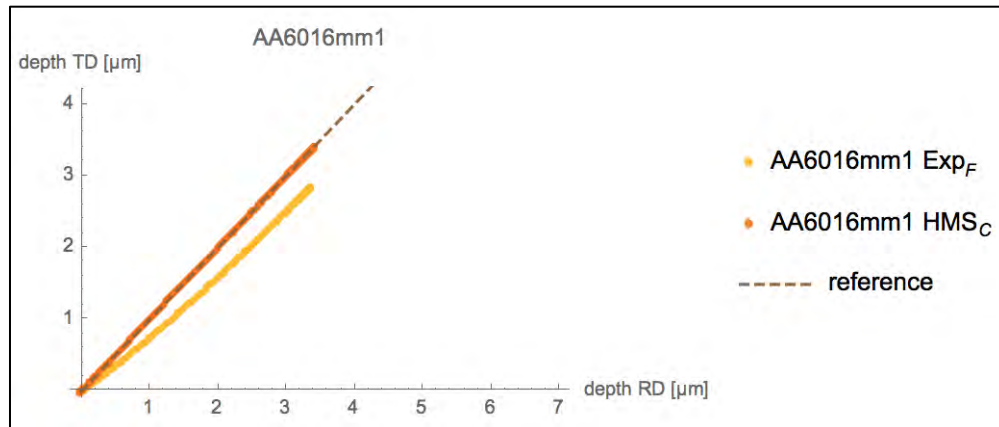
Fig. 5.15 d_{RD} and d_{TD}. HMS (orange). Experimental (light orange). AA6016mm1
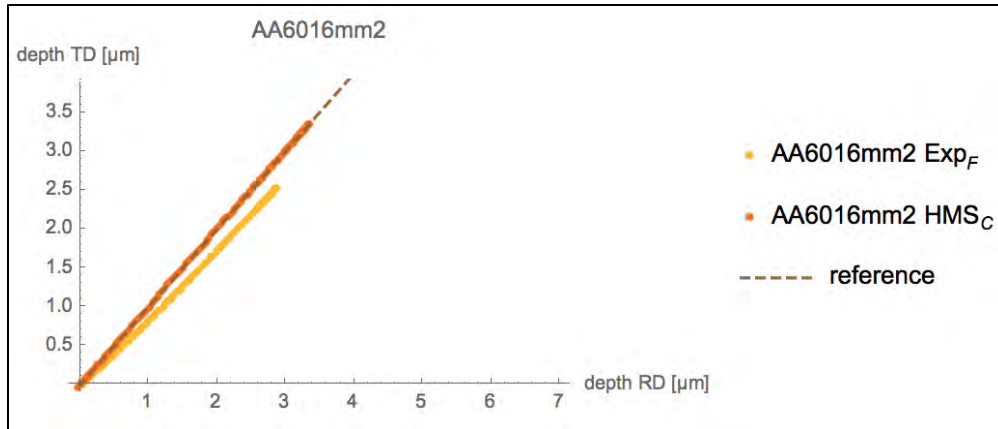
Fig. 5.16 d_{RD} and d_{TD}. HMS (orange). Experimental (light orange). AA6016m2
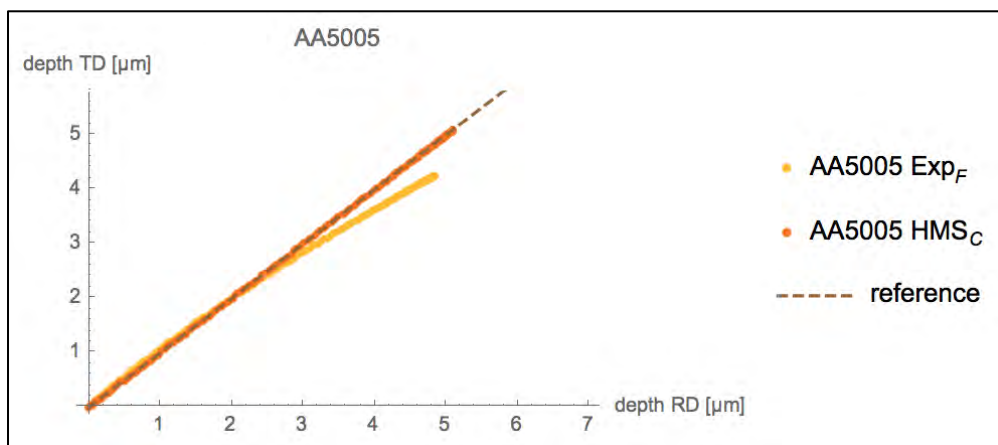
Fig. 5.17 d_{RD} and d_{TD}. HMS (orange). Experimental (light orange). AA5005

Fig. 5.18 d_{RD} and d_{TD}. HMS (orange). Experimental (light orange). AA1100

70

Fig. 5.19 d_{RD} and d_{TD}. HMS (orange). Experimental (light orange). AA3103

As seen from these figures, HMS data does yield a straight line. This is unsurprising since HMS worked all the time under the assumption that the hardening rates are equal in all directions. However, for the experimental data, one can observe that the proportionality between d_{RD} and d_{TD} is only maintained at the beginning. This means that the real relationship between 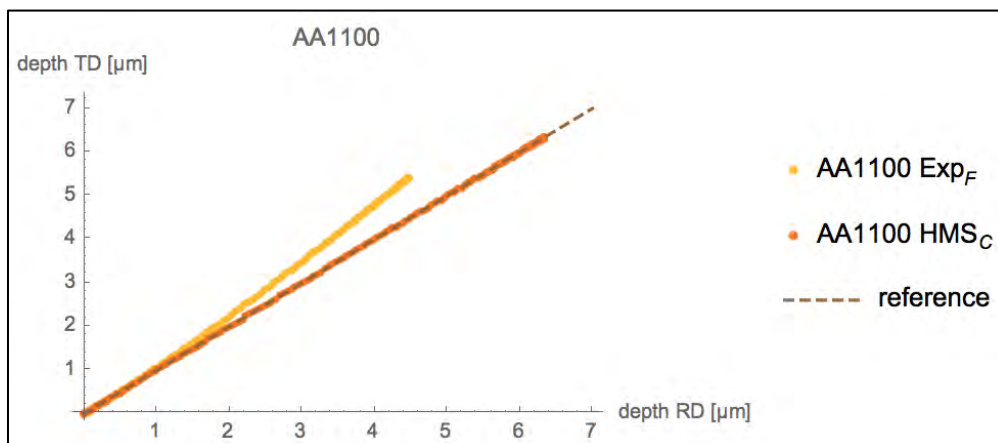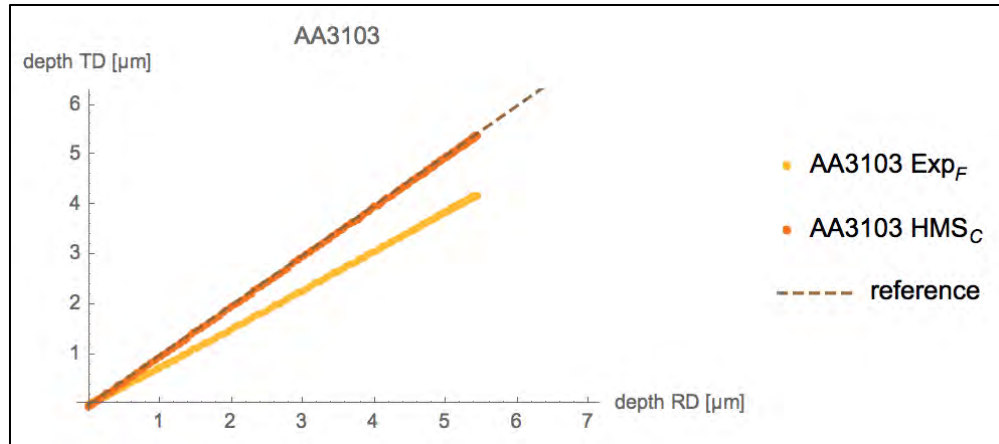σ_{RD} and σ_{TD}, is not maintained throughout the process, with some materials even deviating from this assumption very early in the deformation process.

The deviation of the proportionality between experimental σ_{RD} and σ_{TD} can be due to two reasons. The first one is related to texture evolution, where this change of texture could imply in the long run a change in shape for the yield locus, and consequently a change in the relationship between σ_{RD} and σ_{TD}. However, simulations with texture evolution were run, and produced no visible difference, therefore, this reason was discarded.

The second reason of this deviation between σ_{RD} and σ_{TD} proportionality is due to an effect known as anisotropic hardening. In simple words, this effect means that TD and RD harden at different rates, thus one single strain hardening behaviour description (in the RD direction, for example) is not enough to model the yield stress of the material in other directions. In these cases, yield loci change in shape and size during the process. Therefore, this work proposes that the difference in the amount of the anisotropy predicted is mainly due to the assumption that a single hardening law is enough to describe change in the yield locus during deformation. It should be mentioned that this consideration is at the very heart of the classic theory of plasticity.

It is not the first time that the effect of anisotropic hardening has been observed [67]. As a matter of fact, due to the anisotropic nature of a single grain, this effect is always present, but the magnitude of its influence in the observed macroscopic behaviour varies depending on the specific strain mode associated to the process under consideration. It appears that, for the study at hand (indentation at micro scales), the effect is rather strong.

Conclusions

A multiscale plasticity code (HMS) was used, in conjunction with an FEM model, to simulate and analyse the anisotropic plastic deformation taking place during an indentation test (Vickers). The simulations were compared to a series of experiments carried out for 5 alloys, in the ND, RD, and TD directions. The main aim of this thesis was to use concepts of crystal and continuum plasticity, texture, and FEM to explain the differences between experimental results and predictions.

With regards to the experimental results, the indentation curves were fitted by a procedure where a single fitting curve was obtained by considering the information from all experimental data simultaneously. This procedure turned out to be accurate and efficient, since it provided a fitted indentation depth with less than 5% deviation from the experimental mean by a simpler method than the ones commonly found in the literature. Weighted least square fitting may further improve the results. The extrapolation procedure for determining elastic recovery was successful as well.

Statistically significant variation of these indentation curves for different test orientations was found in all alloys, which, for indentation purposes, can be considered anisotropic. By analysing the indentation diagonals, it was determined that the indentations did not have an ideal indentation shape, which produces deviations in the calculated value of HV. To prevent this, indentation depth (inversely related to hardness) was used instead. Additionally, this parameter had the advantage that is more closely related to the magnitude of plastic strain.

Concerning the HMS/FEM model, a study of the influence of model parameters was carried out to reduce any errors in the simulations that are not directly related to material behaviour. Factors such as elastic properties of the Vickers pyramid, friction coefficient, mesh geometry, and texture evolution were found to have a minimal influence in the results. However, model size, due to a plastic zone breakthrough effect, and the definition of the hardening laws employed greatly influenced the results. Using the scaling properties of continuum plasticity, it was possible to employ a method to correct the plastic breakthrough effect, yielding important modifications in terms of indentation depth.

Comparison between predicted and experimental results was done in terms of pile up, indentation depth, and amount of anisotropy. It was found that HMS predicted pile-up position with acceptable adequacy, although it underestimated pile-up size. Clear effects of anisotropy are found in this phenomenon, which cannot be modelled with isotropic approximations.

With regards to indentation depth, large differences were found. The corrections made for model size and plastic breakthrough, mentioned before, provided a significant decrease in the amount of deviation between experimental and predicted indentation depth. It was also found that the characteristics of the chosen hardening law played a significant part in this difference, as the Voce law shows saturation at values of true strain where this phenomenon is not yet expected. The possibility of an indentation size effect was also studied; however, it was found that even the smallest experimental indentation depth was well above the range where ISE is found.

Finally, it was proposed that the fact that HMS consistently predicted less anisotropy than the observed in measurements was mainly due to the use of the approximation of homogeneous isotropic hardening. Under the assumption of isotropic hardening, the indentation depth in different directions should increase proportionally, as is observed in the model but not in the experiments. The exact moment in which this deviation starts to manifest itself clearly varies from material to material. This observed deviation was attributed to an effect known as anisotropic hardening, which implies RD and TD harden at different rates. This means that the yield locus changes shape and size throughout the deformation process, and at least two different strain hardening descriptions are needed. Texture evolution being behind this change in relationship between σ_{RD} and σ_{TD} was also considered. However, it was discarded since texture evolution simulations did not modify the results in any significant way.

In summary, it was found that the experimental observations were consistent with established norms and that the indentation depth measured by AFM was comparable to the one obtained directly from the indentation test. A large set of factors was found to have a small effect on the simulation results (elastic properties of the Vickers pyramid, friction coefficient, mesh geometry, texture evolution). Two important effects related to the FEM-model were identified. The first one is the breakthrough of the plastic zone to the mesh boundaries, which provokes a strong overestimation of the indentation depth. This effect is eliminated by analysing the model at smaller loads and applying scaling laws. The second one is the early saturation of the Voce-law used, which can be corrected by using different descriptions for strain hardening in future work. The fundamental reason for the underestimation of indentation anisotropy in HMS, however, seems to be the phenomenon of anisotropic hardening, which will require the development of new and more complex models for crystal plasticity.

References

[1] Totten, G. E., & MacKenzie, D. S. (Eds.). (2003). *Handbook of Aluminum: Vol. 1: Physical Metallurgy and Processes* (Vol. 1). CRC Press.

[2] Campbell, F. C. (Ed.). (2008). *Elements of metallurgy and engineering alloys*. ASM International.

[3] Aluminum Association. (2009). International alloy designations and chemical composition limits for wrought aluminum and wrought aluminum alloys. *Teal Sheets*, 1-28.

[4] The Aluminum Association. (2006). Aluminum Alloys 101. Retrieved from http://www.aluminum.org/resources/industry-standards/aluminum-alloys-101

[5] Aluminum Alloy Heat Treatment Temper Designations. (2003). Retrieved from http://www.matweb.com/reference/aluminumtemper.aspx

[6] Primary Aluminium Production. (n. d.). Retrieved from

[7] Reardon, A. C. (Ed.). (2011). *Metallurgy for the Non-metallurgist*. ASM International.

[8] Hardness (n. d.). Retrieved from http://www.engineering-dictionary.com/index.php?definition=2061#

[9] Hardness. (n. d.). Retrieved from https://www.nde-ed.org/EducationResources/CommunityCollege/Materials/Mechanical/Hardness.htm

[10] Ramírez, M. A., Schouwenaars, R., Eyckens, P., Gawad, J., Kestens, L., Van Bael, A., & Van Houtte, P. (2016). Experimental validation and effect of modelling assumptions in the hierarchical multi-scale simulation of the cup drawing of AA6016 sheets. *Modelling and Simulation in Materials Science and Engineering*, *25*(1), 015002.

[11] Eyckens, Philip & An, Y.G. & Gawad, Jerzy & Roose, Dirk & Mulder b, Hans & Van Bael, Albert. (2016). Multi-scale Solutions for Property Variability in Metal Forming CAE design from base material up to formed part

[12] Gawad, J., Van Bael, A., Eyckens, P., Samaey, G., Van Houtte, P., & Roose, D. (2013). Hierarchical multi-scale modeling of texture induced plastic anisotropy in sheet forming. *Computational Materials Science*, *66*, 65-83.

[13] Chakrabarty, J. (2012). *Theory of plasticity*. Butterworth-Heinemann.

[14] ASTM E8 / E8M-16a, Standard Test Methods for Tension Testing of Metallic Materials, ASTM International, West Conshohocken, PA, 2016, www.astm.org

[15] Verlinden, B., Driver, J., Samajdar, I., & Doherty, R. D. (2007). *Thermo-mechanical processing of metallic materials* (Vol. 11). Elsevier.

[16] Rollett, A. D., & Kocks, U. F. (1993). A review of the stages of work hardening. In *Solid State Phenomena* (Vol. 35, pp. 1-18). Trans Tech Publications.

[17] Hill, R. (1998). *The mathematical theory of plasticity* (Vol. 11). Oxford university press.

[18] Van Houtte, P., Yerra, S. K., & Van Bael, A. (2009). The Facet method: A hierarchical multilevel modelling scheme for anisotropic convex plastic potentials. *International Journal of Plasticity*, *25*(2), 332-360.

[19] Banabic, D., Barlat, F., Cazacu, O., & Kuwabara, T. (2010). Advances in anisotropy and formability. *International Journal of Material Forming*, *3*(3), 165-189.

[20] Engler, O., & Randle, V. (2010). *Introduction to texture analysis* (2nd ed.). Taylor & Francis Group.

[21] Waeselmann, N. (2012). Structural transformations in complex perovskite-type relaxor and relaxor-based ferroelectrics at high pressures and temperatures.

[22] Crystallographic Texture in Aluminium. (n.d.). Retrieved from http://core.materials.ac.uk/repository/alumatter/anisotropy.htm

[23] Kocks, U. F., Tomé, C. N., & Wenk, H. R. (2000). *Texture and anisotropy: preferred orientations in polycrystals and their effect on materials properties*. Cambridge university press.

[24] Banabic, D. (2016). *Multiscale Modelling in Sheet Metal Forming*. Springer.

[25] Van Houtte, P., Kanjarla, A. K., Van Bael, A., Seefeldt, M., & Delannay, L. (2006). Multiscale modelling of the plastic anisotropy and deformation texture of polycrystalline materials. *European Journal of Mechanics-A/Solids*, *25*(4), 634-648.

[26] Planes. (n. d.). [online image]. Retrieved from http://www.kochmann.caltech.edu/research_finiteplasticity.html

[27] Schmid's Law. (n. d.). [online image]. Retrieved from http://www.engineeringarchives.com/les_matsci_schmidslaw.html

[28] Zhang, K., Holmedal, B., Hopperstad, O. S., Dumoulin, S., Gawad, J., Van Bael, A., & Van Houtte, P. (2015). Multi-level modelling of mechanical anisotropy of commercial pure aluminium plate: crystal plasticity models, advanced yield functions and parameter identification. *International Journal of Plasticity*, *66*, 3-30.

[29] Van Houtte, P., Li, S., Seefeldt, M., & Delannay, L. (2005). Deformation texture prediction: from the Taylor model to the advanced Lamel model. *International Journal of Plasticity*, *21*(3), 589-624.

[30] Roters, F., Eisenlohr, P., Hantcherli, L., Tjahjanto, D. D., Bieler, T. R., & Raabe, D. (2010). Overview of constitutive laws, kinematics, homogenization and multiscale methods in crystal plasticity finite-element modeling: Theory, experiments, applications. *Acta Materialia*, *58*(4), 1152-1211.

[31] Van Houtte, P. HMS User's Manual. (2013). MTM KU Leuven.

[32] Principle of the Vickers hardness test. (n. d.). [Online image] Retrieved from http://me.aut.ac.ir/staff/solidmechanics/alizadeh/Hardness%20Test.htm

[33] Bolshakov, A., & Pharr, G. (1998). Influences of pileup on the measurement of mechanical properties by load and depth sensing indentation techniques. *Journal of Materials Research*, *13*(04), 1049-1058

[34] Roxel, T. (2015). Schematic drawing of the indentation volume topological analysis by means of AFM [online image]. Retrieved from http://rsta.royalsocietypublishing.org/content/373/2038/20140140

[35] Qu, Z. (2016). Sink in effects on indentation. [online image]. Retrieved from http://appliedmechanics.asmedigitalcollection.asme.org/article.aspx?articleid=2482750

[36] Typical force displacement curve showing measured and derived parameters. (n. d.). [online image]. Retrieved from http://www.npl.co.uk/science-technology/mass-and-force/hardness/instrumented-indentation

[37] Oliver, W. C., & Pharr, G. M. (1992). An improved technique for determining hardness and elastic modulus using load and displacement sensing indentation experiments. *Journal of materials research*, *7*(6), 1564-1583.

[38] Weaver, J. S., & Kalidindi, S. R. (2016). Mechanical characterization of Ti-6Al-4V titanium alloy at multiple length scales using spherical indentation stress-strain measurements. *Materials & Design*, *111*, 463-472.

[39] Tabor, D. (2000). *The hardness of metals*. Oxford university press.

[40] Marteau, J., Bouvier, S., & Bigerelle, M. (2015). Review on numerical modeling of instrumented indentation tests for elastoplastic material behavior identification. *Archives of Computational Methods in Engineering*, *22*(4), 577-593.

[41] Cheng, Y. T., & Cheng, C. M. (1998). Scaling approach to conical indentation in elastic-plastic solids with work hardening. *Journal of Applied Physics*, *84*(3), 1284-1291.

[42] Cheng, Y. T., & Cheng, C. M. (1998). Analysis of indentation loading curves obtained using conical indenters. *Philosophical magazine letters*, *77*(1), 39-47.

[43] Cheng, Y. T., & Cheng, C. M. (2004). Scaling, dimensional analysis, and indentation measurements. *Materials Science and Engineering: R: Reports*, *44*(4-5), 91-149.

[44] Nanovea (n. d.). Chromatic Confocal Surface Measurement. Retrieved from https://nanovea.com/chromatic-confocal/

[45] CHRomatic Confocal Principle for Distance Measurements. (n. d.). [online image]. Retrieved from http://www.precitEq.de/en/products/optical-measuring-technology/how-it-works/

[46] Resolution. (n. d.). Retrieved from https://www.microscopyu.com/microscopy-basics/resolutions

[47] Scanning Electron Microscope A To Z: Basic Knowledge for using the SEM (n. d.). Retrieved from https://www.jeol.co.jp/en/applications/pdf/sm/sem_atoz_all.pdf

[48] Rob, H. (2016). Mechanisms of emission of secondary electrons, backscattered electrons, and characteristic X-rays from atoms of the sample. [online image]. Retrieved from https://en.wikipedia.org/wiki/Scanning_electron_microscope#/media/File:Electron_emission_mechanisms.svg

[49] Robert, W., & Heather, B. (n. d.) Basic Theory: Atomic Force Microscopy. Retrieved from http://asdlib.org/onlineArticles/.../SPMModule_BasicTheoryAFM.pdf

[50] Zhen, G. (2012). Schematic illustration of the principles of AFM. [online image]. Retrieved from https://www.researchgate.net/figure/Schematic-illustration-of-the-principles-of-AFM-The-scanner-is-composed-of-three-piezo_fig1_221927184

[51] Park Systems. (n. d.). Inter-atomic Force vs. distance. [online image]. Retrieved from http://www.parkafm.com/index.php/park-spm-modes/91-standard-imaging-mode/223-basic-contact-afm-dynamic-force-microscope-dfm

[52] Scanning electron microscope. (n. d.). Retrieved from https://en.wikipedia.org/wiki/Scanning_electron_microscope

[53] Wenjie, M. (n. d.). Fundamental Theory of Atomic Force Microscopy. Retrieved from http://www.nanoscience.gatech.edu/zlwang/research/afm.html

[54] Optical profilometry. (n. d.). Retrieved from https://www.mri.psu.edu/materials-characterization-lab/characterization-techniques/optical-profilometry

[55] Aluminium. (n. d.) Retrieved 8 April 2017, from http://www.matweb.com/search/DataSheet.aspx?MatGUID=0cd1edf33ac145ee93a0aa6fc666c0e0&ckck=1

[56] P. Van Houtte. The "MTM-FHM" software system, Version 2. Department of Metallurgy and Materials Engineer- ing, Katholieke Universiteit Leuven, Belgium, January 2004

[57] ASTM E3-11(2017), Standard Guide for Preparation of Metallographic Specimens, ASTM International, West Conshohocken, PA, 2017, www.astm.org

[58] Coefficient of variation. (n. d.). Retrieved from https://en.wikipedia.org/wiki/Coefficient_of_variation

[59] ASTM E384-17, Standard Test Method for Microindentation Hardness of Materials, ASTM International, West Conshohocken, PA, 2017, www.astm.org

[60] Autodesk (n. d.). Reality Capture And 3D Scanning Software Retrieved from https://www.autodesk.com/products/recap/overview

[61] Jacobo, V. H., Ortiz, A., & Schouwenaars, R. (2016). Indentation curves in viscoplastic alloys: mathematical model, fitting procedures, and application to the room-temperature creep of an Al-Sn alloy. *Advances in Materials Science and Engineering*, *2016*.

[62] Ramírez, M. A., Figueroa, C. G., Jacobo, V. H., Ortiz, A., & Schouwenaars, R. (2012). Mesh optimisation for the reverse modelling of the Vickers test and its application to a tribologically modified surface layer. In *Proceedings of the 3rd International Conference on Engineering Optimization (EngOpt'12)*.

[63] Diamond: Mechanical properties, elastic constants, lattice vibrations. (n. d.). Retrieved from http://www.ioffe.ru/SVA/NSM/Semicond/Diamond/mechanic.html

[64] Wang, M., Wu, J., Zhan, X., Guo, R., Hui, Y., & Fan, H. (2016). On the determination of the anisotropic plasticity of metal materials by using instrumented indentation. *Materials & Design*, *111*, 98-107.

[65] Wang, M., Wu, J., Fan, H., Zhang, Z., & Wu, H. (2017). Extraction of the Anisotropic Plasticity of Metal Materials by Using Inverse Analysis and Dual Indentation Tests. *Materials*, *11*(1), 12.

[66] Choi, Y., Park, J. H., Kim, B. M., Choi, J. C., & Min, B. H. (2000). Estimation of relation between effective strain and hardness by rigid-plastic FEM. *Metals and Materials*, *6*(2), 111-116.

[67] Ramírez, M.A. (2016). *Validación de un código de elemento finito para plasticidad anisotrópica mediante ensayos en productos metálicos laminados* (Doctorado). Universidad Nacional Autónoma de México.

[68] Mánik, T., & Holmedal, B. (2013). Additional relaxations in the Alamel texture model. *Materials Science and Engineering: A*, *580*, 349-354.

[69] Manika, I., & Maniks, J. (2006). Size effects in micro-and nanoscale indentation. *Acta Materialia*, *54*(8), 2049-2056.

[70] Gao, X. L. (2006). An expanding cavity model incorporating strain-hardening and indentation size effects. *International journal of solids and structures*, *43*(21), 6615-6629.

[71] Zhao, M., Slaughter, W. S., Li, M., & Mao, S. X. (2003). Material-length-scale-controlled nanoindentation size effects due to strain-gradient plasticity. *Acta Materialia*, *51*(15), 4461-4469.

[72] Sachs, G. (1928). Zur Ableitung einer Fliessbedingung. Z. Ver. deut.Eng., 72.